Insights into the Excited State of Organic Small Molecules With Inelastic Neutron Scattering

Vong, Daniel

2023

Insights into the Excited State of Organic Small Molecules With Inelastic Neutron Scattering

By

DANIEL VONG

DISSERTATION

Submitted in partial satisfaction of the requirements for the degree of

DOCTOR OF PHILOSOPHY

in

Materials Science and Engineering

in the

OFFICE OF GRADUATE STUDIES

of the

UNIVERSITY OF CALIFORNIA

DAVIS

Approved:

Adam Moulé, Chair

Luke Daemen

Ambarish Kulkarni

Committee in Charge

2023

To my mother, who single-handedly got 5 kids to eat vegetables.

Contents

List of Figures

LIST OF TABLES

Abstract

Insights into the Excited State of Organic Small Molecules With Inelastic Neutron Scattering

Considerable research into organic small molecules (OSM) have taken place due to its cheap large scale fabrication cost compared to inorganic semiconductors, tunable optical and electronic properties, and its potential to be designed flexible, transparent, and light weight. OSM are a class of organic semiconductors that form extended crystals. These crystals are held together by weak Van der Waals forces which allow large amplitude inter- and intra- molecular motions. The motions cause large electronic coupling fluctuations, which results in unfavorable electronic properties. With the infinite design space afforded to OSM, it is difficult to make a distinction between molecular design and detrimental molecular motions. Thus, it is important to have full knowledge of the phonon spectrum to design molecules with favorable electronic properties.

Inelastic neutron scattering (INS) is a spectroscopy technique well-suited to study the dynamics of OSM. Here, we use INS in conjunction with density functional theory to highlight the phonon modes that are detrimental to the electronic coupling. Design principles are considered to reduce the infinite design space that dampens those detrimental phonons. We then expand the capabilities of INS by designing and building a sample changer stick, and two photochemistry sample sticks. The sample changer stick can simultaneously cool four samples, and measure each individually. The first photochemistry sample stick uses an LED above the sample container within the closed-cycle refrigerator on the VISION neutron spectrometer at Oak Ridge National Laboratory. The second incorporates a laser and tumbler sample mixing system to increase the density of photoexcited sample. We show simple test cases using an acene and 405 nm photoresin for the two designs. Lastly, an experimental and computational study of an exciton mechanism, singlet fission (SF), in tetracene and pentacene are studied with varying excitation energies. The findings suggest the electronic states shifts due to the excimer deformations leading to energetically favorable SF.

ACKNOWLEDGMENTS

To express my acknowledgements from my heart, rather than my head, I express this in spanish. Quiero empezar expresando mi más sincero agradecimiento a los programas predoctorales de diversidad que me apoyaron durante mis estudios universitarios. En particular, quiero dar las gracias a los programas UCLEAD de la UCSB y PREP de la UCSC por su tutoría y orientación, y por haberme brindado la primera oportunidad de demostrar mi valía, y prepararme para el viaje que estaba por venir.

También me gustaría expresar mi sincero agradecimiento a mi coasesor, el profesor Ambarish Kulkarni, por su perspicacia y apoyo en los estudios computacionales, y por enseñarme a pensar como un científico computacional. Su experiencia en DFT y su disposición a colaborar y compartir sus conocimientos han sido esenciales para el avance de mi investigación.

Estoy igualmente agradecido a mi otro coasesor en el ORNL, el Dr. Luke Daemen, por su tutoría en el diseño y por permitirme explorar mis muchas ideas locas. Su profundo conocimiento y experiencia han sido inestimables para dar forma a mi investigación y ayudarme a superar todos los obstáculos.

Me gustaría expresar mi más profunda gratitud a mi asesor principal, Adam Moulé. Su tutoría, orientación y apoyo a lo largo de mi doctorado han sido inestimables y me han permitido dar lo mejor de mí. También estoy agradecida por su constante apoyo, aliento y paciencia mientras sorteaba los numerosos retos y obstáculos que surgen en el transcurso de un programa de doctorado. Estoy verdaderamente agradecido por todo lo que han hecho por mí y por las valiosas lecciones que me han enseñado como científico.

Por último, me gustaría expresar mi gratitud a mis colegas que me han apoyado a lo largo de este viaje. Especialmente a mis colegas Makena, Meghna y Maggie. Su constante apoyo, ánimo y comprensión han sido esenciales para ayudarme a alcanzar mis metas académicas y personales.

Gracias a todos por vuestro constante apoyo y ánimo a lo largo de mi doctorado. Estoy verdaderamente agradecida por todo lo que habéis hecho por mí.

Chapter 1

Introduction

1.1 Preamble

My dissertation contains four publications that I have co-authored in my time as a UC Davis graduate student. The four publications focus on excited state processes in organic small molecules making heavy use of VISION, the inelastic neutron scattering spectrometer at Oak Ridge National labs. Thus this section will include a brief introduction to small molecule organic semiconductors, some light math for derivation of the structure factor for inelastic neutron scattering, and then introduce each paper with more details in the following chapters.

1.2 Introduction

Organic semiconductors (OSC) have undergone rapid development for use in applications such as organic light emitting diodes, transistors, biological and chemical sensors, and wearable and flexible electronics[1]. Organic small molecules (OSM), a class of OSC able to form highly ordered crystalline domains, shows promise as an alternative to inorganic semiconductors (Silicon, Gallium Arsenide, etc.) wherein the cost is dominated by the fabrication processes[2, 3]. OSM are solution processable and can take advantage of large scale manufacturing techniques, but device efficiencies are too low and thus the widespread use of OSM in devices are cost prohibitive. The current major limitations to device efficiency within OSM based devices are the low charge carrier mobilities (μ) and exciton lifetimes[4] compared to their inorganic counterparts.[5] The unfavorable electronic properties are due in large part to the large amplitude motions within these Van der Waals bound materials.

The large amplitude motions within weakly Van der Waals bound OSM causes large fluctuations in the transfer integral (J) with the same order of magnitude of the transfer integral[6] itself, causing a transient localization of the charge and reducing μ. This is termed dynamic disorder and was first described with transient localization theory (TLT) developed by Ciuchi, Fratini, and Mayou[7]. In contrast to band theory, which calculates unphysical scattering lengths, or hopping theory, which calculates an incorrect temperature dependence for μ, TLT posits the occurrence of both delocalization across a few molecules, and hopping between the delocalized paths.[8, 9] The TLT framework describes the transient localization having a characteristic timescale, τ_R, and localization length, $L(\tau_R)$. Accurate calculations of μ have been achieved with TLT,[10, 11] using a Kubo-Greenwood[12, 13] approach to the Einstein relation to mobility,

$$\mu = \frac{e}{2k_BT}\frac{L(\tau_R)^2}{\tau_R}$$

where $L(\tau_R)^2$ is the average of the localization length about the characteristic timescale for the two Cartesian directions within the high mobility plane, $L(\tau_R)^2 = (L_{xx}(\tau_R)^2 + L_{yy}(\tau_R)^2)/2$. L_{xx} and L_{yy} can be calculated from the overlap of the eigenstates of the system with the current operator expressed in terms of the energy eigenstates

$$L^2_{xx}(\tau_R) = \frac{1}{Z}\sum_{n,m} e^{-E_n/k_BT}|\langle n|\hat{j_x}|m\rangle|^2 \frac{2}{(\hbar\tau_R^{-1})^2 + (E_m - E_n)^2}$$

$$\hat{j_x} = -i\sum_{k,l}(x_k - x_l)J_{kl}|k\rangle\langle l|$$

where $|n\rangle$ and $|m\rangle$ are eigenstates with eigenvalues E_n and E_m, respectively, Z is the partition function, and $\beta = 1/k_BT$. This methods represents the nuclear modes as frozen in which the dynamic disorder is replaced by static disorder with the same order of magnitude.

The dynamic disorder has been found to be for both inter- and intra- molecular motions.[14] In the same vein, exciton diffusion length is influenced by various factors, including molecular packing and intermolecular interactions. Excitons are electron-hole pairs formed from the absorption of a photon that are strongly bound in organic materials by the strong exciton binding energy. Many devices can be improved by increasing exciton diffusion length. For example, a longer exciton diffusion length is desirable for efficient charge transport in organic photovoltaics. It allows more excitons to diffuse farther and reach the interface between different layers, increasing exciton dissociation and subsequent charge carrier collection. Triplet excitons, in particular, can diffuse through Dexter energy transfer,[15] a through-bond mechanism highly dependent on the orbital overlap. With singlet fission, wherein a pair of correlated triplet excitons are formed from a single singlet, it becomes important to understand how dynamic disorder affects this process and their subsequent separation into two uncorrelated triplets.

It is thus clear that obtaining practical electronic properties require further insights into the interplay of molecular composition and phonons. Acenes are a family of molecules that are intensely studied to gain insight into the aforementioned relationship. Acenes are planar and rigid, aromatic molecules consisting of linearly fused benzene rings, exhibiting moderate μs. Increasing the number of fused benzenes can have an unpredictable effect on the material properties. For example, with each additional fused benzene from napthalene (two rings) to pentacene (five rings), the reorganization energy reduces, indicating more order, but the μ varies.[16] A strong correlation between reorganization energy and μ has not been experimentally observed.[17] Furthermore, each additional fused rings reduces the band gap,[18–20] all the while maintaining similar herringbone molecular packing. Thus, the simplicity of studying acene and incorporating minor changes to study their derivatives has allowed major efforts into elucidating "design rules" to reduce dynamic disorder and improve electronic properties.

Establishing design rules to reduce the infinite molecular design space to obtain favorable electronic properties has been a focus of many groups.[14] Synthesizing novel compounds and fabricating devices in a "guess and check" manner would certainly be both costly and time consuming. One of the first design rules established focused on damping long axis intermolecular motions.[21] The long axis phonon was first measured using thermal diffuse electron scattering, which is only visible to the largest amplitude acoustic phonons.[22, 23] The theory was reasonable, the largest amplitude phonon should reasonably contribute more to dynamic disorder than other phonons. Also, a single dynamic disorder dominant phonon meant computationally inexpensive calculations and simple analyses. This led to a focus of new molecules focused on only a single phonon, the long axis phonon.[24–30] It was recently resurrected that an all encompassing single "killer" phonon design rule would be naive in an infinite molecular design space.[14] Indeed, the use of thermal diffuse scattering, a technique that measures a restrictively small number of phonons (sometimes just one), could also reasonably bias the establishment of such a design rule.

For that reason, it is important to have a full picture of the phonon modes. Neutron spectroscopy is unrivaled to probe the phonons for OSMs.[31] Particularly, the inelastic neutron scattering (INS) spectrometer, VISION, at Oak Ridge National Laboratory (ORNL) is the best in its class. INS is a simple non-destructive spectroscopy technique that bombards the sample with neutrons. The neutron loses (or gains) energy and momentum from the neutron to the nuclei of the material.[32] That energy and momentum exchange activates a phonon mode, and the recorded scattering events creates the pDOS. INS is not disadvantaged by optical selection rules or near Γ-point measurements. Furthermore, neutrons have a strong interaction with hydrogen atoms, which are abundant in hydrocarbon molecules. This allows neutron spectroscopy to provide detailed information about the behavior and dynamics of the hydrogen atoms. Neutrons are also sensitive to isotopic composition. By using different isotopes, such as deuterium, neutron spectroscopy can provide selective information about specific parts of a hydrocarbon molecule or probe the effects of substitutions on its properties. The simplicity of the neutron-nucleus interaction also confers simple and accurate computational calculations to the scattering.

To fully understand the INS data, computationally intensive density functional theory

(DFT) is performed. DFT is used to model the INS spectra, with good agreement between the modeled and measured spectra indicating the correct input structure and calculated phonons. The phonons are calculated using the finite displacement supercell method, which calculates the forces between atomic pairs from single small displacements of each individual atom. While this method of phonon calculations is much more computationally expensive than the density functional perturbation theory method, it allows one to calculate the dispersion relation thus including momentum. Momentum is especially important as the low energy phonons ($<$200 cm^{-1}) are more influenced by dispersion than the higher energy phonons, resulting in experimentally under-validated phonons if excluded. Once the structure and phonons are experimentally verified, these parameters can be used to calculate parameters to analyze dynamic disorder and the electronic properties, such as the local and non-local electron-phonon coupling parameters. In all, INS experimentally validates the intensive computational tools allowing the analysis of electronic properties such as the structures and specific phonons which are detrimental to μ.

To understand the theory behind INS, we derive the rate law in terms of the structure factor using Fermi's Golden Rule. The derivations and final formulations can commonly be found citing Squires' text[32] as a reference, and will also be used here. While the Squires text is excellent, I found following/understanding the derivation to be difficult as an early graduate student, and each step is more easily understood by also referencing solid state physics text by both Girvin and Yang, and Ashcroft and Mermin.[33, 34] Therefore the derivation is given here, adapted from all three aforementioned texts, and should be able to be followed after an introductory graduate course in quantum chemistry.

Fermi's Golden Rule is a quantum physical formulation that gives the transition rate from an initial to a final energy state, providing a simple formula for calculating the transition rate between two quantum states based on the strength of the perturbation and the density of states in the final state. The rate is proportional to the product of the density of final states and the matrix element of the perturbation between the initial and final states squared. Assuming a single scattering event, Fermi's golden rule is

$$\Gamma_{if} = \frac{2\pi}{\hbar}\delta(\mathcal{E}_f - \mathcal{E}_i)|M_{if}|^2$$

where $|M_{if}|$ is the matrix element of the perturbation between the initial and final states with the interaction Hamiltonian, and $\mathcal{E}_i$ and $\mathcal{E}_f$ are the eigenvalues of those states, respectively.

To begin, the total Hamiltonian is defined, which includes the material system of interest and the neutron used to probe said material,

$$H_{tot} = H_{mat} + H_N + H_{int}$$

where H_{mat} is the material Hamiltonian, $\mathrm{H}_N = P_N^2/2M_N$ is the kinetic energy Hamiltonian of the probing neutron, and H_{int} is the interaction Hamiltonian between the material and neutron. The initial state of the total system is

$$\Psi_i(\vec{R}, \{\vec{r}\}) = \psi_{\vec{p}}(\vec{R})\phi_i(\{\vec{r}\})$$

where $\vec{R}$ is the neutron coordinates and $\{\vec{r}\}$ is the set of atomic coordinates for all atoms in the material system. The initial state of the neutron is taken as a plane wave,

$$\psi_{\vec{p}}(\vec{R}) = \frac{1}{\sqrt{L^3}} e^{i\vec{p}\cdot\vec{R}}$$

After scattering, the final state of the system is

$$\Psi_f = \psi_{\vec{p}'}(\vec{R})\phi_f(\{\vec{r}\})$$

The initial and final energies of the system is the neutron kinetic energy and crystal energy,

$$\mathcal{E}_i = \frac{\hbar^2 p^2}{2M_N} + E_i$$
$$\mathcal{E}_f = \frac{\hbar^2 p'^2}{2M_N} + E_f$$

Thus the matrix element in Fermi's golden rule for the neutron perturbation of the crystal with initial and final states is

$$M_{if} = \langle \Psi_f | H_{int} | \Psi_i \rangle$$

which results in

$$\Gamma_{if} = \frac{2\pi}{\hbar}\delta(\mathcal{E}_f - \mathcal{E}_i)\langle \Psi_f | H_{int} | \Psi_i \rangle^2$$

We can take the difference of the final and initial system energies,

$$\mathcal{E}_f - \mathcal{E}_i = \frac{\hbar^2}{2M_N}(p'^2 - p^2) + E_f - E_i$$

where the perturbation to the final state is equal to the energy lost by the neutron,

$$\frac{\hbar^2}{2M_N}(p^2 - p'^2) = \hbar\omega$$

Replacing the terms results in

$$\Gamma_{if} = \frac{2\pi}{\hbar}\delta(E_f - E_i - \hbar\omega)\langle\Psi_f|H_{int}|\Psi_i\rangle^2$$

The delta function constitutes the conservation of energy, as E_f and E_i are the final and initial energy, respectively, and $\hbar\omega$ is the energy lost by the neutron. Depending on temperature, $\hbar\omega$ can be negative if the neutron absorbs energy from some initial state of the material. Therefore, the average of the ensemble of the transition rate should be taken over all initial states, and the neutron scattering rate from $\vec{p}$ to $\vec{p}'$ is,

$$\Gamma_{\vec{p}\vec{p}'} = \frac{1}{Z}\sum_{i,f} e^{-\beta E_i}\Gamma_{if}$$

where $Z=\sum_i e^{-\beta E_i}$ is the partition function that summarizes the distribution of energy among the different states and $\beta = 1/k_B T$ where k_B is the Boltzmann constant.

The initial and final states of the system can be substituted into the matrix element,

$$\langle\Psi_f|H_{int}|\Psi_i\rangle = \langle\psi_{\vec{p}'}(\vec{R})\phi_f(\{\vec{r}\})|H_{int}|\psi_{\vec{p}}(\vec{R})\phi_i(\{\vec{r}\})\rangle$$

where we will then sum through the overlap of the final and initial neutron states,

$$\langle\Psi_f|H_{int}|\Psi_i\rangle = \frac{1}{L^3}\int e^{-i\vec{p}'\cdot\vec{R}}\langle\phi_f|H_{int}|\phi_i\rangle e^{i\vec{p}\cdot\vec{R}}d^3\vec{R}$$

Since the neutron interaction with the nucleus via the strong force is so short ranged, H_{int} can be approximated with a delta function,

$$H_{int} \approx \alpha\sum_{j=1}^{N}\delta^3(\vec{R} - \vec{r_j})$$

where α is related to the strength of the interaction, and for a crystal,

$$\vec{r}_j = \vec{R}_j + \vec{u}_j$$

where $\vec{r}_j$ is the instantaneous atomic position at some displacement $\vec{u}_j$ and $\vec{R}_j$ is the lattice site. The matrix element then becomes

$$\langle\Psi_f|H_{int}|\Psi_i\rangle = \frac{1}{L^3}\int e^{-i\vec{p'}\cdot\vec{R}}\langle\phi_f|\alpha\sum_j \delta^3(\vec{R}-\vec{r_j})|\phi_i\rangle e^{i\vec{p}\cdot\vec{R}}d^3\vec{R}$$

$$\langle\Psi_f|H_{int}|\Psi_i\rangle = \frac{1}{L^3}\langle\phi_f|\alpha\sum_{j=1}^{N} e^{-i\vec{q}\cdot\vec{r}_j}|\phi_i\rangle$$

The ensemble average of Fermi's golden rule can now be written as

$$\Gamma_{\vec{p}\vec{p'}} = \frac{1}{Z}\sum_{i,f} e^{-\beta E_i}\frac{2\pi}{\hbar}\delta(E_f - E_i - \hbar\omega)(\frac{1}{L^3}\langle\phi_f|\alpha\sum_{j=1}^{N} e^{-i\vec{q}\cdot\vec{r}_j}|\phi_i\rangle)^2$$

$$= \frac{2\pi\alpha^2}{\hbar L^6}\sum_{i,f}\delta(E_f - E_i - \hbar\omega)\frac{e^{-\beta E_i}}{Z}\sum_{j,k=1}^{N}\langle\phi_i|e^{i\vec{q}\cdot\vec{r}_j}|\phi_f\rangle\langle\phi_f|e^{-i\vec{q}\cdot\vec{r}_k}|\phi_i\rangle$$

If not for the delta function, the transition rate can be simplified further by using the completeness relation, $\sum_f |\phi_f\rangle\langle\phi_f| = 1$. The delta function can be transformed using the exponential representation of the Dirac delta function,

$$\delta(E_f - E_i - \hbar\omega) = \frac{1}{2\pi\hbar}\int_{-\infty}^{\infty} e^{-i(E_f - E_i)t/\hbar}e^{+i\omega t}\,dt$$

wherein the transition rate becomes

$$\Gamma_{\vec{p}\vec{p'}} = \frac{\alpha^2}{\hbar^2 L^6}\sum_{i,f}\frac{e^{-\beta E_i}}{Z}\int_{-\infty}^{\infty} e^{+i\omega t}\,dt\sum_{j,k=1}^{N}\langle\phi_i|e^{i\vec{q}\cdot\vec{r}_j}e^{-i(E_f - E_i)t/\hbar}e^{-i\vec{q}\cdot\vec{r}_k}|\phi_i\rangle$$

$$= \frac{\alpha^2}{\hbar^2 L^6}\sum_{i,f}\frac{e^{-\beta E_i}}{Z}\int_{-\infty}^{\infty} e^{+i\omega t}\,dt\sum_{j,k=1}^{N}\langle\phi_i|e^{iE_i t/\hbar}e^{i\vec{q}\cdot\vec{r}_j}e^{-iE_f t/\hbar}e^{-i\vec{q}\cdot\vec{r}_k}|\phi_i\rangle$$

The transition rate is simplified further by using both $H|\phi_f\rangle = E_f|\phi_f\rangle$ and $H|\phi_i\rangle = E_i|\phi_i\rangle$, and the Heisenberg representation of the jth atom, $\vec{r}_j(t) = e^{iHt/\hbar}\vec{r}_j e^{-iHt/\hbar}$, resulting in

$$\Gamma_{\vec{p}\vec{p'}} = \frac{\alpha^2}{\hbar^2 L^6}\sum_{i,f}\frac{e^{-\beta E_i}}{Z}\int_{-\infty}^{\infty} e^{+i\omega t}\,dt\sum_{j,k=1}^{N}\langle\phi_i|e^{i\vec{q}\cdot\vec{r}_j t}e^{-i\vec{q}\cdot\vec{r}_k}|\phi_i\rangle$$

The transition rate can be written in terms of the dynamical structure factor, $S(\vec{q},\omega)$. $S(\vec{q},\omega)$ gives information about the particles correlations and their timer evolution, considering correlations in space and time. $S(\vec{q},\omega)$ is derived from the van Hove time-dependent pair correlation function. The Fourier transform of the van Hove function in space gives the intermediate scattering function, and the Fourier transform in time of the intermediate scattering function gives

$$S(\vec{q},\omega) = \frac{1}{N}\int_{-\infty}^{\infty} e^{+i\omega t}\,dt \sum_{j,k=1}^{N} \langle\langle e^{i\vec{q}\cdot\vec{r}_j t} e^{-i\vec{q}\cdot\vec{r}_k(0)}\rangle\rangle$$

where $\langle\langle\ \rangle\rangle$ means to take the ensemble average over all possible $|\phi_i\rangle$ with Boltzmann weighing factors. Finally, the transition rate can be written in terms of the equilibrium correlations

$$\Gamma_{\vec{p}\vec{p}'} = \frac{N\alpha^2}{\hbar^2 L^6} S(\vec{q},\omega).$$

This work has used INS heavily to study the electronic properties of acenes and acene derivatives. The plan for this dissertation was always to work on building a sample environment on VISION in order to gain insight into the excited state pDOS. Therefore, the plan was to move to ORNL after the first two years at UC Davis. The time spent at ORNL was funded by Office of Science Graduate Student Research (SCGSR) program, of which the program required participants to be advanced to PhD candidacy. Therefore, the first few years were spent doing computational studies on μ for OSMs while preparing for the qualifying exam. The later years were spent working on designing, building, and using an optical excitation sample environment for the VISION spectrometer.

The work described in chapter 2 begins with the computational studies on charge transport for OSMs. The computational workflow for the intensive DFT calculations were developed by a previous graduate student in the group, Dr. Thomas Harrelson.[10] Two sets of OSMs were studied, one set consisting of brick-wall stacked acenes, and the other herringbone stacked molecules. The brick-wall stacked acenes had similar 5 benzene ring backbones, and large side chains. The backbones had minor substitutions to include sulfurs and fluorines. With each sequential substition, μ increased substantially. For molecules with surfur and flourine substituted into the backbone, the side chain was also reduced by removing an ethyl group, which maintained nearly identical brickwall molecular packing.[35, 36] Herringbone type packed materials are also included in this study. Different molecular packing can influence J and thus μ, as the magnitude of J is highly dependent on the relative positions of the molecules in the unit cell. Rubrene, for example, forms monoclinic, triclinic, or orthorhombic polymorphs, with only the orthorhombic polymorph having high μ.[37] The desirable molecular packing for high μ is the one which provides isotropic transport wherein J between distinct molecular pairs are similar,[24] most easily achieved with herringbone packed materials with three distinct transport directions, compared to brickwall packed materials with two distinct directions.[17] The herringbone materials included two molecules sharing the same core with the addition of long side chains on the other. The addition of side chains also had a substantial increase to μ. A third herringbone type acene derivative, rubrene, was studied as it holds the record for highest μ. Phonons were calculated using DFT, and then used to model the INS spectra and compared with the measured INS spectra. The comparison allowed an experimental validation of the structure and dynamics of the studied materials, resulting in confidence of the calculated electron-phonon coupling parameters and μ. The main point of this paper posited that accurate calculation of the phonons were required to accurately calculate μ, and that accurate calculations were required to establish any high μ design rules. The only way to have accurately calculated phonons were to include phonon momentum, and thus INS was necessary to validate the calculations, as opposed to optical techniques without momemtum transfer. Also, this chapter opposes the view of a single long axis phonon dominating the fluctuations to J being the sole "killer" phonon.[21] With the accurate calculations, we find that the minor atomic and molecular changes between the molecules provided insight into the changes in the phonon spectrum and how these changes damp certain motions to increase μ.

Chapters 3-5 are papers from the work at ORNL. Chapter 3 describes a simultaneous side-project for a sample changer for the VISION spectrometer. The VISION spectrometer did not have a sample changer, so single samples would be lowered into the closed-cycle refrigerator (CCR). Once the measurement was complete, the samples would need to be manually extracted and a new sample lowered for cooling and subsequent measurement, spending time, energy, and helium for cooling unnecessarily. Since this work required mechanical motion within the CCR, of which the optical excitation sample environment discussed in chapter 4 would also use, this project had transferable cryogenic design principles. The sample changer uses stepper motors to control sample selection, and sample positioning. The sample needed to be lowered into the neutron beam with a distance great enough to avoid the other samples obstructing the scattered neutrons to the detectors. This was accomplished using a push rod system (referred to as a lance) and long extension springs to lower samples to the beam position, and return samples to its non-obstructing position. The design allowed 4 samples to be cooled at once, saving cooling time and helium, and measured individually.

Chapter 4 details the design and test cases for two optical excitation sample environments. Many photosensitive materials can take advantage of an in-situ photochemistry system for INS, such as optically activated catalyst, photosynthetic materials, non-linear optical materials, and photovoltaics. The first of the two designs is a passive sample stick with no mechanical motion, and uses a high power LED directly above the sample in the CCR. The internals of the sample stick are evacuated of atmosphere to stop moisture condensing on the optical windows and reduce optical transmission. To test the passive stick, an acene was sandwiched between two quartz sheets. The LED wavelength used causes these types of materials to undergo a dimerization, wherein neighboring molecules fuse together to form a dimer. The dimerization is evidenced in the INS data, showing the superposition of spectra from the single molecules and its dimer. The passive stick is simple enough to be able to modified to measure many different sample loading schemes, leaving the door open for more complex experiments. The other sample stick was an active system referred to as the "tumbler" system, which used stepper motors to rotate a sample container. As light has a penetration depth in the order of microns, and neutrons penetrate in the order of millimeters, this mismatch would weigh the superposition of INS spectra towards non-illuminated sample. Therefore, the mixing system uses aluminum paddles within a sample container mounted horizontally, and rotates it to continuously drop powdered sample into the laser. The rotating sample container has an optical window for a laser to transmit through. The laser is collimated and the laser is injected to the sample through a combination of optical windows and mirrors, and was directed with a kinematic mirror. The tumbler sample stick was tested with 405 nm 3D printer resin and a 405 nm laser. The INS measurement for the in-situ photoreacted material for both sample sticks were verified using Raman scattering.

In chapter 5, we use the tumbler to study two acenes with 4 and 5 fused benzene rings, tetracene and pentacene, respectively. These acenes undergo singlet fission (SF), the conversion of a singlet exciton into a pair of triplet excitons. With the theoretical maximum efficiency of single junction photovoltaics being capped at 33.7% by the Shockley-Queisser limit,[38] SF is alluring as a potential avenue for overcoming such a limit. Tetracene and pentacene are model materials for studying the SF mechanism. The electronic structure of tetracene is such that the energy of the first level photoexcited singlet is lower than that of a pair of triplet excitons.[39] Despite the endoergic SF property, SF still occurs in tetracene with near unity quantum efficiency, even at cryogenic temperature.[40] The additional fused benzene in pentacene changes the electronic structure wherein the exciton states results in exogeric SF, also proceeding with near unity quantum efficiency. Questions remain about how the excited singlet is obtaining the energy to proceed with SF in tetracene. The tumbler sample stick described in chapter 4 is used and measures the phonons while illuminating these samples with two lasers of different wavelengths, showing minor changes in the spectra indicating structural changes from the excitons. DFT calcuations that include the exciton state in tetracene are used to compare with the experimental spectra, verifying the atomic structure and changes due to the exciton formation. The experimentally verified structure is then used in time-dependent DFT to calculate changes to the electronic structure due to the excimer formation, finding that the electronic states shift towards to favorable levels for SF to proceed without additional energy in tetracene.

Finally, chapter 6 details the different designs considered and tested for the optical excitation sample environments detailed in chapter 4.

BIBLIOGRAPHY

(1) Kelley, T. W.; Baude, P. F.; Gerlach, C.; Ender, D. E.; Muyres, D.; Haase, M. A.; Vogel, D. E.; Theiss, S. D. *Chemistry of Materials* **2004**, *16*, 4413–4422.

(2) Loo, Y.-l.; Mcculloch, I.; Editors, G. *MRS Bulletin* **2008**, *33*, 653–662.

(3) Forrest, S. R. *Nature* **2004**, *428*, 911–918.

(4) Luppi, B. T.; Majak, D.; Gupta, M.; Rivard, E.; Shankar, K. *Journal of Materials Chemistry A* **2019**, *7*, 2445–2463.

(5) Sirringhaus, H. *Advanced Materials* **2014**, *26*, 1319–1335.

(6) Troisi, A.; Orlandi, G. *Journal of Physical Chemistry A* **2006**, *110*, 4065–4070.

(7) Ciuchi, S.; Fratini, S.; Mayou, D. *Physical Review B - Condensed Matter and Materials Physics* **2011**, *83*, 1–4.

(8) Fratini, S.; Ciuchi, S.; Mayou, D.; De Laissardière, G. T.; Troisi, A. *Nature Materials* **2017**, *16*, 998–1002.

(9) Fratini, S.; Ciuchi, S. *arXiv* **2019**, *013001*, 1–14.

(10) Harrelson, T. F. et al. *Materials Horizons* **2019**, *6*, 182–191.

(11) Vong, D.; Nematiaram, T.; Dettmann, M. A.; Murrey, T. L.; Cavalcante, L. S.; Gurses, S. M.; Radhakrishnan, D.; Daemen, L. L.; Anthony, J. E.; Koski, K. J.; Kronawitter, C. X.; Troisi, A.; Moulé, A. J. *Journal of Physical Chemistry Letters* **2022**, *13*, 5530–5537.

(12) Greenwood, D. M. *Proceedings of the Physical Society.* **1958**, *71.*

(13) Kubo, R. *Journal of the Physical Society of Japan.* **1957**, *12(6).*

(14) Dettmann, M. A.; Cavalcante, L. S. R.; Magdaleno, C. A.; Moulé, A. J. *Advanced Functional Materials* **2023**, *2213370*, 2213370.

(15) Mikhnenko, O. V.; Blom, P. W.; Nguyen, T. Q. *Energy and Environmental Science* **2015**, *8*, 1867–1888.

(16) Deng, W. Q.; Goddard, W. A. *Journal of Physical Chemistry B* **2004**, *108*, 8614–8621.

(17) Schweicher, G.; Olivier, Y.; Lemaur, V.; Geerts, Y. H. *Israel Journal of Chemistry* **2014**, *54*, 595–620.

(18) Geacintov, N. E.; Burgos, J.; Pope, M.; Strom, C. *Chemical Physics Letters* **1971**, *11*, 504–508.

(19) Sebastian, L.; Weiser, G.; Bassler, H. *Chemical Physics* **1981**, *61*, 125–135.

(20) Brown-Altvater, F.; Antonius, G.; Rangel, T.; Giantomassi, M.; Draxl, C.; Gonze, X.; Louie, S. G.; Neaton, J. B. *Physical Review B* **2020**, *101*, 1–12.

(21) Schweicher, G. et al. *Advanced Materials* **2019**, *31*, 1902407.

(22) Eggeman, A. S.; Illig, S.; Troisi, A.; Sirringhaus, H.; Midgley, P. A. *Nature Materials* **2013**, *12*, 1045–1049.

(23) Illig, S.; Eggeman, A. S.; Troisi, A.; Jiang, L.; Warwick, C.; Nikolka, M.; Schweicher, G.; Yeates, S. G.; Henri Geerts, Y.; Anthony, J. E.; Sirringhaus, H. *Nature Communications* **2016**, *7*, 1–10.

(24) Fratini, S.; Nikolka, M.; Salleo, A.; Schweicher, G.; Sirringhaus, H. *Nature Materials* **2020**, *19*, 491–502.

(25) Okamoto, T.; Okamoto, T.; Okamoto, T.; Yu, C. P.; Mitsui, C.; Yamagishi, M.; Ishii, H.; Takeya, J.; Takeya, J.; Takeya, J. *Journal of the American Chemical Society* **2020**, *142*, 9083–9096.

(26) Sawabe, C.; Kumagai, S.; Mitani, M.; Ishii, H.; Yamagishi, M.; Sagayama, H.; Kumai, R.; Sato, H.; Takeya, J.; Okamoto, T. *Journal of Materials Chemistry C* **2020**, *8*, 14172–14179.

(27) Yamamoto, A.; Murata, Y.; Mitsui, C.; Ishii, H.; Yamagishi, M.; Yano, M.; Sato, H.; Yamano, A.; Takeya, J.; Okamoto, T. *Advanced Science* **2018**, *5*, 1–8.

(28) Mitsui, C. et al. *Journal of Materials Chemistry C* **2017**, *5*, 1903–1909.

(29) Okamoto, T.; Mitsui, C.; Yamagishi, M.; Nakahara, K.; Soeda, J.; Hirose, Y.; Miwa, K.; Sato, H.; Yamano, A.; Matsushita, T.; Uemura, T.; Takeya, J. *Advanced Materials* **2013**, *25*, 6392–6397.

(30) Mitsui, C.; Okamoto, T.; Yamagishi, M.; Tsurumi, J.; Yoshimoto, K.; Nakahara, K.; Soeda, J.; Hirose, Y.; Sato, H.; Yamano, A.; Uemura, T.; Takeya, J. *Advanced Materials* **2014**, *26*, 4546–4551.

(31) Cavaye, H. *Angewandte Chemie - International Edition* **2019**, *58*, 9338–9346.

(32) Squires, G. L., *Introduction to the Theory of Thermal Neutron Scattering*, 3rd ed.; Cambridge University Press: 2012.

(33) Girvin, S. M.; Yang, K., *Modern Condensed Matter Physics*; Cambridge University Press: 2019.

(34) Ashcroft, N. W.; Mermin, N. D., *Solid State Physics*; Holt-Saunders: 1976.

(35) Hailey, A. K.; Petty, A. J.; Washbourne, J.; Thorley, K. J.; Parkin, S. R.; Anthony, J. E.; Loo, Y. L. *Advanced Materials* **2017**, *29*, 1–8.

(36) Anthony, J. E. *Chemical Reviews* **2006**, *106*, 5028–5048.

(37) Bergantin, S.; Moret, M. *Crystal Growth and Design* **2012**, *12*, 6035–6041.

(38) Shockley, W.; Queisser, H. *Journal of Applied Physics* **1961**, *32*, 510–519.

(39) Wilson, M. W.; Rao, A.; Johnson, K.; Gélinas, S.; Di Pietro, R.; Clark, J.; Friend, R. H. *Journal of the American Chemical Society* **2013**, *135*, 16680–16688.

(40) Burdett, J. J.; Gosztola, D.; Bardeen, C. J. *Journal of Chemical Physics* **2011**, *135*, DOI: `10.1063/1.3664630`.

Chapter 2

Quantitative Hole Mobility Simulation and Validation in Substituted Acenes

2.1 Acknowledgement

Tahereh Nematiaram performed the electron-phonon coupling calculations. Alessandro Troisi was the adviser for Tahereh Nematiaram. Makena Dettmann and Lucas Cavalcante helped with DFT calculations. Tucker Murrey and Sadi Gurses performed the Fourier transform infrared measurements. Coleman Kronawitter was the adviser for Sadi Gurses. Dhanya Radhakrishnan took the Brillouin scattering measurements. Kristi Koski was the adviser for Dhanya Radhakrishnan. Luke Daemen is the beamline scientist on the neutron spectrometer. Adam Moulé was the PI in charge of this project.

2.2 Introduction

Organic semiconductors (OSC) have undergone rapid development for use in applications such as organic light emitting diodes, transistors, biological and chemical sensors, and wearable and flexible electronics[1–6]. Small molecule OSCs (OSMs) have the highest μ among OSCs because they form extended crystalline domains[7]. Planar molecules, like acenes, are natural building blocks for OSC crystals, but they tend to form polycrystalline morphologies with poor electronic connection across the grain boundaries[8, 9]. Decades of study have shown that non-planar organic molecules consisting of fused aromatic rings with symmetric side chains enable the molecules to:

1. Lock into geometries that may benefit charge transport[10, 11].
2. Form more extended defect free crystalline domains[12, 13].
3. Achieve improved electronic connection through microdomain grain boundaries[14].

Rubrene, C8-BTBT, C8-DNTT, and TIPS-Pentacene are all examples of substituted acenes that have exhibited high hole mobility (μ_h)[15, 16].

The charge transport mechanism in OSMs have attracted great attention[17–21]. There is unanimous consensus that μ cannot be computed accurately using either band theory or a hopping mechanism[22–27]. Here we consider the coupling between charge carriers and molecular motions in the framework of transient localization theory (TLT) in order to calculate dynamic disorder (σ). The coupling leads to large transfer integral fluctuations that dynamically localizes the charge carrier on the ps time scale and thereby reduces μ. The coupling between phonons and charge carriers is accounted for using diagonal (intramolecular) and off-diagonal (intermolecular) terms in the Hamiltonian[24]. Recent theory-experiment[16, 17, 21, 28, 29] and theory-theory[30–32] studies have shown that TLT provides fairly accurate prediction of μ and the trends between molecules.

Recently, μ_h of several OSMs was calculated based on the spectral measurements of σ[16, 21, 33], wherein experimental data was used to validate theoretical calculations. While there is little doubt that the dynamic disorder model correctly accounts for the reduced μ_h, there is disagreement in the literature about how many modes are responsible, how to measure these modes experimentally, or how to model these modes theoretically. This letter examines this problem using a series of three well-studied high μ_h brick-wall type substituted acenes, 6,13-Bis(triisopropylsilylethynyl)(TIPS)-Pentacene, 5,11-Bis(triethylsilylethynyl)anthradithiophene (TESADT), and its fluorinated analogue, diF-TESADT. These molecules form similar crystal structures, yet have measured μ_h increased from <1 cm^2/Vs for TIPS-pentacene[34], to >1 cm^2/Vs in TESADT[35], and to >6 cm^2/Vs for diF-TESADT[36]. We then extend this study beyond brick-wall materials to herringbone type materials, [1]Benzothieno[3,2-b]benzothiophene (BTBT), 2,7-Dioctyl-BTBT (C8-BTBT), and Rubrene; some of which were reported to have a single long-axis mode dominating σ.[21] Here we use density functional theory (DFT) coupled to electron-phonon calculations to determine the contribution to σ, and compare between Γ-point and full Brillouin zone (FBZ) approaches. We find that many of the intra- and inter-molecular phonons across the FBZ contribute to σ, and that no single phonon contributes $>$10% to σ, regardless of molecular packing. A partial mode analysis is then performed linking the structure-property relationship involving molecular changes and the phonons that contribute to σ.

First we characterize the acoustic and optical phonons using Brillouin scattering (0.1–2 cm^{-1}), inelastic neutron scattering (INS) (3–4000 cm^{-1}), Raman (50–1500 cm^{-1}), and Fourier-transformed infrared (FTIR) (600–1600 cm^{-1}) spectroscopies. Next, we model the crystal using a plane wave DFT supercell that simultaneously and accurately reproduces the measured crystal structure and the phonon spectrum. The electron-phonon coupling is calculated from the DFT model that closely matches the experimental spectrum. Finally, we consider the information contained in each measured spectrum and demonstrate that the isotropic optical spectra not only has missing modes due to selection rules, but also inadequately samples the Brillouin zone, leading to a limited mode analysis and over-assignment of σ. Finally, we compare predictions of μ_h.

2.3 Methods

2.3.1 Brillouin scattering measurement

Brillouin scattering was acquired with a 3×3-pass Sandercock scanning tandem Fabry-Perot interferometer (TFP-1) with a Coherent Verdi V6 Nd:YVO4 laser ($\lambda_0 = 532.15$ nm). The laser was focused onto the TIPS-Pentacene crystal with ~10-15 mW power and with acquisition times from 8-24 hours per spectrum. The mirror spacing of the etalons was 3 mm (90R) or 6 mm (180) with a scan rate of 550 giving an effective spectral window of 50 GHz and 25 GHz, respectively. The narrower spectral window was displayed in Figure 1 in the main text. No other peaks were found at higher frequencies, which indicates that this measurement captured the principle acoustic phonon modes, the translational modes along the molecule's axes. Entrance pinholes were at 450 μm with an exit pinhole of

700 μm providing an overall system finesse of 70 (180) to 140 (90R). Brillouin scattering spectra were not simulated using DFT given the computational expense associated with a box size of 1000's of molecules.

Brillouin scattering measurements of TIPS-Pentacene (Fig. 2.1) was acquired in two geometries with respect to the crystalline axis. The 180° (black curve) geometry observes the directly reflected signal while the 90° (red curve) geometry observes a signal reflected to an angle of 90°. On a fundamental level, Brillouin scattering results from the interaction of a photon with the acoustic phonons of a material on the mesoscopic scale (∼0 to a few cm^{-1})[37]. Thus the principal acoustic phonons that produce the largest molecular displacement are measured directly using Brillouin scattering. A Brillouin spectrum has a single elastically scattered component, which is blocked in these measurements by a shutter, surrounded by Stokes and Anti-Stokes scattering peaks. Each peak consists of one longitudinal or quasi-longitudinal phonon mode, and depending on the geometry and symmetry of the measurement, one or two quasi-transverse acoustic modes. These measurements each show only one longitudinal or quasi-longitudinal mode. The Brillouin frequency shift ($\Delta\nu$) is related to the acoustic sound velocities, V by:

$$\Delta\nu(Hz) = \pm\frac{2nV}{\lambda_o}\sin\frac{\theta}{2} \tag{2.1}$$

where n is the refractive index, θ is the scattering angle as measured inside the sample, and λ_0 is the free-space wavelength of the laser. The geometries of 180° and 90° measure the same sound velocities, thus we can determine n by the frequency shift from both measurements:

$$n = \left(\frac{1}{\sqrt{2}}\right)\left(1-\left(\frac{\nu_{90r}}{\nu_{180}}\right)^2\right)^{-1/2} \tag{2.2}$$

The Brillouin frequency shift in 180° is 12.90 +/- 0.1 GHz. Sound velocities from these measurements of TIPS-Pentacene show 2451 m/s. Assuming a density of 1.10 g/cm^3, this gives a stiffness of c_{11} = 6.61 GPa as calculated from:

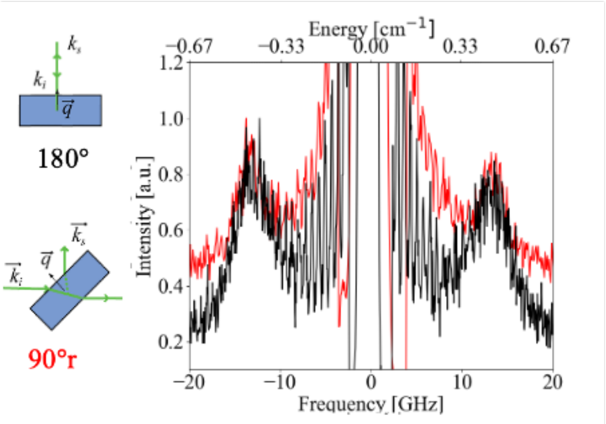

Figure 2.1. Brillouin scattering in 180° (top left, black spectrum) and 90°r (bottom left, red spectrum) scattering geometries. Only one longitudinal acoustic mode is observed. Details are given in the manuscript.

$$V_L = \sqrt{\frac{c_{11}}{\rho}} \tag{2.3}$$

Converting from a frequency scale to an energy scale shows that the principal acoustic phonon in TIPS-Pentacene corresponds to $\sim$50 μeV or 0.43 cm^{-1}. Notably, this energy is at least an order of magnitude below the phonon energies measured by INS, FTIR, Raman or Terahertz spectroscopies. This acoustic phonon mode has the lowest energy, longest wavelength, and largest displacement of any phonon mode. Therefore, this phonon mode is the most likely molecular motion to be measured using diffuse scattering techniques, and the principal acoustic phonon cannot be measured using Terahertz spectroscopy with energy above 20 cm^{-1}[21]. The motions of the acoustic phonon modes measured using Brillouin scattering are much slower than the charge hopping events in OSCs and therefore do not contribute to off-diagonal σ or reduce μ_h. Brillouin scattering measured on Rubrene[38] show multiple acoustic modes while Rubrene has measured μ_h >10 cm^2/Vs. Despite any detrimental actions of these modes, high μ_h is retained.

2.3.2 INS, Raman, and FTIR measurement and modeling

Inelastic neutron scattering spectrum was measured using the VISION spectrometer at the Spallation Neutron Source at Oak Ridge National Laboratory (ORNL). VISION samples were loaded in vanadium sample holders inside a dry helium glove box. An empty sample holder was measured and subtracted from the measured spectra. All data sets were collected at 5K.

A Bruker VERTEX 70 FTIR spectrometer equipped with a liquid nitrogen cooled MCT detector was used to collect reflectance FTIR spectra on powdered TIPS-Pentacene. The sample was placed in a multi-reflection ATR crystal (ZnSe) with a Specac's Gateway ATR accessory set to an incidence angle of 45 degrees. The spectrum represents the average of 128 scans.

Computed inelastic neutron scattering spectra were produced similar to our previously developed plane-wave density functional theory model as implemented in VASP[39, 40] with PAW pseudopotentials[41], with a decrease of the maximum force criteria for the ionic relaxation loop to 0.002 eV/Å and the electronic energy converged to 10^{-8} eV. The optPBE[42, 43] functional was used in describing the exchange-correlation along with the non-local vdW[44] correlation functional for dispersion interactions. The basis set plane wave energy cutoff was increased to 800 eV, with a $4\times4\times2$ Γ-centered k-point mesh for the substituted acenes, and $2\times3\times2$, $3\times2\times1$, and $2\times2\times2$ k-point mesh for BTBT, C8-BTBT, and Rubrene, respectively. The crystallography files used in the computation are from X-ray diffraction measurements and can be found in crystallography databases.[10, 45–48]. Phonopy[49] was used to calculate the vibrational modes and energies on a $2\times2\times1$ supercell for the substituted acenes, and $1\times2\times2$,$2\times2\times1$, and $1\times1\times1$ for BTBT, C8-BTBT, and Rubrene, respectively, using the finite displacement method (more in the next subsection), wherein symmetry inequivalent atoms are displaced by 0.001 Å and restoring forces are calculated. The supercell sizes ensure a minimum of 10 Å per crystallographic length and 4 molecules per supercell, which we have found is necessary to converge the calculation. The INS spectrum was produced using the energies and forces from DFT using the oCLIMAX[50] tool provided by Oak Ridge National Laboratory. oCLIMAX inputs specific geometry considerations based on the VISION beam line. Phonon k-points in Phonopy were increased until INS spectral convergence was reached.

Γ-point phonon eigenvectors and frequencies and Born effective-charge tensors were calculated in VASP using the same parameters listed in the INS model. The DFT calculated[51] off-resonant isotropic Raman intensities were calculated using the Python program developed by Fonari and Stauffer.[52] FTIR intensities were calculated using the Phonopy-Spectroscopy methodology by Skelton.[53]

2.4 Results and Discussion

We compare four different spectroscopic techniques that measure vibrational modes for TIPS-Pentacene in Fig. 2.2. We also highlight the energy region that is most important for σ on the time scale relevant for μ_h[17, 54, 55]. This energy region is important because it represents the modes that are populated at room temperature and could thus contribute to σ. Brillouin scattering (maroon) measures the acoustics modes of molecules, wherein details of the Brillouin scattering result are shown in Fig. 2.1. Although the long-axis acoustic mode has been shown to predict μ_h based on Boltzmann transport in OSMs with plane mirror symmetry,[56] the motions of the acoustic phonon modes measured using Brillouin scattering are much slower than the charge hopping events in OSCs and therefore do not contribute to off-diagonal σ or reduce μ_h.

The experimental and computed spectra for FTIR and Raman of TIPS-Pentacene (Fig. A.2 top-left) can be seen in Figs. A.3 and A.4, respectively. Overall, we show good experimental agreement with most peaks present and the modes shifted by not more than 20 cm^{-1} (note Raman was recorded at room temp so the shift was expected). Although the computed Raman spectrum does not reproduce the experimental Raman intensities well, we do show excellent reproducibility in phonon peak position and intensities for FTIR and INS, which uses the Γ-point and the FBZ phonons in the calculations, respectively. Therefore, we find that the phonons are reproduced accurately, but the activities in the Raman spectrum are off from the macroscopic static dielectric tensor calculations.

The INS spectrum (black) in Fig. 2.2 measures a much higher density of low energy modes over a more complete energy range than either Raman (red) or FTIR (blue), due to optical selection rules. The experimental energy range that Raman can access is limited and many of the lower energy vibrational modes that contain the timescales considered most important for charge transport cannot be resolved. Literature measurements of

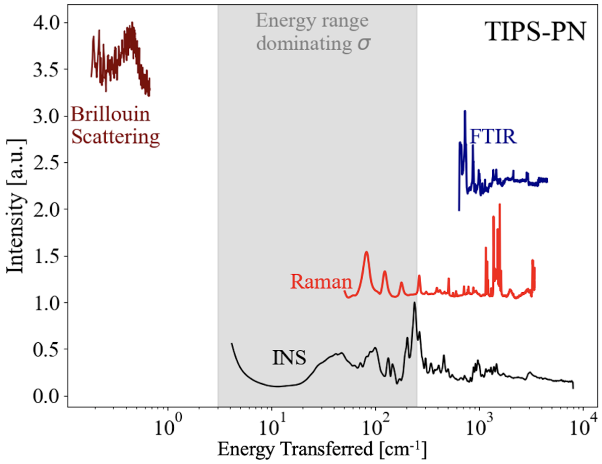

Figure 2.2. Comparison of experimental INS (black), Raman (red), FTIR (blue), and Brillouin scattering (maroon) spectra for TIPS-Pentacene.

low-energy Raman (lower than we could obtain) measured in acenes-based OSMs also depict only a low density of low energy modes[20, 57–60]. Typically, FTIR covers a much narrower energy range because of limits in detectors. Recently, Schweicher et al. utilized Terahertz spectroscopy to access those lower energies in related OSMs to compare with the calculated phonons, but the limited number of resolved modes led to an average over-calculation of μ_hs by a factor of $\sim 3\times$[21]. We conclude that experimental validation solely with optical techniques such as Raman, FTIR, or THz spectroscopies, can lead to simulations that under-sample the phonon modes that are critical for charge transport. By comparison, we previously showed that validation to INS alone reproduces experimental μ_hs[16] because all of the modes over the full energy range and FBZ are sampled. However, we note that polarized Raman spectroscopy on single crystals can provide critical information about the anisotropy of polaron states[20, 57] that is impossible to directly probe using INS.

Unlike optical-based spectroscopy, INS has rarely been utilized[61] to study the dynamics in OSCs[62–64]. While low energy Raman has been used to differentiate the phases present in OSMs[65], INS, specifically performed at the VISION spectrometer at Oak Ridge National Laboratory (ORNL), is currently the only instrument that can quantitatively resolve the phonon spectrum over both the entire vibrational energy range (5-5000 cm^{-1}) and k-space. VISION has a spectral brightness two orders of magnitude larger than those of similar instruments, while other INS instruments are also limited to either higher or lower energy ranges[21, 66–69].

We compare INS spectra from a well-known set of three substituted acenes, Figs. 2.3 and top row of A.1, respectively, that share similar brick-wall type stacking. The full INS spectra can be seen in Fig. A.4. The agreement across three-orders of energy between measured and modeled INS shows that the DFT model accurately resolves both the atomic positions and cell dimensions from diffraction experiments, and the atomic dynamics from INS. Studying OSMs with similar core structures should reveal structural motifs that can lead to high μ_h OSM design.

The substituted acenes, TIPS-Pentacene, TESADT, and diF-TESADT, exhibit respective increases in μ_h after molecular and chemical variations on the conjugated core and side-chains. Firstly, benzenes on the terminal ends of the conjugated core in TIPS-Pentacene (Fig. A.1 top-left) are replaced with thiophenes, and a methyl group is removed from each branch of the side chain creating TESADT (Fig. A.1 top-center). Previous research concluded that the sulfur-sulfur interactions provide stability between adjacent neighboring molecules[70], with an increase in μ_h believed to arise from damped long-axis intermolecular motions[71]. Secondly, fluorines replaced a hydrogen atom on each thiophene along the long-axis of the backbone on TESADT, making diF-TESADT (Fig. A.1 top-right). This substitution further increased μ_h. It was reported that C-F polar covalent bonds, S-F dipoles, and H-F hydrogen bonding[72, 73] further dampen motions between neighboring molecules.

A convenient way to visualize the contribution of σ from the phonons is by plotting the spectral density of electron-phonon coupling, as seen in Fig. A.5 for TIPS-Pentacene and TESADT. The spectral densities (S) are computed as explained in Ref. [16]. The INS spectra are overlaid with S in Fig. A.6, showing which phonon modes make a large contribution to σ in the low energy region. Fig. A.7 depicts a number of these phonon modes for TIPS-Pentacene from 20 to 150 cm^{-1} and clearly indicates that most of these modes do not involve long-axis motions. Only the modes shown in Figs. A.7b and A.7c are Γ-point phonons, and therefore observable using optical measurements. As can be

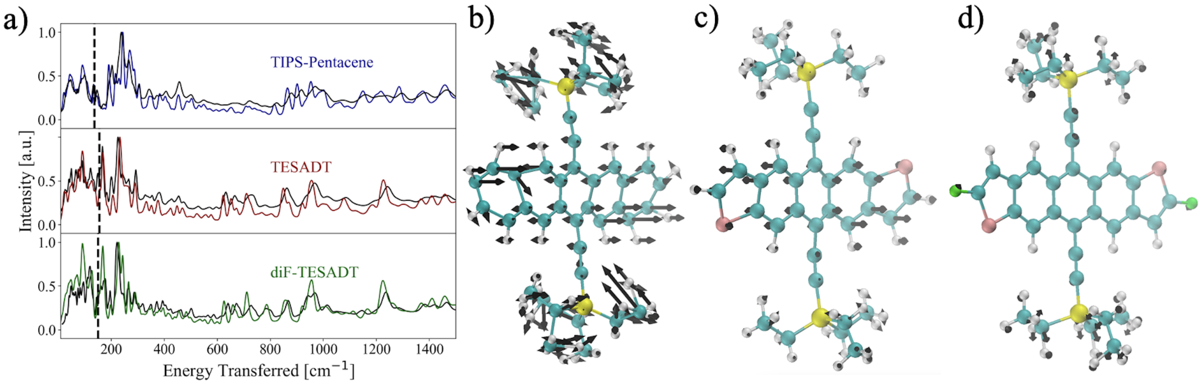

Figure 2.3. a) Experimental INS spectra in solid black for b) TIPS-Pentacene, c) TESADT, and d) diF-TESADT with corresponding optPBE-vdw simulated INS spectra in colored lines. Energy range is from 10-1500 cm^{-1}. Dashed vertical lines in a) highlight the phonon modes shown in b-d with frequencies 136, 155, and 150 cm^{-1}, respectively. Phonon eigenvectors are scaled by 5 for TIPS-Pentacene and 20 for TESADT and diF-TESADT to improve clarity. b-d highlights the effect of chemical change to the molecule on a single series of phonon modes with sizably altered transfer integrals. e-f highlights the modes at 45 and 50 cm^{-1} for BTBT and C8-BTBT, respectively, that show reduced phonon amplitudes.

seen, considering only Γ-point phonons may skew the assessment of σ by leaving out modes that contribute to σ. Even when calculating σ solely at the Γ-point, we found that no single phonon mode is responsible for more than 10% of σ, supporting a similar conclusion from a previous study.[69]

Since the brick-wall type materials in this letter are very similar, having similar structures and stacking motifs, we see phonon modes that can be assigned to similar motions (similar to the well-known C=C stretch at higher energy). In Fig. A.6, the delta functions in the INS spectra overlain with S highlight phonons with appreciable contribution to σ, while Figs. A.7 and A.8 illustrate those delta functions with cartoons of the molecular motion with double-headed phonon arrows. In Fig. 2.3, we highlight a set of molecular motions that are the same, or mostly the same, from Figs. A.7 and A.8. We monitor the effect of minor chemical changes to a particular phonon that had a sizable contribution to σ and show how these phonons change between structures. TIPS-Pentacene has a twist mode for the acene rings at 136 cm^{-1} depicted in Fig. 2.3b. Substituting to an ADT core replaces phenyl rings for end ring thiophenes, which stiffens the ring structure and reduces the amplitude of the twisting mode in TESADT (Fig. 2.3c). These changes reduce

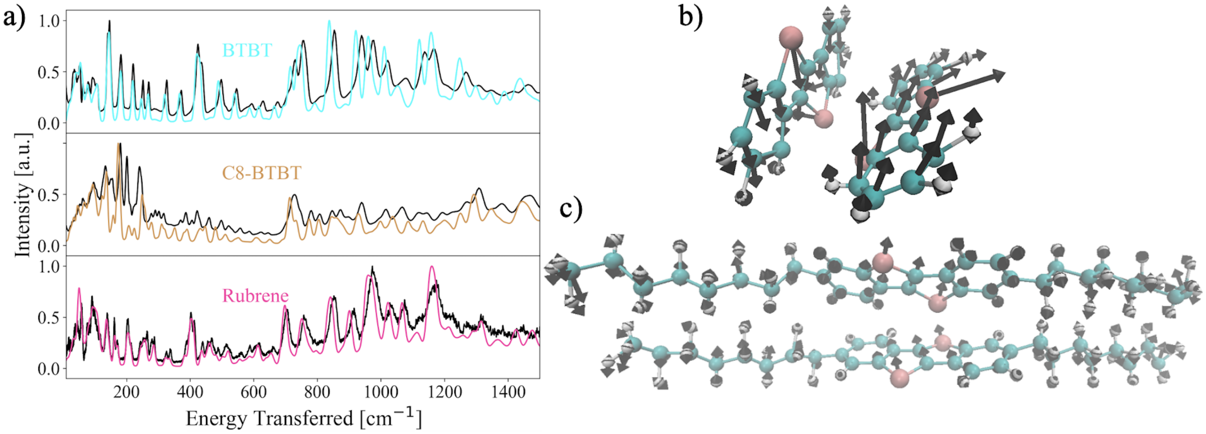

Figure 2.4. a) Experimental INS spectra in solid black for BTBT, C8-BTBT, and Rubrene with corresponding optPBE-vdw simulated INS spectra in colored lines. Energy range is from 10-1500 cm^{-1}.

the absolute magnitude of carbon motions in the backbone in TESADT while the sulfur amplitude is large due to the weak C–S bonds (Fig. A.8d). The total σ in TESADT is lower than for TIPS-Pentacene because there are changes to a variety of modes that combine to reduce the total σ. Further comparing TESADT to diF-TESADT, the addition of fluorine dampens out-of-plane sulfur motions and maintains the stiffened backbone as shown in Fig. 2.3d, with other relevant phonons for diF-TESADT shown in Fig. A.9. We demonstrate that twisting, rotational, or rocking modes that are not along the long-axis can also cause small dynamic changes that have a clear affect on σ.

We now perform a similar analysis on BTBT, C8-BTBT, and Rubrene, with the INS spectra and highlighted molecular motions in Fig. 2.4. Rubrene holds the record for highest μ_h, but does not share chemical or structural motifs with the BTBT molecules. To improve clarity, we show a comparison of the BTBT modes here, but show Rubrene modes in the Appendix A only. First, we note that C8-BTBT exhibits a low temperature polymorphism, while DFT was performed on the room temperature polymorph, leading to poor spectral agreement, particularly above ∼200 cm^{-1}. As we have shown consistent agreement between measured and simulated INS for a number of other OSMs and semiconducting polymers,[74] and since we are interested in the phonons of the room temperature polymorph, the simulated phonons should still provide rough insight into the charge transport relationship. Thus we analyze the change in modes that contribute to σ from addition of the C8 side chains on BTBT. We see that each material contains many peaks in S, Fig. A.14c-f , over a broad range of energy implying that many different phonon modes contribute to σ. In the spectra, the peaks in high energy (e.g. around 1500 cm-1) are also due to carbon–carbon stretch modes as also noted in previous studies.

The INS spectra with S and delta functions overlain are shown in Fig. A.10, while the partial mode analysis of the delta functions are shown in Figs. A.11 and A.12 for BTBT and C8-BTBT, respectively, which highlights some of the motions with sizable σ. BTBT has a large number of modes contributing to σ, including translation, flexing, and twisting. We again notice large amplitude sulfur motions from the weak C–S bonds arising consistently in the modes with energies above pure translation. For C8-BTBT, the long-axis mode shown in Fig. A.12a does indeed have an appreciable contribution to σ, but there are many other modes that are as much so or more impactful that should not be overlooked, as supported in Figs. A.14c and A.14d. The motions in C8-BTBT are similar to BTBT, but the addition of the long C8 side chains contribute to lock in neighboring molecules resulting in reduced amplitude in overall displacements, and reduction of the sulfur motions, highlighted in Figs. 2e and 2f. Regardless of crystal packing, the minimum potential energy well through which a polaron travels is affected by many polarons that increase σ and thereby dynamically localize the polaron. No single mode dominates.

Table 1 summarizes the results and showcases a quantitative comparison between simulations and experiment. In the worse case, computed μ_h is larger than for the FBZ calculations by over 100% because many phonon modes are missing from the Γ-point analysis. In some cases, we see better predictions to μ_h with Γ-point against FBZ, notably with Rubrene. While for most molecules the FBZ simulation is consistently more accurately compared to measurements than Γ-point, we are not sure why the calculated mobility of FBZ Rubrene is so much lower than the Γ-point. Looking at Table 1, σ increases from 36.4 meV to 50.6 meV in the B pairs, but only from 9.5 meV to 10.1 meV in the C pairs. This implies that the Γ-point simulation misses an important contribution to coupled motion between these two directions. We cannot say how this coupling changed. No one (including us) has developed a first principles method to improve μ_h using a phonons

Table 2.1. Computed parameters for the organic small molecules. Top row for each material are for pairs A and bottom row is pairs B for brick-wall type materials and pairs B and C for herringbone type materials. List of materials, transfer integrals J [meV], molecular pairs, band renormalization factor f, local dynamic disorder $\boldsymbol{\sigma_{local}}$ [meV], non-local dynamic disorder calculated considering only gamma point phonons $\boldsymbol{\sigma_{\Gamma}}$ [meV] and full Brillouin zone phonons $\boldsymbol{\sigma_{FBZ}}$ [meV] at 300 K, and respective mobilities [cm^2/Vs] computed in the framework of transient localization theory along with averaged experimental mobilities [cm^2/Vs] from the high mobility plane. $\boldsymbol{\mu_{exp}}$ for TESADT and diF-TESADT consist of pure isomers in *anti* configuration. DFT calculations were also done on *anti*-configurations. μ_{exp} are pulled from literature sources [34, 35, 73, 75, 76].

Material	J	f	σ_{local}	σ_{Γ}	σ_{FBZ}	μ_{Γ}	μ_{FBZ}	μ_{exp}
diF-TESADT	-198.87	0.59	0.016	40.05	47.54	2.27	2.15	2.2 ± 1.1
	-49.66			22.84	24.27			
TESADT	-172.01	0.61	0.016	43.65	57.13	2.03	1.87	1.2 ± 0.2
	-59.09			27.91	30.14			
TIPS-PN	69.78	0.55	0.011	33.72	43.53	1.06	0.81	0.65 ± 0.35
	1.96			15.22	15.98			
BTBT	113.58	0.43	0.015	30.00	32.28	0.86	0.82	0.024 ± 0.007
	13.26			77.65	81.91			
C8-BTBT	88.01	0.47	0.021	26.18	23.80	1.85	2.55	6.0 ± 1.
	-62.94			54.52	50.06			
Rubrene	147.87	0.65	0.018	36.40	50.64	8.73	4.01	9.25 ± 0.75
	22.69			9.56	10.09			

design rule because there are so many different contributions. This remains an important challenge in the field.

As can be seen from Table 1, there are -9% to 28% relative changes between σ computed using the FBZ phonons and those of only Γ-point phonons. In C8-BTBT, there is a decrease in σ from including the phonon dispersion, which may seem counter-intuitive, but can be explained by the improved convergence of the low frequency lattice modes.[77, 78] This is evidenced by the convergence of S between Γ-point and FBZ seen in Fig. A.14. Since the phonon dispersion is highest in the low energy region (Figs. A.15-A.17), including dispersion has drastic effects on the low frequency phonons, which are considered most important for charge transport. Therefore, one can conclude that methods such as Raman and FTIR spectroscopy that are designed to only probe Γ-point phonons do not contain enough information to reliably parametrize the non-local electron-phonon coupling in these materials. An important notable point is that σ in C8-BTBT is smaller than those of BTBT itself in spite of the reduced order and higher flexibility of alkane bonds. As discussed in recent studies, the attachment of the side chains can shift the vibrational range of the conjugated core toward higher frequencies that cannot be as easily populated at room temperature and do not contribute as effectively to σ.[18, 21]

Accordingly, in the calculation of μ_h for C8-BTBT, only the contribution of low frequency modes in σ is considered. However, the computed μ_h of C8-BTBT tends to be slightly smaller than those reported previously. This can be understood based on the fact that σ in this molecule changes in both directions (as can be seen in Table 1) and that the effect on μ_h goes from negligible in one direction to a factor of 2 in the other, meaning it is an effect that cannot be described by some systematic correction. Lastly, μ_hs computed using the full phonon spectra for BTBT are smaller than those computed with only Γ-point phonons. This behavior is consistent with the rule proposed in Ref. [21] which expects the mobility to be scaled by $\mu \ \alpha \ (\sigma/\mathrm{J})^{-\gamma}$ with $\gamma \approx$ "2" and those of Ref. [79] which predicts a rank correlation of up to ∼ -0.45 between σ and μ_h.

2.5 Conclusions

In summary, application of TLT simulations combined with validated phonon modes is currently the most accurate simulation method for prediction of μ_h. Fig. 2.5 shows predicted μ_h normalized to measured μ_h for this work and other recent publications using different methods and assumptions. The μ_h predictions using the method shown here are consistently closest to measured. We see greater deviation between experimental and predicted mobility for the herringbone compared to brick-wall type materials. This may be because the brick-wall materials synthesized and handled by the Anthony group were of particularly high quality, while herringbone materials were commercially obtained. It

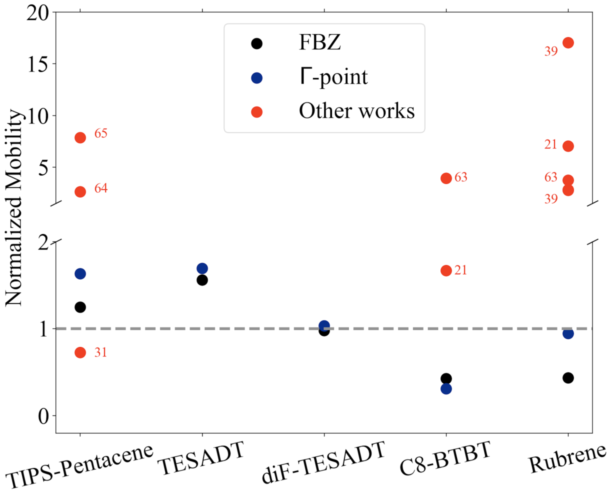

Figure 2.5. Average μ_hs in the high mobility plane normalized by average experimentally measured for FBZ (black) and Γ-point (blue). BTBT has been omitted due to the abnormally large contact resistance leading to low mobility measurements. Red marks are average μ_hs, in the high mobility plane where available, for other work with theories including TLT, Boltzmann transport based acoustic phonon deformation potential, time-dependent wavepacket diffusion, and quantum nuclear tunneling. Gray dashed line indicates computational and experimental unity. Adjacent red numbers for citations.[21, 31, 56, 80–82]

has also been shown that organic field-effect transistors are commonly erroneously used to extract μs much higher than their true intrinsic value.[83] This Figure also shows that FBZ produces a closer prediction to measured that Γ-point for a majority of molecules. The choice of validation data can affect the accuracy of these simulations by enabling measurement of either Γ-point or FBZ data. Regardless of herringbone or brick-wall type stacking, accurate phonons allow for a sequential mode analysis that probes the effect of minor chemical changes and σ significant phonons. The examination of the full phonon spectrum shows that many modes contribute to σ, without any mode contributing more than 10%, and so a design rule focusing on a single phonon mode is unlikely to drastically improve μ_h.

While the calculated μ_hs quantitatively reproduced measured μ_h, these FBZ phonon calculations are limited by the enormous computational expense of DFT. A typical calculation with a 100 atom unit cell costs $> 10^5$ CPU hours on a supercomputer per 2×2×1 supercell. Therefore, DFT cannot model imperfections such as grain boundaries or structural/chemical defects. Rapid screening of theoretical materials based on σ would not be feasible. To overcome this limitation, considerable attention has been focused on computationally cheaper methods. Recent examples include molecular dynamics (MD)[84], density functional based tight binding (DFTB)[85, 86], or a mixture such as quantum mechanics/molecular mechanics (QM/MM)[79], DFT-MD[75, 87], and ChIMES/DFTB[31]. Computationally demanding studies, such as this one, are essential as benchmarks for validating more approximate simulation methods.

Bibliography

(1) Shi, Y. L.; Zhuo, M. P.; Wang, X. D.; Liao, L. S. *ACS Applied Nano Materials* **2020**, *3*, 1080–1097.

(2) Zhang, X.; Dong, H.; Hu, W. *Advanced Materials* **2018**, *30*, 1–34.

(3) Schweicher, G.; Garbay, G.; Jouclas, R.; Vibert, F.; Devaux, F.; Geerts, Y. H. *Advanced Materials* **2020**, *32*, 1905909.

(4) Wang, N.; Yang, A.; Fu, Y.; Li, Y.; Yan, F. *Accounts of Chemical Research* **2019**, *52(2)*, 277–287.

(5) Qian, Y.; Zhang, X.; Xie, L.; Qi, D.; Chandran, B. K.; Chen, X.; Huang, W. *Advanced Materials* **2016**, *28*, 9243–9265.

(6) Wang, Y.; Sun, L.; Wang, C.; Yang, F.; Ren, X.; Zhang, X.; Dong, H.; Hu, W. *Chemical Society Reviews* **2019**, *48*, 1492–1530.

(7) Wang, C.; Dong, H.; Jiang, L.; Hu, W. *Chemical Society Reviews* **2018**, *47*, 422–500.

(8) Horowitz, G.; Hajlaoui, M. E.; Hajlaoui, R. *Journal of Applied Physics* **2000**, *87*, 4456–4463.

(9) Kalb, W. L.; Haas, S.; Krellner, C.; Mathis, T.; Batlogg, B. *Physical Review B - Condensed Matter and Materials Physics* **2010**, *81*, 1–13.

(10) Anthony, J. E.; Brooks, J. S.; Eaton, D. L.; Parkin, S. R.; May, R. V. **2001**, *222*, 1–2.

(11) Payne, M. M.; Odom, S. A.; Parkin, S. R.; Anthony, J. E. *Organic Letters* **2004**, *6*, 3325–3328.

(12) Jurchescu, O. D.; Baas, J.; Palstra, T. T. *Applied Physics Letters* **2004**, *84*, 3061–3063.

(13) Subramanian, S.; Sung, K. P.; Parkin, S. R.; Podzorov, V.; Jackson, T. N.; Anthony, J. E. *Journal of the American Chemical Society* **2008**, *130*, 2706–2707.

(14) Wo, S.; Headrick, R. L.; Anthony, J. E. *Journal of Applied Physics* **2012**, *111*, 073716.

(15) Illig, S.; Eggeman, A. S.; Troisi, A.; Jiang, L.; Warwick, C.; Nikolka, M.; Schweicher, G.; Yeates, S. G.; Henri Geerts, Y.; Anthony, J. E.; Sirringhaus, H. *Nature Communications* **2016**, *7*, 1–10.

(16) Harrelson, T. F. et al. *Materials Horizons* **2019**, *6*, 182–191.

(17) Fratini, S.; Ciuchi, S.; Mayou, D.; De Laissardière, G. T.; Troisi, A. *Nature Materials* **2017**, *16*, 998–1002.

(18) Nematiaram, T.; Troisi, A. *Materials Horizons* **2020**, *7*, 2922–2928.

(19) Fratini, S.; Nikolka, M.; Salleo, A.; Schweicher, G.; Sirringhaus, H. *Nature Materials* **2020**, *19*, 491–502.

(20) Bittle, E. G.; Biacchi, A. J.; Fredin, L. A.; Herzing, A. A.; Allison, T. C.; Hight Walker, A. R.; Gundlach, D. J. *Communications Physics* **2019**, *2*, 29.

(21) Schweicher, G. et al. *Advanced Materials* **2019**, *31*, 1902407.

(22) Ortmann, F.; Bechstedt, F.; Hannewald, K. *Physica Status Solidi (B) Basic Research* **2011**, *248*, 511–525.

(23) Blumberger, J. *Chemical Reviews* **2015**, *115*, 11191–11238.

(24) Giannini, S.; Carof, A.; Ellis, M.; Yang, H.; Ziogos, O. G.; Ghosh, S.; Blumberger, J. *Nature Communications* **2019**, *10*, 1–12.

(25) Wang, L.; Prezhdo, O. V.; Beljonne, D. *Physical Chemistry Chemical Physics* **2015**, *17*, 12395–12406.

(26) Heck, A.; Kranz, J. J.; Kubař, T.; Elstner, M. *Journal of Chemical Theory and Computation* **2015**, *11*, 5068–5082.

(27) Jiang, Y.; Geng, H.; Li, W.; Shuai, Z. *Journal of Chemical Theory and Computation* **2019**, *15*, 1477–1491.

(28) Ruggiero, M. T.; Ciuchi, S.; Fratini, S.; D'Avino, G. *Journal of Physical Chemistry C* **2019**, *123*, 15897–15907.

(29) Ren, X.; Bruzek, M. J.; Hanifi, D. A.; Schulzetenberg, A.; Wu, Y.; Kim, C. H.; Zhang, Z.; Johns, J. E.; Salleo, A.; Fratini, S.; Troisi, A.; Douglas, C. J.; Frisbie, C. D. *Advanced Electronic Materials* **2017**, *3*, 1–7.

(30) Nematiaram, T.; Ciuchi, S.; Xie, X.; Fratini, S.; Troisi, A. *Journal of Physical Chemistry C* **2019**, *123*, 6989–6997.

(31) Dantanarayana, V.; Nematiaram, T.; Vong, D.; Anthony, J. E.; Troisi, A.; Nguyen Cong, K.; Goldman, N.; Faller, R.; Moulé, A. J. *Journal of Chemical Theory and Computation* **2020**, *16*, 3494–3503.

(32) Landi, A. *Journal of Physical Chemistry C* **2019**, *123*, 18804–18812.

(33) Nematiaram, T.; Troisi, A. *Journal of Chemical Physics* **2020**, *152*, 190902.

(34) Park, S. K.; Jackson, T. N.; Anthony, J. E.; Mourey, D. A. *Applied Physics Letters* **2007**, *91*, 6–9.

(35) Hailey, A. K.; Petty, A. J.; Washbourne, J.; Thorley, K. J.; Parkin, S. R.; Anthony, J. E.; Loo, Y. L. *Advanced Materials* **2017**, *29*, 1–8.

(36) Jurchescu, O. D.; Subramanian, S.; Kline, R. J.; Hudson, S. D.; Anthony, J. E.; Jackson, T. N.; Gundlach, D. J. *Chemistry of Materials* **2008**, *20*, 6733–6737.

(37) Beghi, M. G.; Bottani, C. E. *Philosophical Transactions of the Royal Society A: Mathematical, Physical and Engineering Sciences* **2004**, *362*, 2513–2535.

(38) Zhang, Y.; Manke, D. R.; Sharifzadeh, S.; Briseno, A. L.; Ramasubramaniam, A.; Koski, K. J. *Applied Physics Letters* **2017**, *110*, 071903.

(39) Kresse, G.; Furthmüller, J. *Computational Materials Science* **1996**, *6*, 15–50.

(40) Kresse, G.; Furthmüller, J. *Physical Review B* **1996**, *54*, 11169–11186.

(41) Joubert, D.; Kresse, G. *Physical Review B - Condensed Matter and Materials Physics* **1999**, *59*, 1758–1775.

(42) Klimeš, J.; Bowler, D. R.; Michaelides, A. *Journal of Physics Condensed Matter* **2010**, *22*, DOI: `10.1088/0953-8984/22/2/022201`.

(43) Klime, J.; Bowler, D. R.; Michaelides, A. *Physical Review B - Condensed Matter and Materials Physics* **2011**, *83*, 1–13.

(44) Dion, M.; Rydberg, H.; Schröder, E.; Langreth, D. C.; Lundqvist, B. I. *Physical Review Letters* **2004**, *92*, 22–25.

(45) Payne, M. M.; Parkin, S. R.; Anthony, J. E.; Kuo, C. C.; Jackson, T. N. *Journal of the American Chemical Society* **2005**, *127*, 4986–4987.

(46) Vyas, V. S.; Gutzler, R.; Nuss, J.; Kern, K.; Lotsch, B. V. *CrystEngComm* **2014**, *16*, 7389–7392.

(47) Izawa, T.; Miyazaki, E.; Takimiya, K. *Advanced materials.* **2008**, *20*.

(48) Jurchescu, O. D.; Meetsma, A.; Palstra, T. T. M. *Acta Crystallogr B.* **2006**, *62*, 330–334.

(49) Togo, A.; Tanaka, I. *Scripta Materialia* **2015**, *108*, 1–5.

(50) Ramirez-Cuesta, A. J. *Computer Physics Communications* **2004**, *157*, 226–238.

(51) Porezag, D.; Pederson, M. R. *Physical Review B - Condensed Matter and Materials Physics* **1996**, *54*, 7830–7836.

(52) Fonari, A.; Stauffer, S., *vasp_raman.py*; https://github.com/raman_sc/VASP/: 2013.

(53) Skelton, J. M.; Burton, L. A.; Jackson, A. J.; Oba, F.; Parker, S. C.; Walsh, A. *Physical Chemistry Chemical Physics* **2017**, *19*, 12452–12465.

(54) Fratini, S.; Mayou, D.; Ciuchi, S. **2016**, *26*, 2292–2315.

(55) *Physical Review Letters* **2006**, *96*, 1–4.

(56) Shuai, Z.; Li, W.; Ren, J.; Jiang, Y.; Geng, H. *Journal of Chemical Physics* **2020**, *153*, 080902-7–080902-11.

(57) Asher, M.; Angerer, D.; Korobko, R.; Diskin-Posner, Y.; Egger, D. A.; Yaffe, O. *Advanced Materials* **2020**, *32*, 1908028.

(58) Brillante, A.; Bilotti, I.; Della Valle, R. G.; Venuti, E.; Girlando, A. *CrystEngComm* **2008**, *10*, 937–946.

(59) Weinberg-Wolf, J. R.; McNeil, L. E.; Liu, S.; Kloc, C. *Journal of Physics Condensed Matter* **2007**, *19*, 276204.

(60) Sosorev, A. Y.; Maslennikov, D. R.; Kharlanov, O. G.; Chernyshov, I. Y.; Bruevich, V. V.; Paraschuk, D. Y. *Physica Status Solidi - Rapid Research Letters* **2019**, *13*, 1–23.

(61) Cavaye, H. *Angewandte Chemie - International Edition* **2019**, *58*, 9338–9346.

(62) Pintschovius, L.; Rietschel, H.; Sasaki, T.; Mori, H.; Tanaka, S.; Toyota, N.; Lang, M.; Steglich, F. *Europhysics Letters* **1997**, *37*, 627–632.

(63) Degli Esposti, A.; Moze, O.; Taliani, C.; Tomkinson, J. T.; Zamboni, R.; Zerbetto, F. *Journal of Chemical Physics* **1996**, *104*, 9704–9718.

(64) Hermet, P.; Bantignies, J. L.; Rahmani, A.; Sauvajol, J. L.; Johnson, M. R. *Journal of Physical Chemistry A* **2005**, *109*, 4202–4207.

(65) Bedoya-Martínez, N.; Schrode, B.; Jones, A. O.; Salzillo, T.; Ruzié, C.; Demitri, N.; Geerts, Y. H.; Venuti, E.; Della Valle, R. G.; Zojer, E.; Resel, R. *Journal of Physical Chemistry Letters* **2017**, *8*, 3690–3695.

(66) Hermet, P.; Lois-Sierra, S.; Bantignies, J. L.; Rols, S.; Sauvajol, J. L.; Serein-Spirau, F.; Lère-Porte, J. P.; Moreau, J. J. *Journal of Physical Chemistry B* **2009**, *113*, 4197–4202.

(67) Guilbert, A. A.; Parr, Z. S.; Kreouzis, T.; Woods, D. J.; Sprick, R. S.; Abrahams, I.; Nielsen, C. B.; Zbiri, M. *Physical Chemistry Chemical Physics* **2021**, *23*, 7462–7471.

(68) Kruglova, O.; Mulder, F. M.; Kotlewski, A.; Picken, S. J.; Parker, S.; Johnson, M. R.; Kearley, G. J. *Chemical Physics* **2006**, *330*, 360–364.

(69) Stoeckel, M.-A. et al. *Advanced Materials* **2021**, *33*, 2007870.

(70) Wang, Y.; Parkin, S. R.; Gierschner, J.; Watson, M. D. **2008**, *10 (15)*, 3307–3310.

(71) Eggeman, A. S.; Illig, S.; Troisi, A.; Sirringhaus, H.; Midgley, P. A. *Nature Materials* **2013**, *12*, 1045–1049.

(72) Thorley, K. J.; McCulloch, I. *Journal of Materials Chemistry C* **2018**, *6*, 12413–12421.

(73) Hallani, R. K.; Thorley, K. J.; Mei, Y.; Parkin, S. R.; Jurchescu, O. D.; Anthony, J. E. *Advanced Functional Materials* **2016**, *26*, 2341–2348.

(74) Harrelson, T. F.; Cheng, Y. Q.; Li, J.; Jacobs, I. E.; Ramirez-Cuesta, A. J.; Faller, R.; Moulé, A. J. *Macromolecules* **2017**, *50*, 2424–2435.

(75) Adhikari, J.; Zhan, P.; Calitree, B.; Zhang, W.; Fair, R.; Harrelson, T.; Faller, R.; Moule, A.; Milner, S.; Maranas, J.; Hickner, M.; Gomez, E., submitted 2021.

(76) Menard, E.; Podzorov, V.; Hur, S. H.; Gaur, A.; Gershenson, M. E.; Rogers, J. A. *Advanced Materials* **2004**, *16*, 2097–2101.

(77) Kamencek, T.; Zojer, E. *Journal of Materials Chemistry C* **2022**, *10*, 2532–2543.

(78) Tu, Z.; Yi, Y.; Coropceanu, V.; Brédas, J. L. *Journal of Physical Chemistry C* **2018**, *122*, 44–49.

(79) Nematiaram, T.; Padula, D.; Landi, A.; Troisi, A. *Advanced Functional Materials* **2020**, *30*, 1–10.

(80) Kobayashi, H.; Kobayashi, N.; Hosoi, S.; Koshitani, N.; Murakami, D.; Shirasawa, R.; Kudo, Y.; Hobara, D.; Tokita, Y.; Itabashi, M. *Journal of Chemical Physics* **2013**, *139*, 1132–1133.

(81) Geng, H.; Peng, Q.; Wang, L.; Li, H.; Liao, Y.; Ma, Z.; Shuai, Z. *Advanced Materials* **2012**, *24*, 3568–3572.

(82) Chang, J.-F.; Sakanoue, T.; Olivier, Y.; Uemura, T.; Dufourg-Madec, M.-B.; Yeates, S. G.; Cornil, J.; Takeya, J.; Troisi, A.; Sirringhaus, H. *Phys. Rev. Lett.* **2011**, *107*, 066601.

(83) Choi, H. H.; Cho, K.; Frisbie, C. D.; Sirringhaus, H.; Podzorov, V. *Nature Materials* **2017**, *17*, 2–7.

(84) Pelzer, K. M.; Vázquez-Mayagoitia, Á.; Ratcliff, L. E.; Tretiak, S.; Bair, R. A.; Gray, S. K.; Van Voorhis, T.; Larsen, R. E.; Darling, S. B. *Chemical Science* **2017**, *8*, 2597–2609.

(85) Landi, A.; Troisi, A. *Journal of Physical Chemistry C* **2018**, *122*, 18336–18345.

(86) Xie, X.; Santana-Bonilla, A.; Troisi, A. *Journal of Chemical Theory and Computation* **2018**, *14*, 3752–3762.

(87) Cheng, Y. Q.; Kolesnikov, A. I.; Ramirez-Cuesta, A. J. *Journal of Chemical Theory and Computation* **2020**, *16*, 7702–7708.

Chapter 3

Compact, and Portable Automatic Sample Changer Stick for Cryostats and Closed-Cycle Refrigerators

3.1 Acknowledgement

Luke Daemen is the beamline scientist on the neutron spectrometer. Eric Novak is the scientific associate on the neutron spectrometer. Mariano Ruiz-Rodriguez programmed the software for the motors and controls. Saad Elorfi is the sample environment master engineer. Amanda Morris and Benjamin Thomas synthesized the materials measured on the sample changer stick. Adam Moulé was the PI in charge of this project.

3.2 Introduction

The development of automatic sample changers in the laboratory or at user facilities originates from a variety of reasons. Fully automated sample changers requiring little to no human intervention or monitoring saves time, improves productivity, simplifies tedious, repetitive tasks, and minimizes human error. Manufacturers of traditional laboratory equipment such as gas chromatographs, thermogravimetric analyzers, x-ray diffractometers, or NMR instruments, to mention a few, have supplied instruments with sample changers created for their specific needs for several decades. With the increase of flux, first at light sources and more recently at neutron sources, leading to shorter measurement times, the use of sample changers has become a necessity. Sample changer environment design for user facility instruments presents a number of challenges. Each beam line is unique in terms of space, accessibility, and physical and chemical sample environment.

The relatively recent availability of moderately priced robotic arms with multiple-axes and user-friendly software has led to the development of multiple sample changing solutions adapted to individual beam line requirements. Macromolecular crystallography beam lines[1, 2] and some powder diffraction instruments[3–6] in general have adopted such flexible approaches. Others, in an approach reminiscent of the development of sample changers for laboratory-scale instrumentations developed ad hoc, large capacity sample changers based on one particular beam line configuration and environment.[7, 8] Both approaches requires the deployment of large pieces of equipment, which is acceptable if the equipment resides permanently at a beam line and runs continuously, but is impractical for more versatile beam lines requiring a sample changer only part of the time for a limited number of samples. A second disadvantage is that most robotic-arm sample changers for example operate only at room temperature. Automatic sample-changing at cryogenic temperature is complex and remains the province of bulkier, dedicated systems coupled in makeshift ways to an existing cryostat, closed-cycle refrigerator (CCR), or other commercial cooling device. Another disadvantage of larger, more complex sample changers is cost, which becomes difficult to justify for sporadic use. Finally, most dedicated sample changers require the use of one specific type of sample holder -a definite lack of versatility.

The need for a simple, low-capacity, inexpensive sample changer operating at cryogenic temperature motivated the development of a simple sample-changer stick at the VISION beam line at the Spallation Neutron Source (Oak Ridge National Laboratory). VISION is a beam line dedicated to neutron vibrational spectroscopy (inelastic scattering) with typical measurement times lasting from fifteen minutes per sample, per temperature for strong scatterers to several hours per temperature per sample for weaker scatterers. Most samples are measured at cryogenic temperatures. The beam line uses a CCR with individual samples mounted at the end of a sample stick (at room temperature) and inserted in the CCR (usually kept at 5K). Insertion of the room temperature stick into the CCR initially causes a large increase in temperature, typically to 100K. The measurement cannot start until the temperature stabilizes at 5K, which typically means that a waiting period of 45 minutes is needed for the temperature to readjust to 5K for each sample. Manual sample changes every 1-2 hours for every sample are frequently impractical at a facility operating 24 hours a day. For these reasons a sample changer that could reduce cooling times and enable multiple measurements with no manual changes will lead to increased productivity and more efficient use of the VISION instrument. The sample changer stick (SCS) described below is simple (2 axes), robust, allows for sample pre-cooling, and is readily adaptable to most cooling devices in use at user facilities and in laboratories by changing the flange that allows the stick to mate with a cryostat or CCR. The sample capacity is limited by the cryostat or CCR bore and in the case of the prototype described here amounts to four samples. Multiple sample holder types can be used. This SCS is inexpensive and multiple versions can be built to reduce (but not completely eliminate) the need for manual sample changes. The system proved particularly advantageous for overnight runs at the beam line.

This review will first outline the mechanical design of the SCS, detailing the carousel and lance subsystems. Next, the software that controls the motors for sample selection and positioning along with correcting feedback is described for our system. Finally, four samples are mounted and measured using the SCS in cryogenic conditions, showing the SCS operating as expected.

3.3 Mechanical Design

The sample changer consists of two main subsystems driven by stepper motors; a rotating carousel for sample selection, and a lance which lowers the sample the correct depth into the neutron beam. Most of these components are made out of 6061 aluminum, as aluminum is relatively light weight and strong, resulting in a sample stick that can be used by a single person without a crane. All parts of the sample changer are readily available from major suppliers, as seen in the bill of materials (BOM) in Tables B.1 and B.2 of the Supplementary Information (SI). While some of the components were custom machined

Figure 3.1. Picture of entire sample changer stick.

from raw materials, the machining is simple, requiring just a basic end mill, lathe, and laser cutter or computer numerical control (CNC). These equipment are common and are typically readily available at most research institutions. The only specialized fabrication process needed involves three welds with matching grade stainless steel for a total weld length of <20 cm.

The entire sample changer stick can be seen in Figure 3.1. The stick is designed around a Janis closed-cycle refrigerator (CCR) on the VISION neutron spectrometer at the Spallation Neutron Source at Oak Ridge National Laboratory. The CCR cools samples down to as low as 5K and has an inner diameter of ~85 mm and an inner depth of ~120 cm, with the center of the neutron beam located ~110 cm from the top. At the top of the stick, stepper motors with encoders and drivers/controllers are attached to a ferrofluidic rotary feedthrough. The rotary feedthroughs are mated with DN16CF conflat flanges, which are welded to an ISO100 flange. The ISO100 flange seals the CCR required to evacuate atmospheric gases before back-filling with helium exchange gas.

To support the components that select (carousel) and position (lance) the sample 110 cm into the neutron path, an aluminum support rib and linear support guides were installed. The support rib is a long 6061 aluminum bar that is affixed to the ISO100 flange through a stainless steel support bracket. The bracket has four tapped holes to bolt the support rib and is welded onto the ISO100 flange. The engineering drawings of the support guides can be seen in Figures B.1-B.3 of the SI. The support guides bolt onto the support rib, and include holes for Rulon J dry sleeve bearings, or hybrid stainless steel housing with silicon nitride ball bearings, which perform very well in cryogenic temperatures at the speeds used here (<300 RPM). The support guides also act as mounting points for baffles, Figures B.4 and B.5, which helps to restrict cryogenic helium to the lower end of the CCR and improve cooling.

3.3.1 Carousel

The carousel holds four samples and rotates a 1/4 turn to select which sample to measure, Figure 3.2. The carousel consists of an upper aluminum round, Figure 3.2a, that is bolted to a round female threaded stainless steel standoff, Figure 3.2b. The standoff is connected to the rotary shaft of one of the stepper motors with a shaft coupler, Figure 3.2c. While rotary shafts can be purchased custom with threaded ends, this particular design foregoes that elegance in exchange for a reduction in cost (>$100 savings). The engineering drawing for the upper aluminum round is shown in Figure B.6 of the SI. The upper aluminum round uses four aluminum shafts to attach the lower carousel round, Figure 3.2d and B.7. A groove is cut into the aluminum shafts and retaining rings are pressed in to secure the aluminum rounds into place.

The components for each sample seat on the carousel contains two stud spring anchors,

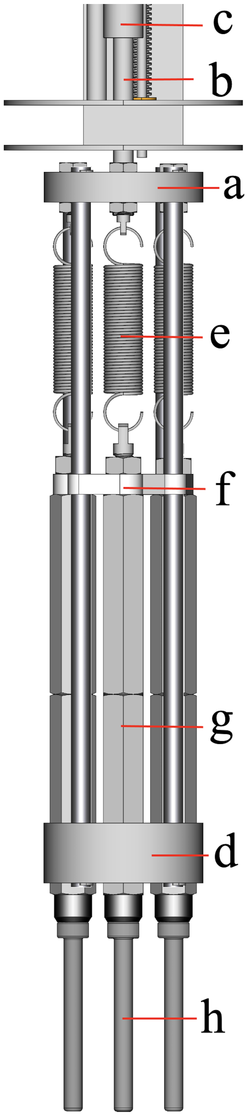

Figure 3.2. Carousel of the sample changer stick. a) upper aluminum round b) stainless steel round female threaded standoff c) shaft coupler d) lower aluminum round e) extension spring with hook ends f) PTFE linear guide g) female threaded hex bars h) vanadium sample can

an extension spring with hook ends (Figure 3.2e, a PTFE linear guide (Figure 3.2f), threaded aluminum hex bars (Figure 3.2g), and fasteners. The extension springs has a maximum extension of ∼22 cm and allows the sample (Figure 3.2h) to return to the retracted position, while the PTFE linear guides, engineering drawing shown in Figure B.8, are fastened to the hex bars and both limit motion to the vertical axis, and is a contact point for the lance, which will be discussed in more detail in Section 3.3.2. The lower carousel round has hex through holes with a sliding fit tolerance for the hex bars.

While two hex bars are connected with a threaded stud to increase the total length, a single hex bar can be tapped to achieve the same result. The hex bars are threaded on both ends to fasten the stud anchor on top, and a male threaded sample can on the bottom. This stick uses cylindrical vanadium sample cans that are sealed with a copper gasket and use a 5/16"-18 titanium threaded stud lid. The sample cans are available in 6 mm, 8 mm, and 10 mm outer diameters. Other sample can materials and geometries can be used with this stick as well.

The operation of the carousel is simple. With the lance in the retracted position, the stepper motor connected to the carousel is commanded to rotate by multiples of 90° to position the desired sample concentric with the CCR. A small hold current is applied by the motor to stop any movement away from the central position due to the CCR vibrations. This also aligns the proper access hole in the upper carousel round for the lance action.

3.3.2 Lance

The lance in the retracted and lowered positions can be seen in Figure 3.3. The neutron scattering detector banks on the VISION spectrometer are positioned to measure a 30 to 60° conical ring for forward and back scattered neutrons. The lance allows the sample to be lowered far enough from the other samples mounted on the carousel to avoid any scattered neutrons from interacting with the other samples. The lance uses a standard ACME lead screw and flange, Figure 3.3a. The lead screw is connected to a stepper motor through shaft couplers and a universal joint, as the lance's stepper motor is inserted at a 30° angle due to volume constraints. The flange has four equally angular spaced holes. A vertical shaft is held between the bottom two support guides, Figures 3.3b and 3.3c, and acts as a vertical linear guide and stops the flange from freely spinning. Another hole on the flange is used to mount the lance, Figure 3.3d, a stainless steel rod held between two shaft collars.

With the lance retracted, the carousel rotates to select the desired sample. The lance then traverses the access hole to strike the PTFE guide, Figure 3.3e, and lowers the sample into the neutron beam and is held in the lowered position until the measurement

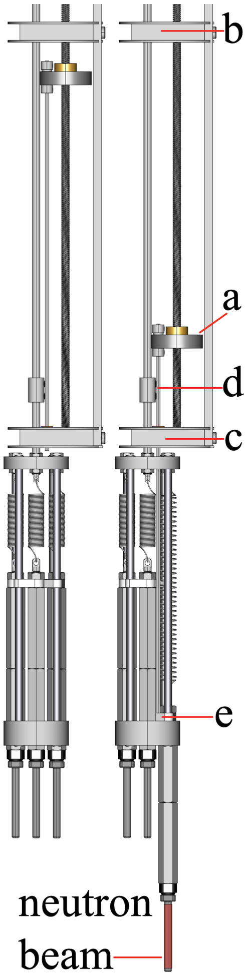

Figure 3.3. Lance action of the sample changer stick loaded with four 6 mm vanadium sample cans. Left shows the sample stick with lance at the top position with sample retracted. Right shows the lance extending the spring and placing the sample into the position of the neutron beam. a) ACME lead screw and flange b) and c) support guides d) lance e) PTFE guide

is complete. The neutron beam is usually adjusted using slits to match the area of sample within the sample can. The lance can easily adjust sample height to match the sample can fill height and beam slit parameters by reducing the steps sent to the stepper motor. Once the measurement is complete, retracting the lance also retracts the sample can with the extension spring and returns it to the carousel.

While the design presented has been commissioned for use on the VISION spectrometer, we recognize a few improvements to mechanical designs such as single piece hex rods for sample mounting, use of steel rather than aluminum for the sliding parts, and overall reduction of materials to decrease thermal loading and improve cool down times. Nevertheless, these are minor changes overall outside of function that will improve the operation and robustness of the SCS.

3.4 Software Controls

The software for the SCS was exclusively developed using EPICS, a commonly used software toolkit in various research facilities worldwide. The system is operated through multiple EPICS software tools, including ASYN Stream Device for network communication with the motor controllers, Databases for partial logic, archiving, and creation of Process Variables (PVs) across the network, and State Notation Language (SNL) as the central logic component. To display the graphical user interface, the Software Engineer employed Control System Studio (CSS). Additionally, the Scan Server serves as the scripting interface to synchronize the SCS with other beam line equipment.

3.4.1 ASYN

ASYN is used to create a low-level driver that enables computer network communication with motor controllers using the TCP/IP protocol, using a protocol file containing ASCII commands. This driver allows for sending network packets to the controllers to position a sample, as well as requesting information about the system's position and error status. In addition to network communication, the ASYN driver also sets initial gains for the motor controller, including velocity, holding and move currents, encoder ratio, and motor directions. These parameters are crucial for ensuring accurate and precise motor control.

3.4.2 Databases

The SCS EPICS Databases serve a crucial role in creating and managing PVs, as well as input and output records. PVs are particularly essential as they enable communication with graphical user interfaces through the Channel Access protocol. Moreover, PVs are periodically polled for archiving purposes, which enables the system to keep track of every state of the sample changer. In addition to these functions, PVs also facilitate remote control of the SCS through scripts via the Scan Server. Furthermore, the name of each PV is stored in the records, making them easily accessible by the SNL to sequence the movements of the system.

3.4.3 State Notation Language

The SNL is an indispensable tool for programming sequential operations within the SCS. It leverages state-transition diagram concepts to achieve this goal effectively. Within the SCS, the SNL plays a crucial role in controlling sample changes, by managing the main sequencing logic. It achieves this by interacting with the Database PVs, ensuring that the SCS samples change correctly and efficiently. Furthermore, the SNL logic ensures that the motors move precisely to their designated positions while avoiding potential collisions. In the event of any errors, the SNL also initiates the immediate cessation of motor operations to prevent any mishaps.

To place a sample, the script sends a command to the SCS software via the scan server, instructing it to move to the desired sample location. If a sample is already present, an error is reported upstream by the SCS. However, if the sample location is free, the SCS commands the carousel to rotate to the specified sample location and then inserts the lance until the sample is in place. An event is then triggered to notify the Scan Server that it can proceed with the next steps.

To retrieve a sample, the script sends a command to the SCS software to pick the sample currently on the beam. The SCS instructs the lance to retract and notifies the scan server via an event that the sample has been retrieved.

In the event that the actual position of the lance or carousel deviates from the commanded position outside the desired tolerance, the SCS software stops all movement, reports an error to the scan server, CSS GUI, and the human hall floor coordinators crew. Additionally, the carousel is protected from turning if the lance is still inserted, preventing collisions between the carousel and lance axis.

3.4.4 Scan Server

The Scan Server scripting tool is a solution that enables centralized control of all the equipment in the Beam Line, including the SCS. With this tool, researchers can easily monitor neutron metrics and control the other hardware to decide when data collection should begin. The Scan Server and SCS sample changer software work in tandem to optimize the performance and efficiency of beamline experiments. This collaborative system simplifies the experimental process and enhances the accuracy of the results obtained by researchers.

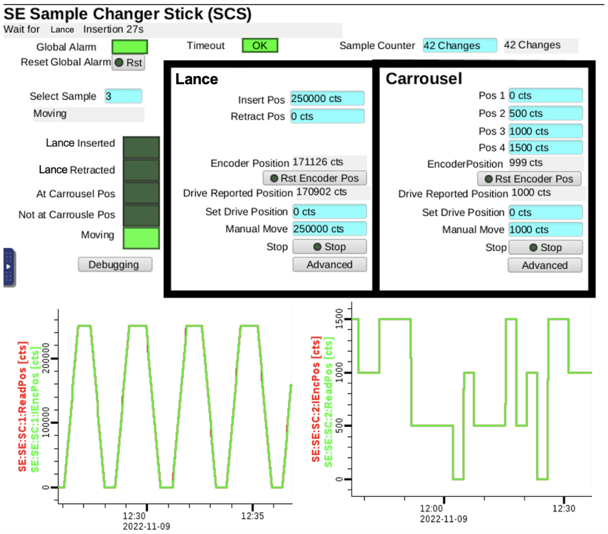

SE Sample Changer Stick (SCS)

Wait for Lance Insertion 27s

Timeout OK

Sample Counter 42 Changes 42 Changes

Select Sample 3

Moving

Lance

Insert Pos 250000 cts

Retract Pos 0 cts

Encoder Position 171126 cts

Drive Reported Position 170902 cts

Set Drive Position 0 cts

Manual Move 250000 cts

Carrousel

Pos 1 0 cts

Pos 2 500 cts

Pos 3 1000 cts

Pos 4 1500 cts

EncoderPosition 999 cts

Drive Reported Position 1000 cts

Set Drive Position 0 cts

Manual Move 1000 cts

Figure 3.4. Basic user screen used to monitor and use the SCS.

3.4.5 Control System Studio

The SCS Databases generate PVs enable users to read from and write to them using a graphical user interface. To create the GUI for all beamline software, CSS is utilized. The SCS comprises two GUIs: the Basic Screen (Figure 3.4), which includes simple practical controls and indicators for users, and the Advanced Screen (Figure 3.5), which includes low-level controls and indicators for configuring the SCS and monitoring low-level status for experts.

3.4.6 Network

To enable communication between the control Linux server and the SCS, two TCP/IP network ports are employed, with one dedicated to each Axis. To ensure that packets are delivered to the appropriate destination, a router is used to guide the traffic from the Linux server running the EPICS software to the SCS motor controllers on a distinct network. This arrangement keeps the SCS network isolated from the server network,

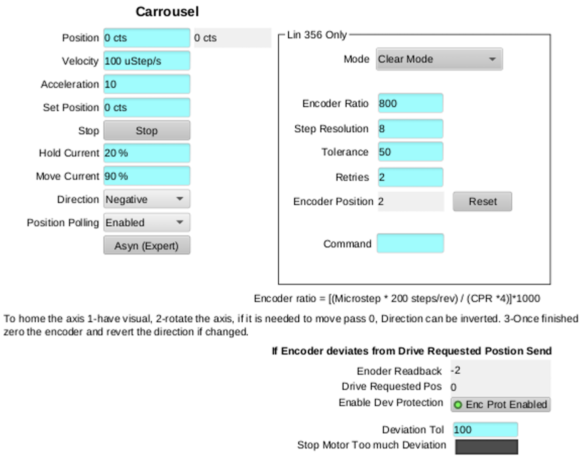

Carrousel

Position 0 cts 0 cts
Velocity 100 uStep/s
Acceleration 10
Set Position 0 cts
Stop
Hold Current 20 %
Move Current 90 %
Direction Negative
Position Polling Enabled

Lin 356 Only

Mode Clear Mode
Encoder Ratio 800
Step Resolution 8
Tolerance 50
Retries 2
Encoder Position 2
Command

Encoder ratio = [(Microstep * 200 steps/rev) / (CPR *4)]*1000

To home the axis 1-have visual, 2-rotate the axis, if it is needed to move pass 0, Direction can be inverted. 3-Once finished zero the encoder and revert the direction if changed.

If Encoder deviates from Drive Requested Postion Send

Enoder Readback -2
Drive Requested Pos 0
Enable Dev Protection ● Enc Prot Enabled
Deviation Tol 100
Stop Motor Too much Deviation

Figure 3.5. Advanced user screen for expert controls of SCS.

ensuring that the communication channel with the SCS remains secure and free from any unwanted server network traffic or access.

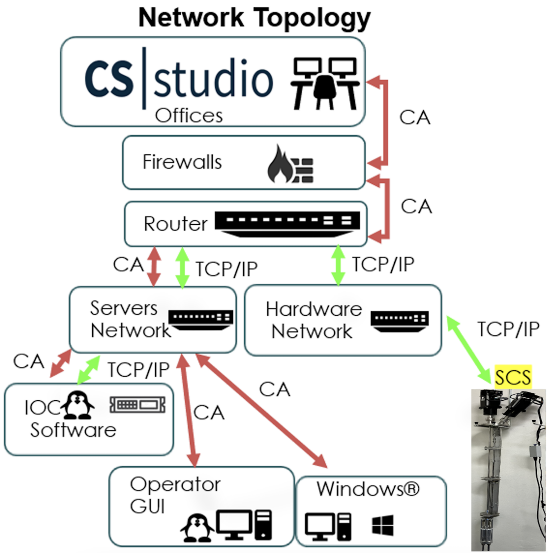

Figure 3.6. Flowchart showing communications network.

In addition, it is possible to monitor the SCS remotely from office networks by leveraging firewalls. To maintain the integrity and security of the system, outside access is restricted to read-only access for PVs from the beamline. This is accomplished using firewalls to enforce network segmentation, limiting external access to only those parts of the system that are necessary for monitoring purposes. These details are summarized in Figure 3.6.

3.4.7 SCS Control Hardware

The SCS control hardware comprises of several components working in unison to control and monitor its status. This includes two stepper motor controllers/drives, two stepper motors, two relative encoders, and two serial ports to network converter. Together, these components form a cohesive system that enables precise control and real-time monitoring of the SCS.

3.4.7.1 Stepper Motors and Relative Encoders

Both the lance and carousel mechanisms in this SCS utilize Lin 082321 2A Stepper Motors and relative encoders. One of the Lin Motors controls the lance mechanism, which is responsible for pushing the selected sample in or out of the beam. The relative encoder ensures that the steps sent to the motor reflect the exact amount of movement required to accurately push or retrieve the lance. The other Lin Motor oversees rotating the samples between positions 1 to 4 on the carousel. The relative encoder on this axis ensures that the steps sent to the motor accurately reflect the amount of rotation required to position the sample correctly.

The SCS stepper motors are controlled by a pair of motor controllers/drives Lin R356-RO. These motor controllers/drivers ensure that the precise voltage pulses are sent to the motors while simultaneously reading the encoder signals. Furthermore, the Lin controller/driver oversees reporting back statuses and executing EPICS commands.

Lastly, the SCS requires a reliable means of establishing computer communications with EPICS, and for this purpose, we employ the RS-485 to Ethernet converter Moxa 5150. This component receives TCP/IP ASCII commands over the EPICS hardware network and transforms them into differential RS-485 signals that the Lin Motor controller can readily comprehend.

3.5 Measurements

To test the SCS in-situ on the VISION instrument, four different metalated porphyrin metal-organic frameworks (MOFs), PCN-222, were loaded in 6 mm vanadium sample cans and mounted onto the SCS. The samples were cooled to 15 K before scattering data

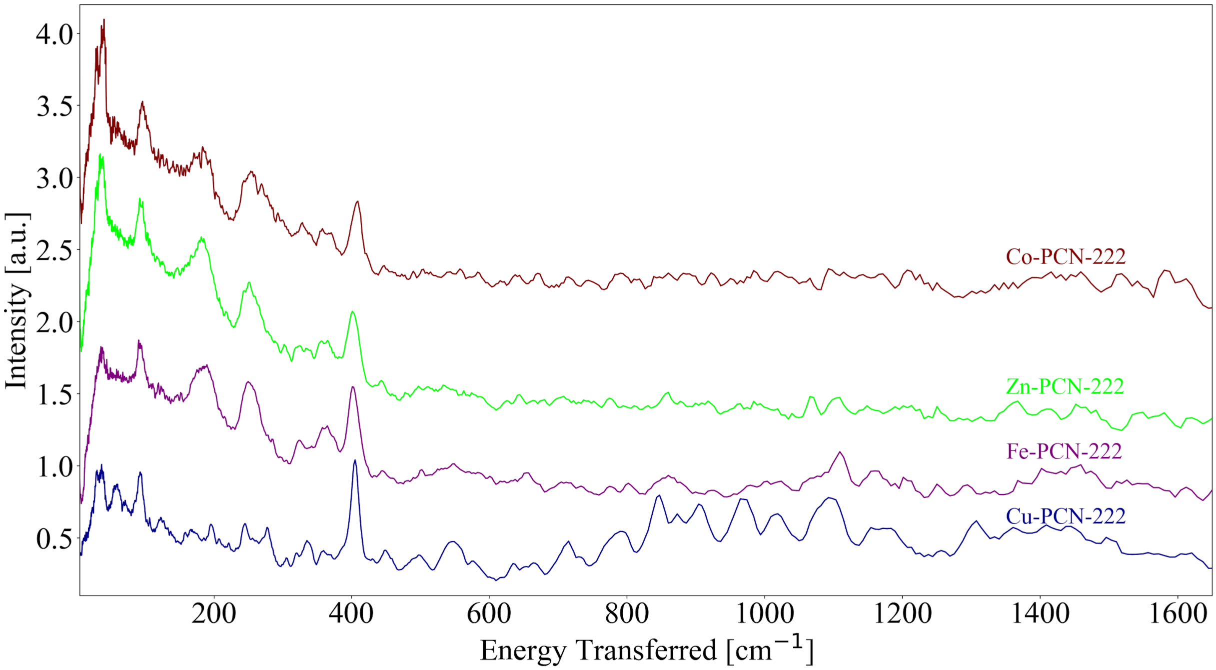

Figure 3.7. INS spectra of metalated porphyrin MOFs measured using the sample changer stick.

was measured. We show the INS spectra for each sample, Figure 3.7. The four MOFs, metalated with either Co, Zn, Fe, and Cu, show some of the same vibrational features, as expected, with some pronounced changes due to the dissimilar metalation, indicating the sample selection and repositioning in cryogenic conditions was successful.

3.6 Conclusion

Sample changers are used to increase productivity and decrease human intervention during scientific measurements. Here we present a SCS that uses a simple two-axis mechanism to select and position samples into the neutron beam. The design is low cost, portable to allow single user operation without the need of a crane, and can be easily built with basic fabrication equipment. While the SCS presented here is limited to a four seat carousel, CCRs with larger bore diameter could easily be engineered to accommodate 6 or 8 samples, further increasing productivity and efficiency of the neutron beam. The SCS reduces cooling frequency and total cooling time by enabling a single cooldown for four samples, and can be controlled remotely and set to run automatically. In all, this enables multiple measurements to increase overall efficiency and especially improves working conditions for happy beam line operators, especially during overnight measurements which encourage more periods at night to sleep.

BIBLIOGRAPHY

(1) Papp, G.; Felisaz, F.; Sorez, C.; Lopez-Marrero, M.; Janocha, R.; Manjasetty, B.; Gobbo, A.; Belrhali, H.; Bowler, M. W.; Cipriani, F. *Acta Crystallographica Section D: Structural Biology* **2017**, *73*, 841–851.

(2) Nurizzo, D.; Bowler, M.; Caserotto, H.; Dobias, F.; Giraud, T.; Surr, J.; Guichard, N.; Papp, G.; Guijarro, M.; Mueller-Dieckmann, C.; Flot, D.; McSweeney, S.; Cipriani, F.; Theveneau, P.; Leonard, G. *Acta Crystallographica Section D: Structural Biology* **2016**, *72*, 966–975.

(3) Rodriguez-Navarro, A. B.; Kudlacz, K.; Ortega-Huertas, M. *Journal of Applied Crystallography* **2012**, *45*, 135–137.

(4) Olsen, S. R.; Pullen, S. A.; Avdeev, M. *Journal of Applied Crystallography* **2010**, *43*, 377–379.

(5) Lian, D.; Swainson, I. P.; Cranswick, L. M.; Donaberger, R. *Journal of Applied Crystallography* **2009**, *42*, 1206–1208.

(6) Losko, A. S.; Vogel, S. C.; Reiche, H. M.; Nakotte, H. *Journal of Applied Crystallography* **2014**, *47*, 2109–2112.

(7) Hoshikawa, A.; Ishigaki, T.; Nagai, M.; Kobayashi, Y.; Sagehashi, H.; Kamiyama, T.; Yonemura, M.; Aizawa, K.; Sakuma, T.; Tomota, Y.; Arai, M.; Hayashi, M.; Ebata, K.; Takano, Y.; Kasao, T. *Nuclear Instruments and Methods in Physics Research, Section A: Accelerators, Spectrometers, Detectors and Associated Equipment* **2009**, *600*, 203–206.

(8) Shah, H. M. *Physica B* **1991**, *174*, 551–558.

Chapter 4

Photochemistry Sample Sticks for Inelastic Neutron Scattering

4.1 Acknowledgement

Luke Daemen is the beamline scientist on the neutron spectrometer. Eric Novak is the scientific associate on the neutron spectrometer. Adam Moulé was the PI in charge of this project.

4.2 Introduction

Vibrational spectroscopy was first used to measure the mid-infrared absorption of organic liquids to identify the molecules and their spectral fingerprints.[1] Now, vibrational spectroscopy is routinely used to characterize molecular structure and to understand the behavior of materials and their chemical processes through their vibrations.[2] Measuring vibrational motions has increased insight into studies of complex light-induced mechanisms in materials such as light activated catalysis,[3, 4] artificial photosynthesis,[5–9] water splitting,[10, 11] electron-phonon coupling,[12, 13] and other photo-chemical processes.[14] Although a broad range of important work has been realized using optical vibrational spectroscopy such as Raman and Fourier-transform infrared (FTIR), these measurements have limitations because optical selection rules result in a reduced density of "allowed" phonons that can be measured in the spectra. These selection rules originate because photons interact with the change in dipole moment within the molecule that is induced by a molecular motion, so molecular motions that do not cause a dipole change are invisible to a photon probe.

Inelastic neutron scattering (INS), by comparison, is an analytical vibrational spectroscopy technique that does not have optical selection rules. While photons excite dipolar transitions involving the electron cloud surrounding atoms, neutrons interact directly with the nuclear motion, which exclude neutron/nucleus interactions from optical selection rules. The direct interaction between neutrons and atomic nuclei enables accurate calculations for INS peak position, intensity, and shape, which allows a thorough investigation of local interactions on the atomic scale. Thus an INS spectrum can be interpreted as a nuclear cross section weighted density of motion states. By comparison, interpretation of the photon-electron interaction is much more complex. For the case of Raman spectroscopy, the spectrum must be interpreted via simulation of polarizability tensors that determine which peaks can be detected and their relative intensities. As an additional advantage of INS, since neutrons have mass, and therefore momentum, the momentum of the vibrational modes can also be measured, leading to richer and more complete data across the full Brillouin zone. By comparison, optical techniques provide only Γ-point information without multiple measurements of single crystal samples. A final important advantage of INS spectroscopy over optical spectroscopies is that INS measurements enable strongly different contrast for different isotopes. In particular the neutron scattering cross section for protons is particularly high, which enables INS to measure the vibrational modes that are most difficult to probe by optical techniques. Mixtures of protonated and deuterated molecules enable a large scattering contrast and maximize signal to noise for INS measurements. This comparison of measurement techniques is a strong justification for the use and expansion of INS spectroscopy to study complex materials.

Despite the aforementioned advantages of INS spectroscopy, there are almost no studies that highlight INS measurements of photoinduced or photoexcited samples. One of the main limitations is that neutrons penetrate deeply and probe into the bulk of materials, while photons only penetrate a few microns into the surface. This mismatch results in a low volume of photo-activated material on the sample surface that does not provide enough sample material to be probed by the comparatively low sensitivity (low flux) INS instruments. Even with very long data collection times to improve measurement statistics, the photo-activated signals in an INS instrument may be overshadowed by the larger volume of unexcited material in the sample. One method to reduce the amount of unreacted bulk sample, and therefore increase the signal from the photoreacted sample, is to use thin sample geometries. Unfortunately, decreasing the sample volume leads to longer measurement times and makes it more difficult to extract the sample signal from the instrument background. An additional measurement complication for INS is that almost all measurements must be performed at cryogenic temperatures in a closed cycle refrigerator (CCR) to reduce the spectral broadening and attenuation from the Debye-Waller effect. The need to measure at cryogenic temperatures requires the use of high vacuum and small and limited working volumes that can be accessed inside of the cryostat. To our knowledge, the only published paper of INS probing photochemistry at cryogenic temperatures has been performed recently on the TOSCA neutron spectrometer in the UK, wherein a 405 nm LED was used to illuminate a photochromic compound contained in quartz cuvettes[15]. The product of the cyclization reaction has reduced optical absorption at 405 nm compared to the reactant, allowing for deep optical penetration and thereby increased sample volume for the reacted mass. Nevertheless, long measurement times were necessary and future studies may be limited to materials sharing similar optical properties.

In this article we present the design of two different photochemistry sample sticks that are designed to enable efficient measurement of photoexcited samples using INS in spite of the challenges listed above. The sample sticks are designed based on the dimensions of the Janis CCR on the VISION neutron spectrometer at Oak Ridge National Laboratory (ORNL). These sample stick designs could also be adapted for use with other types of sample environment equipment and at other beamlines and facilities. The first sample stick is a passive system envisioned for film samples that uses high-power mounted light emitting diodes (LEDs) in the sample container to maximize illumination. The second stick is an active system designed for powder samples that implements a tumbler-based mixing system to optically expose the bulk material. This design improves upon the limitation of shallow light penetration depth encountered with the passive sample stick design. Both sample sticks are enclosed using either a stainless steel (passive) or aluminum (tumbler) housing, allowing the ex-situ atmospheric evacuation and back-filling of helium gas before undergoing cryogenic cooldown in the CCR. A simple optical system allows either a laser or LED light source to illuminate the sample in the passive sample stick, while the tumbler uses the laser source with a stepper motor and drive train system to mix the sample within the confines of the CCR.

In this paper, we first report in detail the designs for the passive and tumbler photochemistry sample sticks in different subsections for the different systems. The first subsection details the components to achieve high vacuum internally within both of the sample sticks. The next involves the light sources and optical components that translate the photons to the sample. We then describe the motor and components of the tumbler to achieve mixing within the neutron beam path. Lastly, we test and discuss results for the sample sticks in-situ with anthracene, a well-studied photoactive material which undergoes a photodimerization under illumination >300 nm, and a 405 nm 3d printer photoresin undergoing photo-polymerization.

4.3 Photochemistry Measurement Apparatuses

VISION is an indirect geometry neutron vibrational spectrometer at ORNL. VISION has the highest neutron flux and resolution of any other similar instruments, and has been designed to probe molecular vibrations over a broad range of energy from $\sim$5 cm^{-1} up to $\sim$8000 cm^{-1}. In order to reduce the Debye-Waller effect, a Janis CCR is used to cool the sample in the neutron beam path. Sample sticks for spectroscopy measurements on VISION are designed around the CCR. The CCR has an inner diameter of 8.58 cm, while the neutron beam center is located $\sim$110 cm from the top opening of the CCR. The maximum neutron beam area is 3 cm in width and 5 cm in height, with motorized slits which reduce the beam area for different sized sample containers. The components in the beam path of the neutrons are usually designed to be aluminum, a good material

Figure 4.1. A photograph of the two photochemistry sample sticks mounted vertically. On the left is the passive design sample stick and on the right is the tumbler design sample stick.

for neutron instrumentation as aluminum has a small neutron cross section (0.0082 barns for the incoherent scattering neutron cross section).

4.3.1 Passive Photochemistry Stick

4.3.1.1 Vacuum Components

Sample sticks on VISION typically have an ISO100 flange on the upper end, with a concentric long arm securing a sample container on the lower end that is placed into the neutron beam path. The top ISO100 flange closes off the CCR to allow cooling within the cryostat while removing atmospheric gases. The passive photochemistry sample stick, Figure 4.1 left, follows the typical sample stick design. Since there will be optical components directing light towards the sample, a Swagelok bellow valve and Swagelok tube connection allows the internal tube of the sample stick to be evacuated and subsequently backfilled with helium gas. Atmospheric gases must be removed to prevent the formation of ice because icing on any optical components would reduce that total power of light that reaches the sample. Backfilling the sample tube with helium, rather than use of a vacuum, is necessary to aid in heat convection for efficient cooling of the internal parts of the sample stick.

Figure 4.2 shows the components to seal the system and achieve both high vacuum seal between the CCR and atmosphere, and between the internals of the sample stick and atmosphere. At the top of the stick, a stainless steel DN16CF conflat half nipple and quick connect coupling are welded to the 304L stainless steel ISO100-K flange. The DN16CF flange mounts an electrical feedthrough, while the quick connect allows the vertical position of the stick to be adjusted to center the sample on the neutron beam. The upper components are sealed using either NPT threads and PTFE Teflon tape, or Swagelok tube fittings. An optical window is also epoxied into place at the top of the stick in anticipation of future use cases with a laser system. Lastly, a pressure gauge is installed to monitor the internal pressure.

The bottom of the stick contains the LED housing and sample container, which are attached to the photochemistry stick using Swagelok tube unions. All of the front and back ferrules in the two unions are stainless steel, with the exception of the front ferrule that attaches the sample container. The sample container union front ferrule was changed to PTFE Teflon to prevent swaging of the ferrules into the sample container cap, which makes the attachment reusable and easier to switch between samples. The LED housing was machined out of 6061 aluminum, with an engineering drawing shown in Figure C.1 of the Appendix. The housing is based on a double flanged pipe with end caps of half nipples machined to spec to fit the unions, using an indium wire seal between the mating

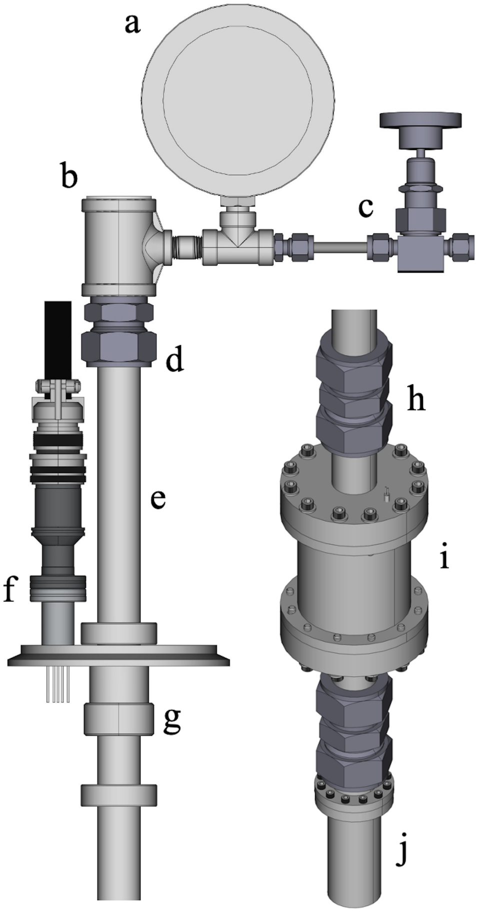

Figure 4.2. Components of passive photochemistry stick vacuum system. Upper assembly includes: a) Pressure gauge b) Fused silica optical window c) Swagelok bellow valve d) Swagelok tube fitting to male NPT adapter e) Stainless steel tube f) DN16CF half nipple conflat flange, and g) Quick connect coupling. Lower assembly includes: h) Swagelok union i) LED housing, and j) sample container

faces. The indium wire groove was machined using a ball end mill at the diameter of the indium wire (1 mm) and half the depth of the indium wire diameter into the double flanged faces. As the flanges are bolted together with an indium wire, the indium wire deforms into the groove and against the mating surface, creating a hermetic seal.

To bring power to the LED while maintaining the separate environments inside and outside of the sample stick, an electrical feedthrough was fabricated and installed into the half nipple of the upper LED housing half nipple cap. The feedthrough is a nonporous alumina ceramic tube with four bores. The bores are sized to accept 22 AWG copper wire and was epoxied into place using Torr seal epoxy. The ceramic tube was then epoxied into a hole made in the half nipple cap.

4.3.1.2 Optical Source and Components

The LED light source and optical components are directly above the sample, as shown in Figure 4.3. The LED used in this paper is Thorlabs M365D2 (365 nm, 2 W optical power) mounted in 30.5 mm aluminum heat sinks. An adjustable lens tube with an appropriate aspheric condenser lens is used to collimate the LED output towards the sample. Due to the low backfilling of helium, ∼200 mbar, which reduces convective cooling, the first LED tested burned out while driven at its maximum current rating, even in cryogenic temperatures. Therefore, to increase the heat sink capacity, a 6061 aluminum round, colored yellow in Figure 4.3, was machined to mount to the end of the heat sink and allow the LED assembly to mount against the LED housing. An indium wire was crushed between the aluminum round and the aluminum housing as a thermally conductive medium between the two. Testing of the optical source with a different mounted LED (Thorlabs M280D4, 280 nm, 114 mW optical power) required a different lens, resulting in different height aluminum rounds fabricated for each mounted LED as their respective condenser lenses have different focal lengths.

4.3.2 Tumbler Photochemistry Stick

4.3.2.1 Vacuum Components

The tumbler photochemistry sample stick, Figure 4.1 right, shows the entire sample stick with ISO100-K flange. A zoom in photograph of the upper components are shown in Figure 4.4. Like the passive design photochemistry stick, a Swagelok bellow valve is also used to evacuate and backfill the internal pottions of the tumbler photochemistry stick. Aluminum DN16CF conflat half nipples are welded at the top end to attach the respective feedthroughs with aluminum gaskets to maintain the high vacuum. The feedthroughs consist of a DN35CF conflat flange for the optical feedthrough, and a DN16CF flange for a rotary motion feedthrough.

The outer shell that houses the middle section of the tumbler sample stick is 6061 aluminum tubing that has been welded to an upper and lower flange, seen in Figure 4.5, with the engineering drawings shown in Appendix Figure C.2. Since the upper portion of

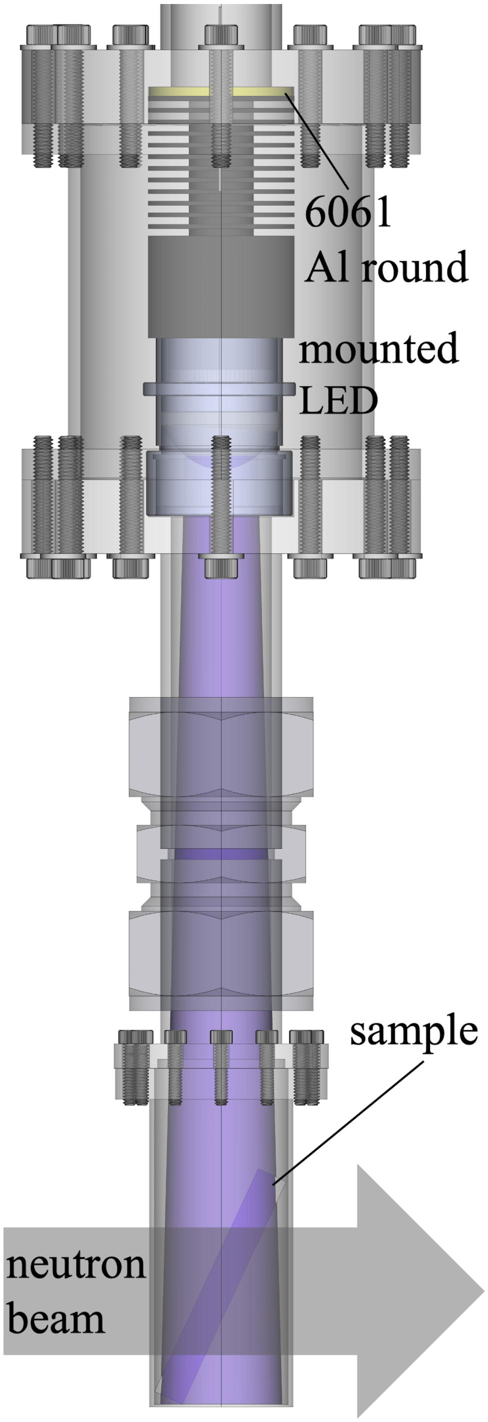

Figure 4.3. Internal view of optical system within the passive photochemistry stick. The sample is also depicted while being illuminated by the LED within the neutron beam path. Aluminum round sandwiched between LED housing and LED assembly to is colored yellow to increase distinction.

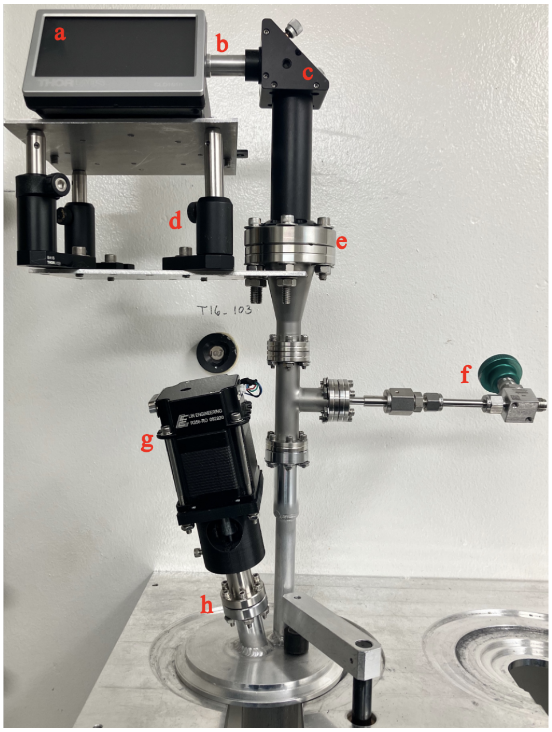

Figure 4.4. Labeled photograph of the upper portion of the tumbler photochemistry stick above the ISO100-K aluminum flange. a) Laser diode driver (Thorlabs CLD1010LP) b) Laser diode mounted in aluminum cylinder c) Kinematic right-angle mirror d) Laser diode driver base with optical post to align laser e) Optical viewport with laser window (Thorlabs VC22FL) f) Swagelok bellow valve g) stepper motor with mounted driver and controller, and h) ferrofluidic rotary feedthrough

the sample stick is near room temperature, the upper flange can use a standard rubber o-ring with standard design face-to-face vacuum groove without issue. The bolt circle of the upper flange is matched with the bolt circle on the ISO100-K flange, thus removable if any parts in the center require servicing.

At the lower end of the sample stick, a rubber o-ring cannot be used because the cryogenic temperatures would cause o-ring failure. The bottom cover is fabricated from an aluminum flange with an indium wire groove and welded to an aluminum tube and bottom round plate, allowing the hermetic seal, Figure 4.5. The bottom cover needs to be removed and reinstalled for every sample change. The conflat flanges in atmosphere and sealed flanges from the central section and below allow the complete sealing of the entire photochemistry sample stick.

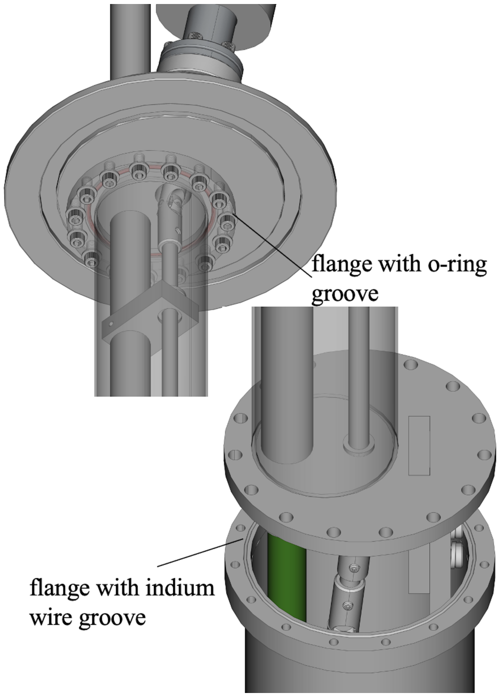

Figure 4.5. Upper and lower flanges that are welded to the 6061 aluminum tubing to house the internals of the tumbler photochemistry stick. The upper flange uses a rubber o-ring to seal, while the lower flange uses an indium seal. Both flanges have circular pockets with diameter matching the aluminum tubing outer diameter to ensure weld placement.

4.3.2.2 Optical Source and Components

Fiber optics are commonly used to transmit light into a cryostat. Eichhorn et al. used fiber optics for dynamic neutron polarization experiments within a liquid helium cryostat,[16] while a sample stick has also been designed and used to measure simultaneously Raman with INS on VISION[17] using fiber optics. We choose a different design because the fiber optic geometry would only illuminate only the top surface and fail to adequately photo-induce a sufficient volume of the sample for photochemistry experiments. Furthermore, the cryogenic temperatures for measurements on VISION (usually 5K) can lead to brittle fiber optic cables, resulting in core fractures from the CCR vibrations. While the brittle fibers can be laminated in an epoxy to avoid vibration induced fracture,[18] we opted to avoid using fiber optics within the cryogenic volume.

The laser system used can be seen at the top of the tumbler sample stick in Figure 4.4a. One benefit of having the optical system outside of the sample stick is that only optical power is pumped into the cryogenic environment, avoiding heating from other power sources. In the case of using a laser light source, the laser diode driver accepts standard To-Can laser diodes with and without fiber optic cables. With a fiber, the output can be collimated and connected through a cylindrical coupler to the kinematic right angle mirror mount, Figure 4.4c. In lieu of the fiber, the diode is mounted concentric to an aluminum cylinder and threaded to hold an aspheric lens, Figure 4.4b. The cylinder's outer diameter matches with the cylindrical coupler. The fiberless system enables switching of laser diode wavelengths without requiring a stockpile of different optical fibers, which can be easily damaged if care is not taken between sample changes. To ensure that the sample does not burn from the laser output, the aspheric lens that collimates the diode is adjusted from the focal point to increase the beam size to the maximum that fits within the right-angle mirror measured at the location of the sample.

From the laser diode driver, the incident light first reflects off a right-angled kinematic mirror, Figure 4.4c. The UV enhanced aluminum mirror in the kinematic mount provides >85% optical reflection for wavelengths between 250-600 nm. Since it is difficult to ensure perfect optical alignment down the length of the 6061 tube, the kinematic mount allows adjustment of ±4° in pitch and yaw. The laser then transmits across the vacuum viewport window. The viewport consist of a DN35CF conflat flange with a 25 mm diameter UV fused silica laser window sealed with Vitron gaskets. The fused silica window is rated for >90% optical transmission for wavelengths between 185 nm - 2100 nm, allowing deep ultraviolet wavelengths typically used in photochemistry studies and longer wavelengths that may be of interest for semiconductors. The light continues down the tube and exits, Figure 4.6, before being reflected by another right-angle mirror, and into the sample holder through a window on the sample can cap. While most chemical mechanisms and processes of interest in the materials are within the wavelength range of the optical components described here, the mirrors and windows can be easily changed to match the correct laser wavelength required.

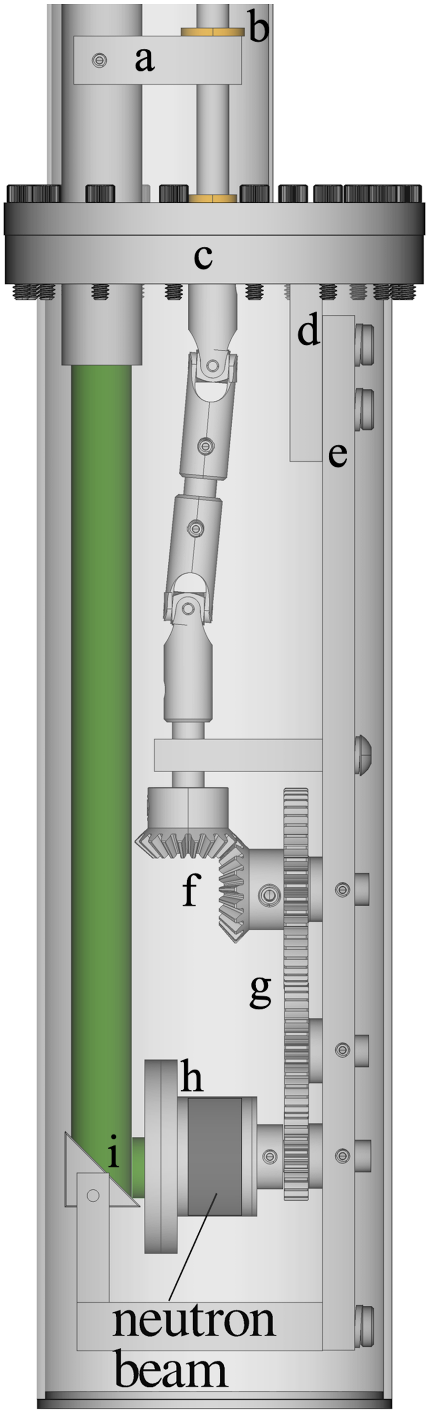

Figure 4.6. Inside view within lower cover of the optical and mechanical transmission components of photochemistry sample stick. a) linear guide b) Rulon J bearing c) lower flange d) support bracket e) support rib f) miter gears g) spur gears h) sample container i) laser beam

4.3.2.3 Mechanical Motion

In the tumbler sample stick design, a tumbler system is used to mix the powder sample while illuminating to maximize the sample volume that is illuminated by the laser. Figure 4.6 shows a schematic of the mechanical components of the tumbler along with the optical components described above. The optical and mechanical components at the bottom of the tumbler sample stick are connected to an aluminum support rib (Figure 4.6e), which is bolted onto a support bracket (Figure 4.6d) that has been welded to the bottom flange (Figure 4.6d), allowing a modular design in case different configurations are desired. The tumbler motion is driven by a stepper motor attached to a ferrofluidic rotary feedthrough, Figure 4.4g and Figure 4.4h, respectively. The drive shaft is aligned parallel to the 6061 aluminum tubing using a universal joint and guided along a series of linear supports (Figure 4.6a) and Rulon J sleeves (Figure 4.6b). Rulon J is used because it has very low outgassing under room temperature vacuum conditions and low friction at cryogenic temperature. A set of miter gears transform the rotary motion from the vertical axis to the horizontal axis.

The transfer of motion from the horizontal miter gear (Figure 4.6f) to the sample can (Figure 4.6h) is accomplished using a series of spur gears, Figure 4.6g. The shafts for the spur gears have grooves on the end in which to mount external retaining rings, and are themselves pressed into hybrid stainless steel and silicon nitride open ball bearings. These bearings have very low friction and are often used in cryogenic environments where coefficients of friction may become inhibitively large. The miter gear rotating on the horizontal axis shares a shaft with the top spur gear, allowing a transfer of rotary motion down spur gears of decreasing size. The smaller spur gears near the sample container reduces the amount of material in the path of the neutron beam that could increase non-sample scattering of neutrons, hence reducing the instrumental background. The bottom spur gear shares a shaft with a sample container that is held with a set screw.

To test the tumbling action and to plan for future powder samples, a sample can was machined from 6061 aluminum, with 1 mm thick walls, an inner diameter of 22 mm, and a height within the cylindrical portion of 17.8 mm. The flange has a groove machined to accept 1 mm indium wire, while the cap has been machined to fit a 25.4 mm window. The sample can and tumbler blade inserts are are shown in Figure C.3 of the Appendix. The dimensions of the sample container were designed around a 25.4 mm window, but larger containers and windows could be used in this configuration. While conventionally tumblers are used to mix powders at a high angular velocity, this design was intended to slowly drop material through the expanded beam, thoroughly illuminating the bulk of the powder sample. Therefore, the motor was set to rotate at a low speed of approximately ∼10 revolutions per minute (rpm), leading to the sample can rotating at ∼20 rpm due to the spur gear ratios. This low tumbling rate is appropriate for optically excited reactions occurring on the minutes times scale or for excitation of excited states (for example triplets in organic materials at cryogenic temperatures) that have lifetimes much longer than the tumbling rate.

4.3.3 Photodimerization in the Passive Sample Stick

Anthracene is a well-studied solid aromatic compound of three linearly fused benzene rings. Upon illumination with long wavelength UV photons (>300 nm), Anthracene undergoes a $[4\pi_s+4\pi_s]$ cycloaddition to form an anthracene dimer. The photodimerization reaction is reversible either by irradiation with shorter UV photon wavelengths (<300 nm[19]) or thermal treatment[20], returning the dimer back into the monomer. While the cycloaddition is photochemically allowed, it is forbidden thermally.[21] These properties of anthracene has brought about a slew of engineered materials such as shape memory alloys,[22, 23] mechanoluminescent and fracture detecting polymers,[24, 25] self-healing thermoplastic elastomers[26], photoresponsive hydrogels,[27, 28] and controlled-release drug delivery particles.[29–31] Anthracene and other photochemical materials can be studied using the INS photochemistry sticks.

To prepare the sample on the passive photochemistry sample stick, 120 mg of anthracene (used as purchased, Sigma-Aldrich) was sandwiched between two 50×18×3 mm quartz plates. The edges were sealed with Torr seal epoxy in a helium glove box. As mentioned previously, the goal of this sample geometry was to form a thin layer of sample in an effort to increase the relative volume fraction of illuminated/photoreacted sample com-

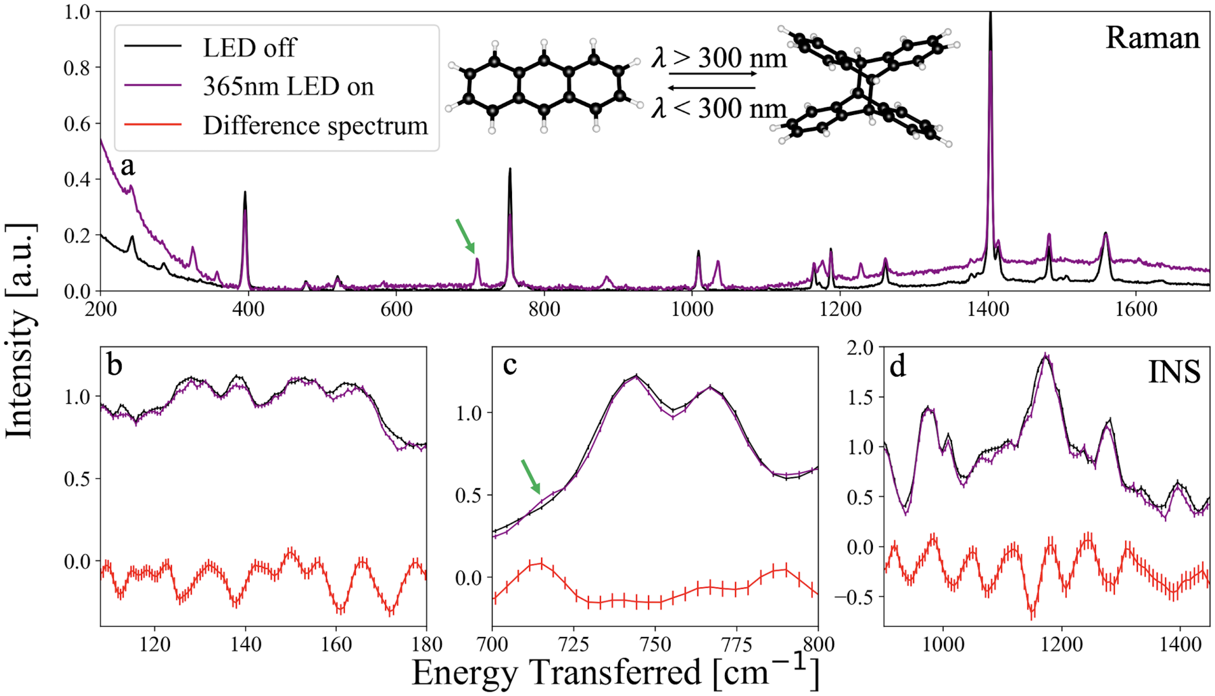

Figure 4.7. a) Raman spectroscopy of Anthracene before exposure (black) and after exposure (purple) to 365 nm LED illumination. b-d) show relevant portions of the INS spectra of Anthracene before and during illumination with 365 nm LED. Green arrows corresponds to mode formation from dimerization seen in both Raman and INS spectra. Difference spectra in red highlight changes between LED on and LED off. Difference spectra is scaled by 4 to increase clarity.

pared to the bulk of the sample, hence maximizing the signal from the in-situ dimerized anthracene. The quartz-anthracene sandwich was tilted into place in a 30 mm diameter aluminum sample can. With a half nipple cap fastened to the sample can, the sample can was secured to the Swagelok union, as seen in Figure 4.3. The internal portion of the sample stick was evacuated for ∼1 hour to 10^{-5} mbar before being placed into the CCR and cooled to 6 K. The CCR and the sample stick were back-filled with ∼300 mbar of helium. The beam slits for the incoming neutron beam were set to 18×10 mm to avoid scattering from the Torr seal epoxy. The INS measurement was taken without illumination for 4 hours followed by 3 additional hours of measurement with illumination using the 365 nm LED at 140 mW/cm^2. A temperature sensor was embedded into the CCR approximately at the sample location. The CCR used is able to dissipate up to 2 W of heat at 1 K and 10 W of heat at 40 K. With the LED powered using a constant current 1200 mA driver, the sensor measured an increase in temperature up to a steady state of ∼16 K. An empty quartz plate sealed with Torr seal was measured and used for background subtraction.

Ex-situ photodimerization of anthracene was measured using off-resonant Raman spectroscopy at room temperature on a Renishaw inVia Raman microscope with a wavelength of 785 nm. An initial measurement was taken before irradiation, and once again after irradiation for 12 hours with the 365 nm LED at 240 mW/cm^2. The Raman and INS measurements can be seen in Figure 4.7. The green arrow point to the corresponding Raman shift that occurs from the dimers and its INS equivalent. Although the INS changes look very minor, Figures 4.7b-d, we found that irradiating anthracene for 2 hours produced much less pronounced changes in the Raman spectrum, and an overnight irradiation was performed to get the features shown in Figure 4.7a. Therefore, we expect the INS intensities for those modes to increase with increased irradiation in-situ past 3 hours. In general there is less definition in the phonon peaks, which is due to the increasingly mixed crystals of monomers and dimers that have reduced long range order. The red spectrum is a numerical difference between the dark and illuminated spectra that highlights differences.

The quartz window sandwich method used here is only one possible sample loading method for the passive sample stick. Different designs may be used, depending on the application. For example, we have loaded samples between two concentric quartz tubes with a diffuse reflector, and also loaded porous Vycor tubes (both dataset are not included or presented in this article). Both of these examples were meant to increase the illuminated area, taking advantage of an easily modifiable sample environment.

4.3.4 Photopolymerization in the Tumbler Sample Stick

Stereolithography has rapidly grown in use over the past few decades, both commercially in production and rapid prototyping,[32–35] and even by home hobbyist and enthusiast. All stereographic printers follow the same basic principles, a vat filled of a photoactive resin and a stage are incrementally photo-polymerized to create a structure in layers from the bottom-up. The quick and easy fabrication afforded by 3d printing has contributed to the large push in additive manufacturing research,[36–39] and the photoactivate resins

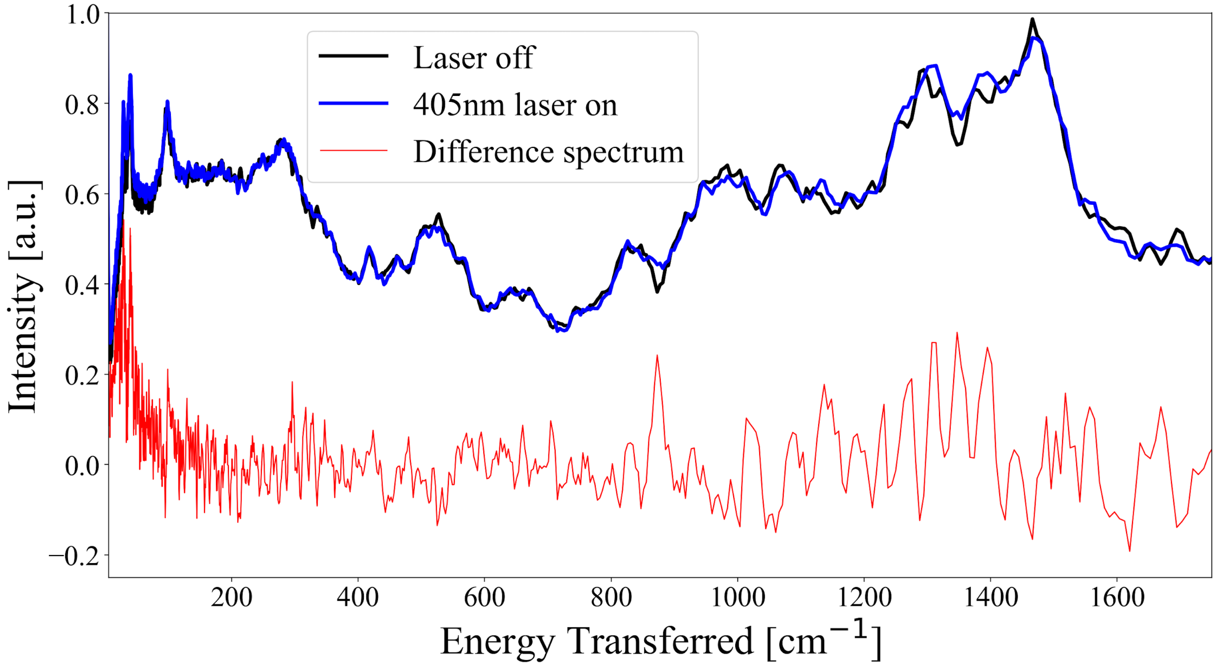

Figure 4.8. INS spectra showing the 405 nm photoresin with the laser off (black - uncured), and with 405 nm laser on (blue - cured). The red curve shows the numerical difference between the cured and uncured curves. Red curves have been scaled by 4 for clarity.

continue to be studied leading to a plethora of amalgamate resins with enhanced properties or novel functionalites.[40–45]

The tumbler photochemistry sample stick was used on the VISION spectrometer to measure the in-situ photo-polymerization of a 405 nm 3D printer photoresin (used as purchased, Anycubic). A quartz sample holder was fabricated out of an 18 mm outer diameter, 16 mm inner diameter, and 1.5 cm height quartz tube. The faces of the cylinder were a 1.5 mm thick quartz window and an 5 mm height aluminum round. The aluminum round was machined with a concentric pocket for mounting onto the tumbler stick with a threaded hole for a set screw, along with a concentric pad to match the inner diameter of the quartz tube. An image of the quartz sample holder described is shown in Figure C.4 of the Appendix. The quartz cylinder was epoxied to the aluminum round and cured overnight at room temperature. 300 mg of the photoresin was placed into the quartz holder in a helium glove box in low ambient light conditions, epoxy sealed with a quartz window, and allowed to cure overnight in dark conditions. During photo illumination measurements, a 405 nm laser diode (BDR-209) was driven at 400 mA to achieve an optical power of 127 mW/cm^2 at the sample location. The laser intensity was measured with a Thorlabs PM100D power meter and S121C photodiode. The laser path was adjusted to illuminate the sample mounting rod on the lowest spur gear, before the quartz sample holder with photoresin was mounted in low light conditions. With the bottom cover fastened, the internal volume of the tumbler stick was evacuated for $\sim$1.5 hours to 10^{-5} mbar and subsequently back-filled with 200 mbar of Helium. The stepper motor was set to rotate at 10 rpm before being lowered into the CCR and cooled to 15 K. The neutron beam slits were set to 11×15 mm to reduce undesired scattering from the tumbler components. With the laser on, the temperature sensor measured an increase of the steady state temperature by $<$300 mK.

Figure 4.8 shows INS spectra of the un-illuminated photoresin (black) and for the in-situ illuminated photoresin (blue). The un-illuminated resin was measured in the VISION spectrometer for three hours before the laser was turned on. Next the sample was exposed to the laser in-situ and INS spectra were averaged starting simultaneously with the laser exposure time, so initially the sample is unreacted and all of the changes that occur due to the optical excitation occur during the sample exposure. The blue spectrum in Figure 4.8 was collected over 9 hours. The photo-polymerization reaction shows obvious changes in the illuminated spectrum, with reduced intensity of vibrations for the unreacted photoresin and the appearance of new or growing features. The differences are highlighted in the difference spectra shown in red. Venzac *et al.* measured Raman scattering on a similar 405 nm photoresin, taking a raster scan and averaging over 3600 scans.[46] The authors highlight the decrease in scattering intensity once cured due to the reduction of methacrylate monomers by photo-polymerization. While the brand of photoresin measured here is not identical to the brand of clear photoresin used by Venzac, the Raman shifts clearly show the same changes in intensities at the same energies, indicating the likelihood of the same or similar chemical compositions. The obvious photoinduced changes to the INS spectrum with in-situ illumination shows that the tumbler system is working as intended.

4.4 Conclusions

Neutron sources are powerful tools used to study a wide variety of materials. While photochemistry is an important area of study with implications in new materials engineering and discovery, the photochemistry instrumentation at neutron sources has been limited. Here we present the design of two different photochemistry sample sticks that will enable in-situ photochemistry experiments. Two different designs are presented to enable measurement of film and powder sample geometries. To demonstrate the use of the film geometry sample sticks, we measured the light induced photodimerization of anthracene in-situ and detected changes to the INS scattering corresponding to previously measured changes using Raman scattering. To demonstrate the use of the powder sample geometry, we used a mechanical tumbler sample stick to measure the photopolymerization of a 3D printer photoresin in-situ. In both cases, changes were observed in the INS spectrum upon illumination that correspond to the same energies that changes were observed using Raman spectroscopy. Also in both cases, these polymerization reactions were carried out in-situ at cryogenic temperatures and within the neutron beam line, showing that chemical changes can be measured using the INS VISION instrument at ORNL. The photochemistry sticks broaden the capabilities of neutron instrumentation, allowing research into more materials such as artificial photosynthetics, non-linear optics, photoactive catalyst, photovoltaics, and more.

BIBLIOGRAPHY

(1) Abney, W.; Festing, E. *Phil. Trans. Roy. Soc.* **1881**, *172*, 887.

(2) Parker, S. F.; Lennon, D.; Albers, P. W. *Applied Spectroscopy* **2011**, *65*, 1325–1341.

(3) Cheshme Khavar, A. H.; Moussavi, G.; Mahjoub, A. R.; Satari, M. *Solar Energy* **2018**, *173*, 848–860.

(4) Zedler, L.; Mengele, A. K.; Ziems, K. M.; Zhang, Y.; Wächtler, M.; Gräfe, S.; Pascher, T.; Rau, S.; Kupfer, S.; Dietzek, B. *Angewandte Chemie - International Edition* **2019**, *58*, 13140–13148.

(5) Zedler, L.; Guthmuller, J.; Inês, R. d. M.; Kupfer, S.; Krieck, S.; Schmitt, M.; Popp, J.; Rau, S.; Dietzek, B. *Chemical Communications* **2014**, *50*, 5227–5229.

(6) Herrmann, C.; Neugebauer, J.; Presselt, M.; Uhlemann, U.; Schmitt, M.; Rau, S.; Popp, J.; Reiher, M. *Journal of Physical Chemistry B* **2007**, *111*, 6078–6087.

(7) Schwarz, J.; Ilic, A.; Kaufhold, S.; Ahokas, J.; Myllyperkiö, P.; Pettersson, M.; Wärnmark, K. *Sustainable Energy and Fuels* **2022**, *6*, 4388–4392.

(8) Kim, W.; Edri, E.; Frei, H. *Accounts of Chemical Research* **2016**, *49*, 1634–1645.

(9) Hong, Y. H.; Lee, Y. M.; Nam, W.; Fukuzumi, S. *ACS Catalysis* **2023**, *13*, 308–341.

(10) Qiu, Z.; Ma, Y.; Edvinsson, T. *Nano Energy* **2019**, *66*, 104118.

(11) Deng, Y.; Yeo, B. S. *ACS Catalysis* **2017**, *7*, 7873–7889.

(12) Harrelson, T. F. et al. *Materials Horizons* **2019**, *6*, 182–191.

(13) Vong, D.; Nematiaram, T.; Dettmann, M. A.; Murrey, T. L.; Cavalcante, L. S.; Gurses, S. M.; Radhakrishnan, D.; Daemen, L. L.; Anthony, J. E.; Koski, K. J.; Kronawitter, C. X.; Troisi, A.; Moulé, A. J. *Journal of Physical Chemistry Letters* **2022**, *13*, 5530–5537.

(14) Hoffman, N. *Chemical Reviews* **2008**, *108*, 1052–1103.

(15) Cavaye, H.; Schastny, M. *Physical Chemistry Chemical Physics* **2021**, *23*, 22324–22329.

(16) Eichhorn, T. R.; Haag, M.; Van Den Brandt, B.; Hautle, P.; Wenckebach, W. T.; Jannin, S.; Van Der Klink, J. J.; Comment, A. *Journal of Magnetic Resonance* **2013**, *234*, 58–66.

(17) Gillis, R. C.; Cheng, Y. Q.; Gallmeier, F. X.; Hartl, M. A.; Huegle, T.; Iverson, E. B. *Review of Scientific Instruments* **2018**, *89*, 1–8.

(18) Thomes, W. J.; Ott, M. N.; Chuska, R.; Switzer, R.; Onuma, E.; Blair, D.; Frese, E.; Matyseck, M. In *Planetary Defense and Space Environment Applications*, ed. by Hughes, G. B., SPIE: 2016; Vol. 9981, pp 134–149.

(19) O'Donnell, M. *Nature* **1968**, *218*, 460–461.

(20) Dong, S.; Ong, A.; Chi, C. *Journal of Photochemistry and Photobiology C: Photochemistry Reviews* **2019**, *38*, 27–46.

(21) Breton, G. W.; Vang, X. *Journal of Chemical Education* **1998**, *75*, 81–82.

(22) Xie, H.; He, M. J.; Deng, X. Y.; Du, L.; Fan, C. J.; Yang, K. K.; Wang, Y. Z. *ACS Applied Materials and Interfaces* **2016**, *8*, 9431–9439.

(23) Xie, H.; Cheng, C. Y.; Deng, X. Y.; Fan, C. J.; Du, L.; Yang, K. K.; Wang, Y. Z. *Macromolecules* **2017**, *50*, 5155–5164.

(24) Song, Y. K.; Lee, K. H.; Hong, W. S.; Cho, S. Y.; Yu, H. C.; Chung, C. M. *Journal of Materials Chemistry* **2012**, *22*, 1380–1386.

(25) Kan, L.; Cheng, H.; Li, B.; Zhang, X.; Wang, Q.; Wei, H.; Ma, N. *New Journal of Chemistry* **2019**, *43*, 2658–2664.

(26) Han, D.; Lu, H.; Li, W.; Li, Y.; Feng, S. *RSC Advances* **2017**, *7*, 56489–56495.

(27) Truong, V. X.; Li, F.; Forsythe, J. S. *ACS Macro Letters* **2017**, *6*, 657–662.

(28) Zheng, Y.; Micic, M.; Mello, S. V.; Mabrouki, M.; Andreopoulos, F. M.; Konka, V.; Pham, S. M.; Leblanc, R. M. *Macromolecules* **2002**, *35*, 5228–5234.

(29) Yao, H.; Wang, J.; Mi, S. *Polymers* **2018**, *10*, 1–27.

(30) Wang, C.; Delcros, J. G.; Biggerstaff, J.; Phanstiel IV, O. *Journal of Medicinal Chemistry* **2003**, *46*, 2672–2682.

(31) Palmer, A. J.; Ghani, R. A.; Kaur, N.; Phanstiel, O.; Wallace, H. M. *Biochemical Journal* **2009**, *424*, 431–438.

(32) Madhav, V. N. V.; Daule, R. *Journal of Dental and Allied Sciences* **2013**, *2*, 57.

(33) Quadri, S.; Kapoor, B.; Singh, G.; Tewari, R. *Journal of Oral Research and Review* **2017**, *9*, 96.

(34) Bertsch, A.; Bernhard, P.; Vogt, C.; Renaud, P. *Rapid Prototyping Journal* **2000**, *6*, 259–266.

(35) Zhou, J. G.; Herscovici, D.; Chen, C. C. *International Journal of Machine Tools and Manufacture* **2000**, *40*, 363–379.

(36) Zhakeyev, A.; Tobin, J.; Wang, H.; Vilela, F.; Xuan, J. *Energy Procedia* **2019**, *158*, Innovative Solutions for Energy Transitions, 5608–5614.

(37) Zhakeyev, A.; Zhang, L.; Xuan, J. In *3D and 4D Printing of Polymer Nanocomposite Materials*, Sadasivuni, K. K., Deshmukh, K., Almaadeed, M. A., Eds.; Elsevier: 2020, pp 387–425.

(38) Zhakeyev, A.; Jones, M. C.; Thomson, C. G.; Tobin, J. M.; Wang, H.; Vilela, F.; Xuan, J. *Additive Manufacturing* **2021**, *38*, 101828.

(39) Marsico, C.; Carpenter, I.; Kutsch, J.; Fehrenbacher, L.; Arola, D. *Dental Materials* **2022**, *38*, 2030–2040.

(40) Weng, Z.; Zhou, Y.; Lin, W.; Senthil, T.; Wu, L. *Composites Part A: Applied Science and Manufacturing* **2016**, *88*, 234–242.

(41) Wang, J.; Goyanes, A.; Gaisford, S.; Basit, A. W. *International Journal of Pharmaceutics* **2016**, *503*, 207–212.

(42) Skoog, S. A.; Goering, P. L.; Narayan, R. J. *Journal of Materials Science: Materials in Medicine* **2014**, *25*, 845–856.

(43) Voet, V. S.; Strating, T.; Schnelting, G. H.; Dijkstra, P.; Tietema, M.; Xu, J.; Woortman, A. J.; Loos, K.; Jager, J.; Folkersma, R. *ACS Omega* **2018**, *3*, 1403–1408.

(44) Xu, X.; Robles-Martinez, P.; Madla, C. M.; Joubert, F.; Goyanes, A.; Basit, A. W.; Gaisford, S. *Additive Manufacturing* **2020**, *33*, 101071.

(45) Thrasher, C. J.; Schwartz, J. J.; Boydston, A. J. *ACS Appl. Mater. Interfaces* **2017**, *9*, 39708–39716.

(46) Venzac, B.; Deng, S.; Mahmoud, Z.; Lenferink, A.; Costa, A.; Bray, F.; Otto, C.; Rolando, C.; Le Gac, S. *Analytical Chemistry* **2021**, *93*, PMID: 33961394, 7180–7187.

Chapter 5

Excited State Geometry Shifts Energy Levels for Favorable Singlet Fission in Tetracene

5.1 Acknowledgement

Luke Daemen is the beamline scientist on the neutron spectrometer. Eric Novak is the scientific associate on the neutron spectrometer. Adam Moulé was the PI in charge of this project.

5.2 Introduction

Photovoltaics (PV) convert sunshine into electricity, thus are a promising solution to the ever-growing energy demand of the world (we can not burn ancient dinosaur juice forever). The Shockley-Queisser limit[1] defines the maximum theoretical single junction device efficiency at 33%. Singlet fission (SF) is a spin allowed process that that converts a singlet exciton into a pair of triplet excitons between molecular chromophores. This carrier multiplication increases the maximum theoretical PV efficiency to 44%.[2, 3] Going from a single photon into a pair of excited charges spurred research into SF molecules and PV, as the ability to overcome the Shockley-Queisser limit is seductive. While SF is not fully understood, many studies have been dedicated to molecules that can undergo SF being incorporated into devices to increase efficiencies,[4–7] including photovoltaics,[8–16] photodetectors,[17] and organic light emitting diodes.[18–21] A simplified general mechanism for SF is:

$$S_0 + S_1 \rightleftharpoons (TT)^1 \rightleftharpoons T_1 + T_1$$

where S_0 and S_1 are the singlet ground and first excited states, respectively, $(TT)^1$ is the correlated triplet pair state, and T_1 is the first excited triplet state. SF is a unidirectional process when $E(2T_1) \leq E(S_1)$, and reversible when $E(2T_1) \geq E(S_1)$.[22] It is well-known and widely accepted that $E(S_1) \geq E(2T_1)$ or $E(S_1) \approx E(2T_1)$ for SF to occur. While the excited state energies are not in doubt, the source of energy to overcome the energy barrier in the cases of $E(S_1) < E(2T_1)$ remains inconclusive. Experimental and theoretical studies suggested the energy deficit can either be obtained through a thermally activated process,[23] with fission from higher lying singlet states (S_n),[24] compensated entropically,[25] or through the formation of multiexciton states.[26] However, these theories contradict the independence of SF to excitation energy[27, 28] and temperature[29].

Here, we use inelastic neutron scattering (INS) to probe the phonon density of states (pDOS) for photoexcited tetracene and pentacene. INS is analogous to Raman spectroscopy, with the advantage of no selection rules, measurement across the entire energy range alongside momentum transfer, and very high sensitivity to hydrogen-rich materials.[30] This makes neutron spectroscopy particularly advantageous over optical based technique for organic materials.[31] For the first time, we report in-situ excited state INS measurements on organic chromophores measured using a recently developed sample environment on the indirect geometry VISION neutron spectrometer at Oak Ridge National Laboratory.[32] The sample environment uses 405 nm (3.06 eV) and 520 nm (2.38 eV) lasers to photoexcite samples while measuring INS in-situ. We show the differences in the spectra with these excitation energies and model the spectra using plane-wave density functional theory (DFT), showing that the spectral changes are due to excitons. The excited state structures that are able to model the INS spectra correctly is taken from the periodic DFT calculation and used to calculate the electronic properties using Time-dependent DFT (TD-DFT), finding that the SF activation barrier reduces in the excimer state.

5.3 Methods

INS spectrometers can be one of two types, indirect and direct geometries. Indirect geometry spectrometers do not measure the phonon modes (or the currently active phonons), but the pDOS averaged over momemtum (Q), while the direct geometry spectrometers measure the currently active motions with a Q-dependence. INS is typically measured at cryogenic temperatures (5-20 K) to reduce signal attenuation and broadening from the Debye-Waller effect and inherent noise from thermally activated phonons. Consider a simplified example where the atoms at these cryogenic temperatures can be considered not moving. As the neutron scatters off the molecule, it loses some energy and activates an atomic vibration, e.g., a phonon mode. In an INS experiment, the scattered neutrons are detected and an energy histogram is determined based off of the energy transfer and direction (Q transfer) of the scattered neutrons, which yields the pDOS. We use a recently developed photochemistry sample environment stick[32] on VISION, an indirect geometry neutron spectrometer, which will be briefly summarized here. The sample stick uses stepper motors to rotate an aluminum sample container with a quartz glass window cap. The sample container has a 3-paddle aluminum insert, which helps to increase the density of illuminated sample. A laser driver directs a collimated beam through a series of mirrors into the sample container. The collimated beam was expanded by adjusting the collimating optic away from focus to the size of the mirrors. Optical power of 520 nm and 405 nm lasers were set to ∼200 mW at the sample location, as measured with Thorlabs PM100D power meter and S121C photodiode (∼113 mW/cm^2).

Approximately 200 mg of tetracene and pentacene crystalline powders were used as purchased from Sigma Aldrich and stored in a Helium glovebox. Both materials were loaded and sealed into the sample containers in the helium glovebox in low light conditions, then the quartz window was covered with foil until it was ready for measurement. The closed-cycle refrigerator (CCR) on the neutron spectrometer was cooled to 12 K and 3 hours of data was recorded for both samples with laser off. 6 hours of data was collected for both samples and both excitation energies, resulting in an increase of the steady state temperature of ≤300 mK measured with the CCR.

INS was modeled for the materials using the Vienna Ab initio Simulation Package (VASP),[33–35] using the projector-augmented-wave[36] potentials. Spin polarized calculation was performed and with triplet spin multiplet setting. The phonons were calculated using the supercell method implemented with phonopy.[37, 38] INS intensities are calculated using oCLIMAX[39] software, set to match the VISION instrument.

TD-DFT was performed using the ORCA package. Structures were relaxed using the B97M level of theory with the def2-TZVP basis set.[40, 41] The D3 dispersion correction was applied as approached by Grimme[42] *et al.* with Becke-Johnson damping.[43] Level of theories were chosen from the GMTKN55[44] benchmarking database and tested by comparing calculated and experimental singlet and triplet energy levels, as seen in Figure D.0.1. The self-consistent field convergence tolerance for energy change was set to 10^{-9} au.

5.4 Results and Discussion

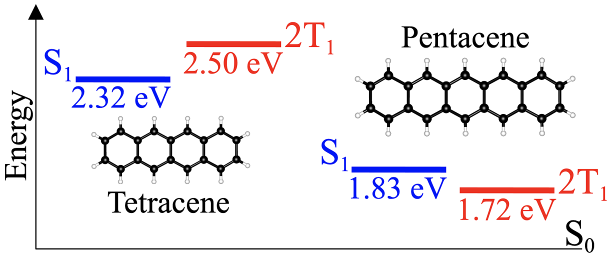

Figure 5.1. Electronic states diagram showing the ground state, first Singlet and 2× first Triplet energy levels for tetracene (left) and pentacene (right).

Tetracene and pentacene are model molecules used in studying the SF mechanism,[45] containing four and five linearly fused benzene rings, respectively. Figure 5.1 shows the energy levels of the first excited singlet (S_1) and 2× first excited triplet ($2T_1$), in blue and red, respectively, for tetracene and pentacene. E(S_1) is 1.83 eV and E($2T_1$) is 1.72 eV for pentacene,[46, 47] resulting in a spontaneous unidirectional exoergic pathway for SF on the 80-100 fs timescale.[48–51] On the other hand, tetracene has energy levels of 2.32 eV for E(S_1) and 2.50 eV for E($2T_1$),[52] leaving a 0.18 eV energy barrier for SF to proceed. Despite tetracene's endoergic character, SF proceeds with very high quantum efficiency for both pentacene and tetracene.[53]

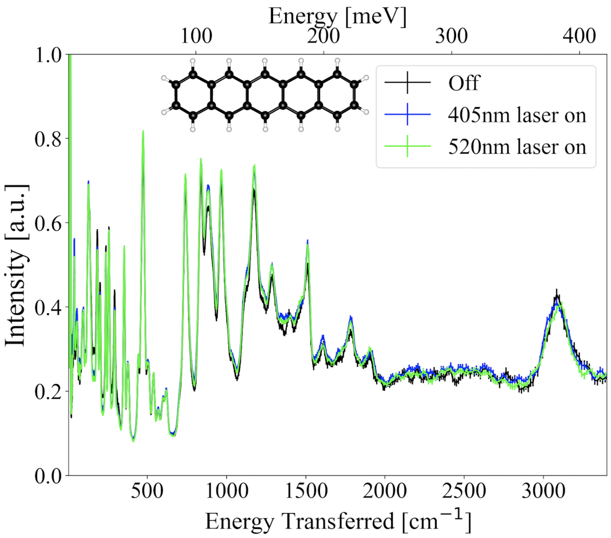

Figure 5.2. INS spectrum for pentacene with 405 nm laser on (blue), 520 nm laser on (green), and laser off (black).

Figure 5.2 shows the INS spectrum for crystalline pentacene with the lasers off and on. The blue line shows the measurement with 405 nm laser on, green line shows 520 nm laser on, and black is for laser off. The S_n population has been shown to have a dependence on excitation energy by measuring stimulated emission in ultrafast measurements, finding that the excitation energies between 475-575 nm forms singlets,[54] and is corroborated by photoluminescence studies.[55, 56] While pumping with 405 nm excitation energy was not performed, blue shifted pump sources (475nm, 2.61 eV) shown a population of 'hot' exciton states before relaxing to a short-lived S_1.[45] Temperature dependent transient absorption measurements indicate SF is active down to 4 K.[57] INS measures the superposition of the pDOS of the sample, therefore a mixture of ground state and excited state molecules are present in the spectra. Very minor changes are seen between the laser off compared to laser on measurements. The minor changes throughout the spectra are likely the result of slight changes in bond lengths after excitation and from excimers, locally distorted geometries of excited dimers.[49, 58] The acenes studied can also undergo [2+2] photodimerization[59] between neighboring molecules, but we have previously shown this solid-state reaction to be very slow in the cryogenic environment.[32] The INS spectral differences between the 405 nm and 520 nm lasers are more or less absent within the experimental error, indicating the lack of changes to the pDOS from the optically excited states.

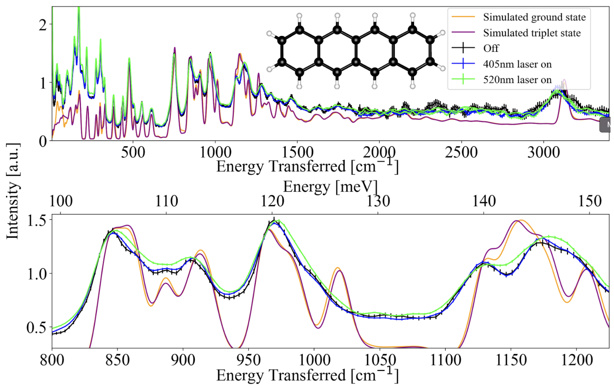

Figure 5.3. INS spectrum for tetracene with 405 nm laser on (blue), 520 nm laser on (green), and laser off (black). Top shows INS of the entire energy range. Bottom shows a close up of the spectra between ∼100-150 meV.

The same measurement was performed for crystalline tetracene and can be seen in Figure 5.3, using the same color scheme as for pentacene in Figure 5.2. SF has been shown to occur for tetracene with various optical excitation energies and temperatures (2.43 eV, 2.58 eV, and 3.10 eV at 298 K, 77 K, and 4 K).[28, 45] The temperature independence was further supported by transient absorption measurements between 10-270 K in tetracene.[29] Like pentacene, tetracene shows similar changes to the spectra when comparing laser off and on. Interestingly, the spectra of the 405 nm and 520 nm lasers on during INS measurement overlap within error throughout the spectral range, besides from the peaks shown in the bottom of Figure 5.3 between the energy range ∼100-150 meV. This is also the energy range where most of the changes between the dark and light on spectra occurs. The 520 nm excitation produces an increase in phonons with energies between ∼100-150 meV, while the 405 nm excitation is less pronounced. The change in phonons between the excitation wavelengths are likely the result of increased density of long lived T_1 states, as tetracene has a much higher absorption at 520 nm compared to 405 nm.[60]

Previous 2D electron spectroscopy measurements show evidence of coherent vibrational modes coupling to overcome the energy deficit and is dependent on excitation wavelength.[61] The 405 nm laser is able to excite higher S_n states and fission to the triplet pairs without the need for any vibronic coherence. This is further corroborated by shaped pulse studies that show that the energy deficit for SF can be supplied optically.[62]

While the excitation energy of the 405 nm laser is able to excite S_n above $2\mathrm{T}_1$ and directly convert through SF, the 520 nm laser is only able to excite S_n states with the broad energy range supplied by the laser below $2\mathrm{T}_1$. Indeed, Stern *et. al* found that SF proceeds for a tetracene derivative by vibronic coupling to form $(\mathrm{TT})^1$, with $\mathrm{T}_1 + \mathrm{T}_1$ separation being thermally activated,[63] but the whereabouts of the energy deficit required and obtained in cryogenic measurements remain.

To explore the SF energy barrier of tetracene, TD-DFT is used to calculate the excited states of tetracene. For a single gaseous tetracene molecule in the ground state, S_1 and $2\mathrm{T}_1$ levels are calculated to be 2.286 eV and 2.418 eV, respectively, very close to the published experimentally measured values of 2.32 eV and 2.5 eV. Opposed to being rigidly bound by covalent bonds as with inorganic semiconductors, molecular crystals are held together by weak Van der Waals forces, which may allow appreciable structural changes from the dipole during the electronic excitation. The deformation from the ground state structure and neighboring molecules can shift the electronic states. The geometry for tetracene was then optimized in the S_1 excited state. The excited state energy levels were calculated with the S_1 excited geometry, finding that the S_1 level decreased to 1.974 eV, while $2\mathrm{T}_1$ level decreased to 1.592 eV. This shows an avenue for SF that does not require additional energetic activation, but also paints an incomplete picture, as the single molecule calculation ignores the local environment of true periodic systems, and importantly, the effect to the electronic states from the neighboring, ground state, molecules.

The S_1 and $2\mathrm{T}_1$ levels are further explored by using planewave DFT to include periodic effects. We have previously shown excellent agreement between experimental and simulated INS, allowing experimental vaidation of the input structure and calculated phonons leading to accurately calculated charge mobilities.[64, 65] The orange and purple spectra seen in Figure 5.3 show the simulated INS for ground and triplet states, respectively. Some of the changes from photoexcitation are captured in the triplet INS simulation. First at ~113 meV, both the slight increased intensity and broadening from ground to triplet is seen in the 520nm laser on (green) spectrum. Then at 110 meV the triplet structure shows decreased intensity resulting in the smoothe valley from the distinct peak seen in the light off spectrum. The phonon at ~121 meV shows a very slight broadening in higher energy that is not as large as seen in the measured spectrum. Lastly, the simulations show the increased intensity that fills the valley at 142 meV and also has increased intensity on the right at about 148 meV, clearly capturing the effect of including the triplet. In all, this shows that the periodic calculation is able to capture some of the phonon changes seen from the triplet induced deformations, which can then be used in the TD-DFT calculation.

The unit cell of the tetracene crystal used in the periodic calculations contain two molecules.[66] Local basis set TD-DFT is again used to calculate E(S_1) and E($2T_1$) of the ground state molecules optimized with planewave DFT, 2.241 eV and 2.306 eV for one molecule, and 2.232 eV and 2.286 eV for the other, respectively. While the result is good, but less quantitative than the local basis set optimized geometry, the calculation still shows the endoergic SF character. DFT may not always be quantitative, but it does show trends well, in this case the shifting of electronic levels from excited state deformations. The excited state optimized structure used to model INS is then taken from the planewave DFT and used to calculate E(S_1) and E($2T_1$), 1.951 eV and 1.496 eV for one molecule, and 2.212 eV and 2.232 eV for the other, respectively. While the electronic excitation is very fast, the nuclei moves relatively slower towards its new relaxed state. That deformation causes the excimer formation with neighboring molecules, and the TD-DFT calculation shows that it can have a large impact on the electronic structure. While both levels shift downwards, T_1 decreases much lower than S_1 in one molecule, indicating that favorable energetic levels for SF to proceed exoergically without the need for additional activation energy may be due to the structural deformations caused by the dipole formation of the excited states. The exciton on the molecule calculates E(S_1) and E($2T_1$) very close to the calculated values of the local basis set optimized in the S_1 state, indicating that the energetics due to localization of an exciton and its resulting deformations are captured by the periodic calculation. The neighboring molecule has most of the energy shifting lower for T_1, resulting in E(S_1)~E($2T_1$). While this shows that the local electronic states can shifts accordingly to allow SF without an energy barrier once the optical excitation takes place, it is unclear what occurs immediately proceeding the shifting. It may be that while S_1 maintains the initial ground state $E(S_1)$ and $E(2T_1)$ recedes toward its lower equilibrium energy, at some point during the excited state relaxation $E(S_1)$ is just below $E(2T_1)$, and SF could be thermally activated, or the nuclei continue to relax until $E(S_1) \geq E(2T_1)$ resulting in SF to form the $(TT)^1$. In this scenario, the local electronic states would allow both the thermal separation of $(TT)^1$, and the singlet regeneration from geminate triplets following SF from degenerate singlet and triplet pairs both previously observed in tetracene.[29, 63]

5.5 Conclusions

We used INS with a recently developed optical excitation sample environment to study the excited states of tetracene and pentacene. One limitation to the laser equipped sample environment on the neutron spectrometer is that currently there is only optical pumping. Lacking an integrated transient absorption set up, the excited state populations are only presumed based on previous experimental literature. With this in mind, we presume that for both excitation energies used, both the model molecules studied here undergoes some SF under illumination. The INS spectra is modeled, showing the effect of the triplets on the pDOS and verifying the validity of the periodic exciton structure. The structure is used in TD-DFT to calculate the electronic states, finding that the deformations from the excited state and neighboring molecules result in local electronic shifting, allowing $E(2T_1)$ to lower until the SF barrier reduces to be more easily overcome. This study will further the understanding of SF and spreads a recently developed instrument to study excited state materials.

Bibliography

(1) Shockley, W.; Queisser, H. *Journal of Applied Physics* **1961**, *32*, 510–519.

(2) Hanna, M. C.; Nozik, A. J. *Journal of Applied Physics* **2006**, *100*, DOI: `10.1063/1.2356795`.

(3) Dexter, D. L. *Journal of Luminescence* **1979**, *18-19*, 779–784.

(4) Baldacchino, A. J.; Collins, M. I.; Nielsen, M. P.; Schmidt, T. W.; McCamey, D. R.; Tayebjee, M. J. Y. *Chemical Physics Reviews* **2022**, *3*, 021304.

(5) Rao, A.; Friend, R. H. *Nature Reviews Materials* **2017**, *2*, 1–12.

(6) Hudson, R. J.; Stuart, A. N.; Huang, D. M.; Kee, T. W. *Journal of Physical Chemistry C* **2022**, *126*, 5369–5377.

(7) Futscher, M. H.; Rao, A.; Ehrler, B. *ACS Energy Letters* **2018**, *3*, 2587–2592.

(8) Ehrler, B.; Walker, B. J.; Böhm, M. L.; Wilson, M. W.; Vaynzof, Y.; Friend, R. H.; Greenham, N. C. *Nature Communications* **2012**, *3*, DOI: `10.1038/ncomms2012`.

(9) Lee, J.; Jadhav, P.; Reusswig, P. D.; Yost, S. R.; Thompson, N. J.; Congreve, D. N.; Hontz, E.; Van Voorhis, T.; Baldo, M. A. *Accounts of Chemical Research* **2013**, *46*, 1300–1311.

(10) Yang, L.; Tabachnyk, M.; Bayliss, S. L.; Böhm, M. L.; Broch, K.; Greenham, N. C.; Friend, R. H.; Ehrler, B. *Nano Letters* **2015**, *15*, 354–358.

(11) Xia, J.; Sanders, S. N.; Cheng, W.; Low, J. Z.; Liu, J.; Campos, L. M.; Sun, T. *Advanced Materials* **2017**, *29*, DOI: `10.1002/adma.201601652`.

(12) Kawata, S.; Pu, Y. J.; Saito, A.; Kurashige, Y.; Beppu, T.; Katagiri, H.; Hada, M.; Kido, J. *Advanced Materials* **2016**, *28*, 1585–1590.

(13) Kunzmann, A.; Gruber, M.; Casillas, R.; Zirzlmeier, J.; Stanzel, M.; Peukert, W.; Tykwinski, R. R.; Guldi, D. M. *Angewandte Chemie - International Edition* **2018**, *57*, 10742–10747.

(14) Reusswig, P. D.; Congreve, D. N.; Thompson, N. J.; Baldo, M. A. *Applied Physics Letters* **2012**, *101*, DOI: `10.1063/1.4752445`.

(15) Macqueen, R. W.; Liebhaber, M.; Niederhausen, J.; Mews, M.; Gersmann, C.; Jäckle, S.; Jäger, K.; Tayebjee, M. J.; Schmidt, T. W.; Rech, B.; Lips, K. *Materials Horizons* **2018**, *5*, 1065–1075.

(16) Wu, T. C.; Thompson, N. J.; Congreve, D. N.; Hontz, E.; Yost, S. R.; Van Voorhis, T.; Baldo, M. A. *Applied Physics Letters* **2014**, *104*, DOI: `10.1063/1.4876600`.

(17) Lee, J.; Jadhav, P.; Baldo, M. A. *Applied Physics Letters* **2009**, *95*, 10–13.

(18) Bai, J. W.; Chen, P.; Lei, Y. L.; Zhang, Y.; Zhang, Q. M.; Xiong, Z. H.; Li, F. *Organic Electronics* **2014**, *15*, 169–174.

(19) Ullah, M.; Yambem, S. D.; Moore, E. G.; Namdas, E. B.; Pandey, A. K. *Advanced Electronic Materials* **2015**, *1*, DOI: `10.1002/aelm.201500229`.

(20) Tang, X.; Hu, Y.; Jia, W.; Pan, R.; Deng, J.; Deng, J.; He, Z.; Xiong, Z. *ACS Applied Materials and Interfaces* **2018**, *10*, 1948–1956.

(21) Nagata, R.; Nakanotani, H.; Potscavage, W. J.; Adachi, C. *Advanced Materials* **2018**, *30*, DOI: `10.1002/adma.201801484`.

(22) Miyata, K.; Conrad-Burton, F. S.; Geyer, F. L.; Zhu, X. Y. *Chemical Reviews* **2019**, *119*, 4261–4292.

(23) Thorsmølle, V. K.; Averitt, R. D.; Demsar, J.; Smith, D. L.; Tretiak, S.; Martin, R. L.; Chi, X.; Crone, B. K.; Ramirez, A. P.; Taylor, A. J. *Physical Review Letters* **2009**, *102*, 3–6.

(24) Zimmerman, P. M.; Bell, F.; Casanova, D.; Head-Gordon, M. *Journal of the American Chemical Society* **2011**, *133*, 19944–19952.

(25) Chan, W. L.; Ligges, M.; Zhu, X. Y. *Nature Chemistry* **2012**, *4*, 840–845.

(26) Chan, W. L.; Berkelbach, T. C.; Provorse, M. R.; Monahan, N. R.; Tritsch, J. R.; Hybertsen, M. S.; Reichman, D. R.; Gao, J.; Zhu, X. Y. *Accounts of Chemical Research* **2013**, *46*, 1321–1329.

(27) Birech, Z.; Schwoerer, M.; Schmeiler, T.; Pflaum, J.; Schwoerer, H. *Journal of Chemical Physics* **2014**, *140*, DOI: `10.1063/1.4867696`.

(28) Burdett, J. J.; Gosztola, D.; Bardeen, C. J. *Journal of Chemical Physics* **2011**, *135*, DOI: `10.1063/1.3664630`.

(29) Wilson, M. W.; Rao, A.; Johnson, K.; Gélinas, S.; Di Pietro, R.; Clark, J.; Friend, R. H. *Journal of the American Chemical Society* **2013**, *135*, 16680–16688.

(30) Seeger, P. A.; Daemen, L. L.; Larese, J. Z. *Nuclear Instruments and Methods in Physics Research, Section A: Accelerators, Spectrometers, Detectors and Associated Equipment* **2009**, *604*, 719–728.

(31) Cavaye, H. *Angewandte Chemie - International Edition* **2019**, *58*, 9338–9346.

(32) Vong, D.; Novak, E.; Moulé, A.; Daemen, L. *Review of Scientific Instruments* **2023**, *Submitted, in review.*

(33) Kresse, G.; Hafner, J. *Physical Review B* **1993**, *47*, 558–561.

(34) Kresse, G.; Furthmüller, J. *Computational Materials Science* **1996**, *6*, 15–50.

(35) Kresse, G.; Furthmüller, J. *Physical Review B* **1996**, *54*, 11169–11186.

(36) Kresse, G.; Joubert, D. *Physical Review B* **1999**, *59*, 1758–1775.

(37) Togo, A.; Tanaka, I. *Scr. Mater.* **2015**, *108*, 1–5.

(38) Togo, A. *J. Phys. Soc. Jpn.* **2023**, *92*, 012001.

(39) Ramirez-Cuesta, A. J. *Computer Physics Communications* **2004**, *157*, 226–238.

(40) Weigend, F.; Ahlrichs, R. *Physical Chemistry Chemical Physics* **2005**, *7*, 3297–3305.

(41) Weigend, F. *Physical Chemistry Chemical Physics* **2006**, *8*, 1057–1065.

(42) Grimme, S.; Antony, J.; Ehrlich, S.; Krieg, H. *Journal of Chemical Physics* **2010**, *132*, 1–19.

(43) Grimme, S.; Ehrlich, S.; Goerigk, L. *Journal of Computational Chemistry* **2011**, *32*, 1456–1465.

(44) Goerigk, L.; Hansen, A.; Bauer, C.; Ehrlich, S.; Najibi, A.; Grimme, S. *Physical Chemistry Chemical Physics* **2017**, *19*, 32184–32215.

(45) Smith, M. B.; Michl, J. *Annual Review of Physical Chemistry* **2013**, *64*, 361–386.

(46) Sebastian, L.; Weiser, G.; Bassler, H. *Chemical Physics* **1981**, *61*, 125–135.

(47) Geacintov, N. E.; Burgos, J.; Pope, M.; Strom, C. *Chemical Physics Letters* **1971**, *11*, 504–508.

(48) Thorsmølle, V. K.; Averitt, R. D.; Demsar, J.; Smith, D. L.; Tretiak, S.; Martin, R. L.; Chi, X.; Crone, B. K.; Ramirez, A. P.; Taylor, A. J. *Physica B: Condensed Matter* **2009**, *404*, 3127–3130.

(49) Marciniak, H.; Fiebig, M.; Huth, M.; Schiefer, S.; Nickel, B.; Selmaier, F.; Lochbrunner, S. *Physical Review Letters* **2007**, *99*, 1–4.

(50) Jundt, C.; Klein, G.; Sipp, B.; Le Moigne, J.; Joucla, M.; Villaeys, A. A. *Chemical Physics Letters* **1995**, *241*, 84–88.

(51) Musser, A. J.; Liebel, M.; Schnedermann, C.; Wende, T.; Kehoe, T. B.; Rao, A.; Kukura, P. *Nature Physics* **2015**, *11*, 352–357.

(52) Tomkiewicz, Y.; Groff, R. P.; Avakian, P. *The Journal of Chemical Physics* **1971**, *54*, 4504–4507.

(53) Smith, M. B.; Michl, J. *Chemical Reviews* **2010**, *110*, 6891–6936.

(54) Wilson, M. W.; Rao, A.; Clark, J.; Kumar, R. S. S.; Brida, D.; Cerullo, G.; Friend, R. H. *Journal of the American Chemical Society* **2011**, *133*, 11830–11833.

(55) He, R.; Tassi, N. G.; Blanchet, G. B.; Pinczuk, A. *Applied Physics Letters* **2010**, *96*, 1–4.

(56) Kabakchiev, A.; Kuhnke, K.; Lutz, T.; Kern, K. *ChemPhysChem* **2010**, *11*, 3412–3416.

(57) Rao, A.; Wilson, M. W.; Albert-Seifried, S.; Di Pietro, R.; Friend, R. H. *Physical Review B - Condensed Matter and Materials Physics* **2011**, *84*, 1–8.

(58) Marciniak, H.; Pugliesi, I.; Nickel, B.; Lochbrunner, S. *Physical Review B - Condensed Matter and Materials Physics* **2009**, *79*, 1–8.

(59) Zade, S. S.; Zamoshchik, N.; Reddy, A. R.; Fridman-Marueli, G.; Sheberla, D.; Bendikov, M. *Journal of the American Chemical Society* **2011**, *133*, 10803–10816.

(60) Shao, Y.; Sista, S.; Chu, C. W.; Sievers, D.; Yang, Y. *Applied Physics Letters* **2007**, *90*, DOI: `10.1063/1.2709505`.

(61) Wang, G.; Zhang, C.; Liu, Z.; Wang, R.; Ma, H.; Wang, X.; Xiao, M. *Journal of Physical Chemistry A* **2020**, *124*, 10447–10456.

(62) Grumstrup, E. M.; Johnson, J. C.; Damrauer, N. H. *Physical Review Letters* **2010**, *105*, 1–4.

(63) Stern, H. L.; Cheminal, A.; Yost, S. R.; Broch, K.; Bayliss, S. L.; Chen, K.; Tabachnyk, M.; Thorley, K.; Greenham, N.; Hodgkiss, J. M.; Anthony, J.; Head-Gordon, M.; Musser, A. J.; Rao, A.; Friend, R. H. *Nature Chemistry* **2017**, *9*, 1205–1212.

(64) Harrelson, T. F. et al. *Materials Horizons* **2019**, *6*, 182–191.

(65) Vong, D.; Nematiaram, T.; Dettmann, M. A.; Murrey, T. L.; Cavalcante, L. S.; Gurses, S. M.; Radhakrishnan, D.; Daemen, L. L.; Anthony, J. E.; Koski, K. J.; Kronawitter, C. X.; Troisi, A.; Moulé, A. J. *Journal of Physical Chemistry Letters* **2022**, *13*, 5530–5537.

(66) Holmes, D.; Kumaraswamy, S.; Matzger, A. J.; Peter, K.; Vollhardt, C. *Chemistry A European Journal* **1999**, *5*, 3399–3412.

Chapter 6

Unpublished work

6.1 Introduction

The photochemistry sticks were designed, built, and used on the VISION beamline within the year that I spent at Oak Ridge. The initial few months of planning including brainstorming and testing a variety of ideas. Some of the concepts tested were passive systems, wherein the materials were loaded into thin geometries to try and increase photoilluminated surface area, while other concepts were active systems that used external forces to mix powder materials.

6.1.1 Passive concepts

One of the first concepts tested was mixing transparent media with the sample. Since quartz has a relatively small incoherent neutron cross section and high transmission in the desired wavelengths, quartz was chosen as the transparent media. Quartz tube was broken and put through a sieve to separate by size, as shown in Figure 6.1(a), and placed into a quartz tube. To reduce the transmission out of the tube, the quartz tube was sputter coated with silver.

A 520 nm laser pointer was used at one end, illuminated pointing towards a power meter, and data points taken for various configurations. The data for the transmission experiment is shown in Figure 6.2. The quartz pieces reduced the measured intensity by >95%, with the best case being the larger quartz pieces with silver coating. For a more uniform media, this experiment was repeated with commercially obtained 0.5 mm and 1

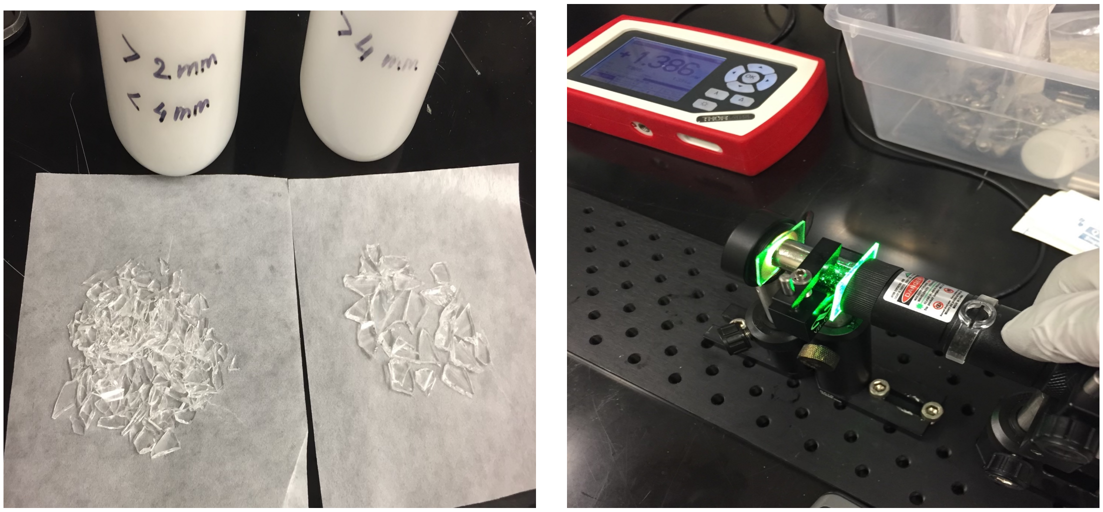

(a) (b)

Figure 6.1. Transmission experiment using quartz pieces for passive concept. Quartz pieces were made from smashing quartz tubes and different sizes were separated using a sieve. a) Quartz pieces separated by size. b) Transmission measurement through silver coated quartz tube.

mm diameter spherical quartz beads, with power measured at the opposite end reduced >99%. Therefore, we expected with the inclusion of sample that the quartz media concept would not be a viable method.

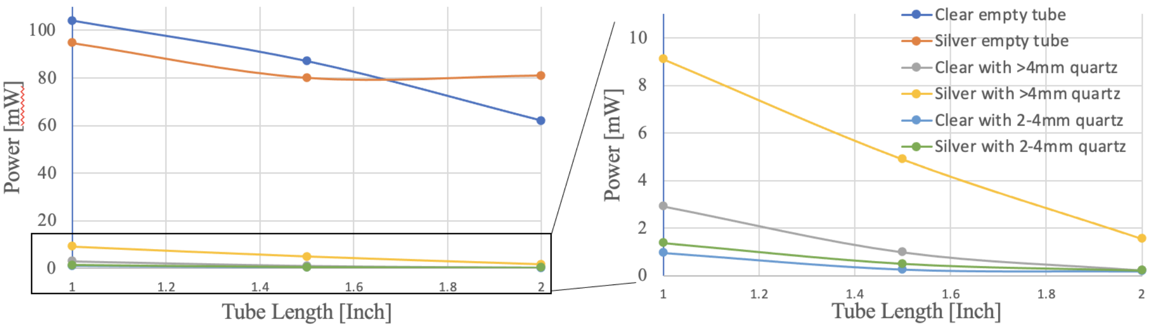

Figure 6.2. Data showing the power measured at the opposite end of the quartz tube.

For the next concept, polystyrene was spin coated to form a film, Figure 6.3, to test wrapping around a quartz tube. The film was removed from the substrate and floated in a water bath (Figure 6.4), and a quartz tube was used to pick the sample up (Figure 6.5). This initial measurement was placed into a standard aluminum sample can and INS was measured. This tested whether there was enough material to be visible on VISION. We shown that the count rate was adequate and a film wrapped around a quartz tube should be a viable candidate for future photochemistry experiments.

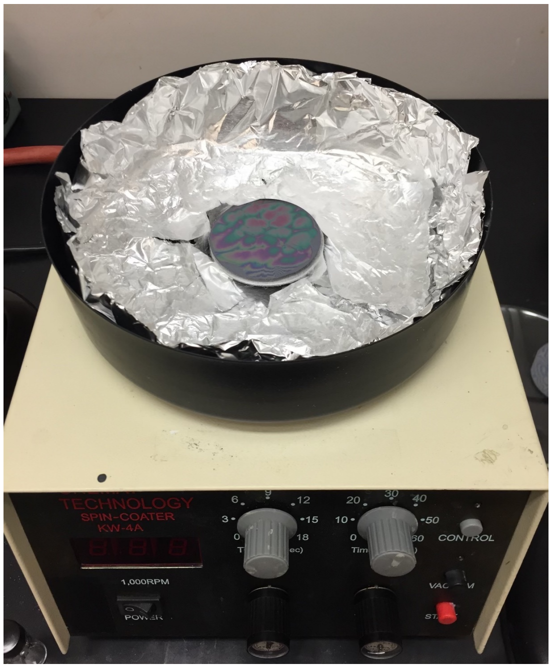

Figure 6.3. Spin coating polystyrene film.

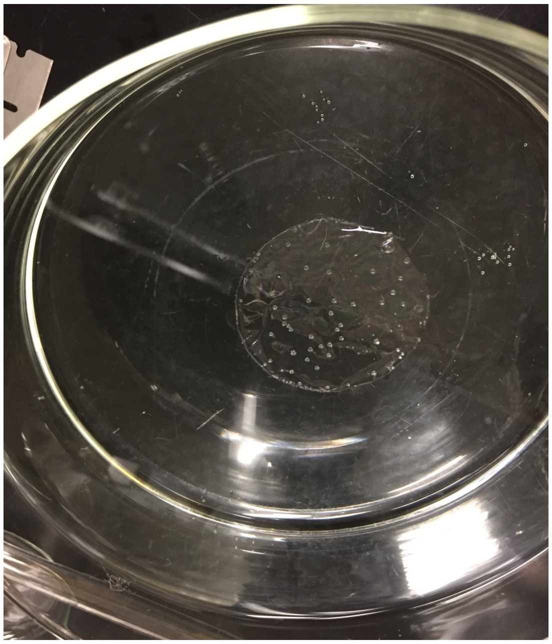

Figure 6.4. Floating polystyrene films in water.

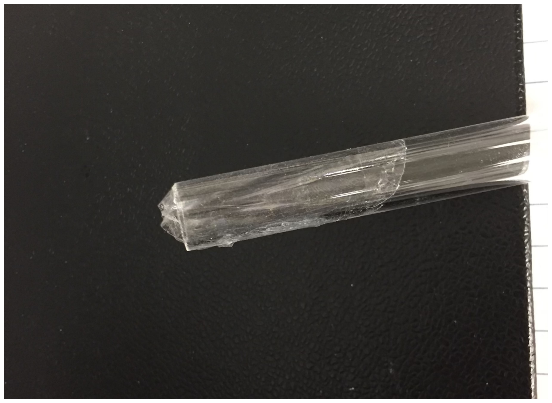

Figure 6.5. Polystyrene film wrapped around quartz tube.

6.1.2 Active concepts

Active concepts that mixed the sample were also explored. One idea was ultrasonic mixing, which uses ultrasonic hammers placed below the sample container. While the powder samples jumped around vigorously in the container, ultrasonic mixers require very large power sources, a few kW, and the samples would dump too much energy into the CCR.

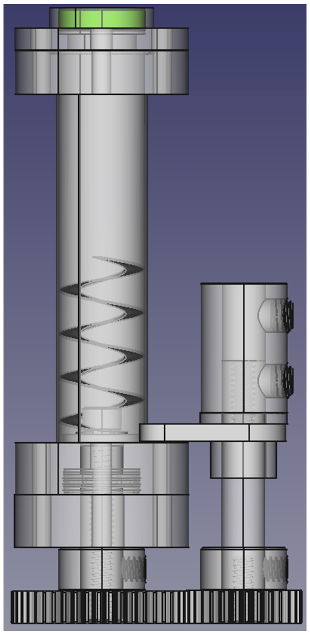

Figure 6.6. Computer generated concept of the spiral mixer.

The next idea tested was a spiral mixer, Figure 6.6. The idea was to use a motor and drive shaft down the length of the CCR to rotate a spiral mixer, repeated moving the sample from the bottom of the sample can to to top. The cap holds an optical window to allow light to pass. To test this concept, the spiral blades were 3d printed (Figure 6.7), and also small springs were purchased as make-shift spiral blades. The blades fit within a plastic tube. To test the mixing, coffee grounds and sugar was mixed with the blades connected to a stepper motor. The 3D printed plastic broke immediately, and the spring did not mix well.

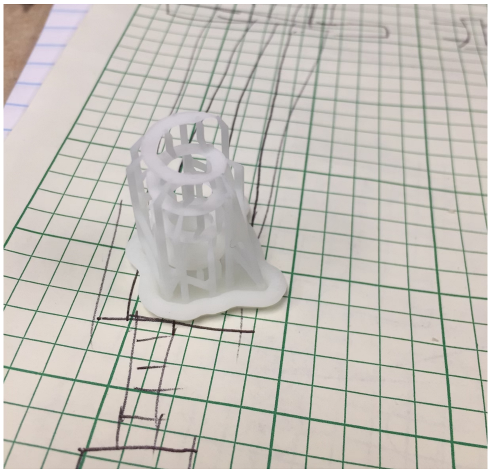

Figure 6.7. Plastic 3D printed spiral mixer blades.

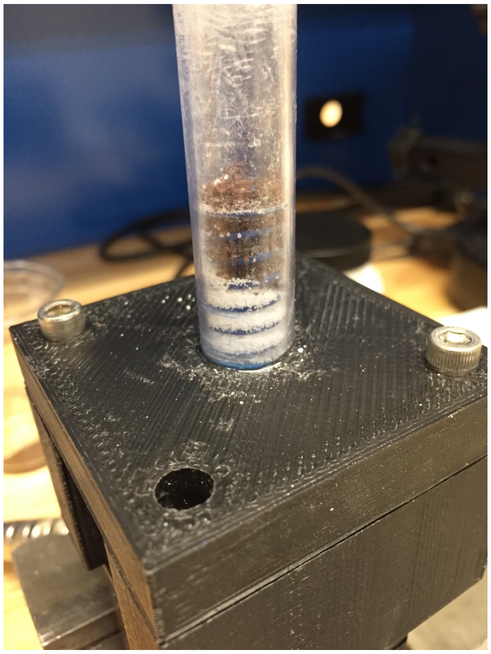

Figure 6.8. Springs used as spiral mixer blades.

To have spiral mixing blades more reminescent of large commercial mixers, the blades were 3D printed in aluminum with lips around the edge to better pick up and transport the coffee and sugar, Figure 6.9. Unfortunately, the two materials still did not mix.

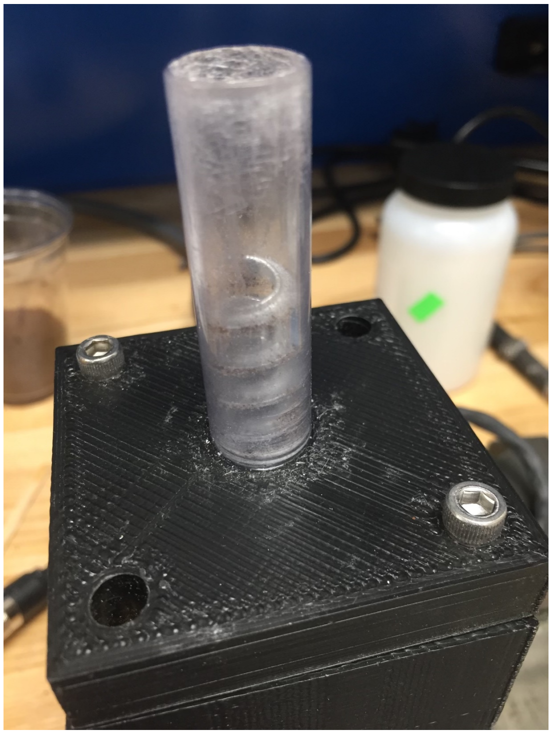

Figure 6.9. 3D printed aluminum for spiral mixing blades.

Another idea was to test a tumbler concept. The tumbler was made using 30 mm diameter aluminum sample cans, and a popsicle stick was glued to the edge to mix the coffee components.

(a) (b)

Figure 6.10. Make shift test of tumbler concept.

The mixing was achieved with this configuration, and we moved forward with the tumbler mixing system.

Some of the issues with mechanical motion at cryogenic temperatures are the thermal contraction and increase in coefficient of friction. The initial idea to transfer rotational motion was to use sprockets and chains, Figure 6.11, which has been used at ORNL for previous cryogenic motion.

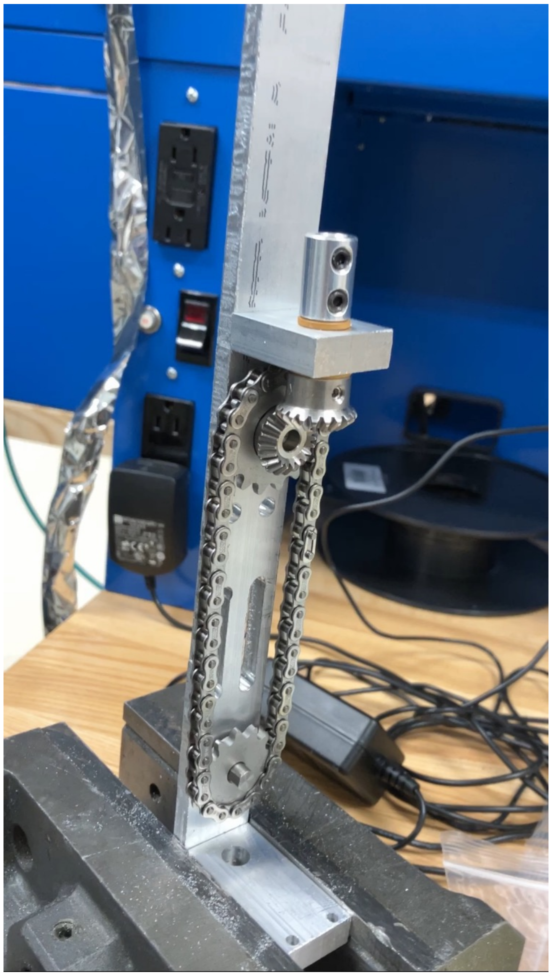

Figure 6.11. Chain and sprockets used for the tumbler concept.

While the chain and sprocket can be used, the cryogenic conditions cause very large increases in frictional forces. The working chain and sprocket systems used very large motors that could overcome the frictional forces. These motors are too large for our design, as we wanted a sample stick that could be portable and handled by a single user. While ultimately the stepper motor used in our design has a reasonably high maximum torque of 120 oz-in, the frictional forces at 80 K was too high. Changing the design to ultimately use spur gears resulted in very smooth and much lower friction down to 5 K.

Appendix A

SI for Quantitative Hole Mobility Simulation and Validation in Substituted Acenes

A.0.1 Finite displacement supercell

Here we describe the finite displacement supercell method in a simplified 2D convention to obtain inputs to the scattering law. Using Phonopy, finite displacement is a method to obtain the phonon eigenvectors (phonon displacement vectors) and eigenvalues (phonon frequencies) beyond the Γ-point (as some DFT packages are limited to Γ-point phonons or can only handle smaller systems). A supercell with cell dimensions >10 Å in each crystallographic direction of the relaxed primitive cell is created and a displaced atom from its equilibrium position induces a force on every other atom (large enough cell to minimize the chance of the displaced atom self-interaction, small enough displacement to stay in the harmonic regime), and can be systematically applied to every other symmetry in-equivalent atoms to obtain a matrix of pairwise force constants,

$$\Phi_{nimj} = \frac{\partial F_{ni}}{\partial u_{mj}} \tag{A.1}$$

where F is the force, u is the displacement, subscripts n and m are atom labels, and i and j are Cartesian directions. The mass weighted Fourier transform of the force constant matrix,

$$\tilde{D} = \frac{\Phi_{nimj}}{\sqrt{m_n m_m}} e^{i\vec{q}\cdot(r_{mj}-r_{ni})} \tag{A.2}$$

is defined as the dynamical matrix, where m are the atom masses. Diagonalizing the dynamical matrix gives the solutions to the harmonic approximation's eigenvalue problem, specifically the square of the vibrational mode frequencies and atomic displacements,

$$[\tilde{D}][\varphi] = \omega^2[\varphi] \tag{A.3}$$

The solutions to the eigenvalue problem are inputs to OCLIMAX[1], a proprietary software written by the VISION vibrational neutron spectrometer beamline scientists at Oak Ridge National Lab, which reproduces spectra with the instrument sensitivity and spectral response of VISION, given by

$$S(Q, n\omega_s) = \frac{Q \cdot U_s^{2n}}{n!} e^{-Q \cdot U_{total}^2} \quad U_s = \sqrt{\frac{\hbar}{2m\omega_s}} \varphi_s \tag{A.4}$$

which is the reduced form of the scattering law for low temperature, hydrogen containing materials, where n is the population of phonon mode s, and Q is the neutron momentum transfer.

A.0.2 Dynamic disorder and mobility

The methodology and computational detail(s) are identical to those presented by the Troisi group[2] except for the calculation of the phonons. Briefly, the following standard Hamiltonian is used,

$$\begin{aligned} \hat{H} = \\ & \sum_i \epsilon_i \hat{c}_i^+ \hat{c}_i + \sum_{<ij>} J_{ij}^0 \hat{c}_i^+ \hat{c}_j + \sum_M \hbar\omega_M (\hat{a}_M^+ \hat{a}_M + \frac{1}{2}) + \\ & \sum_{i,M} g_{i,M} \frac{1}{\sqrt{2}} (\hat{a}_M^+ + \hat{a}_M) \hat{c}_i^+ \hat{c}_i + \sum_{i \neq j, M} g_{ij,M} \frac{1}{\sqrt{2}} (\hat{a}_M^+ + \hat{a}_M) \hat{c}_i^+ \hat{c}_j. \end{aligned}$$

The first two terms indicate the electronic part of the Hamiltonian, the third term describes the lattice phonons, and the last two terms describe the local and non-local electron-phonon couplings. ϵ_i denotes the on-site electronic energy of the hole; J^0_{ij} is the transfer integral between adjacent molecules at the equilibrium geometry; $\hbar\omega_M$ and k_BT are the phonons and the thermal energies, respectively; $\hat{c}^+_i(\hat{c}_i)$ are the creation (annihilation) operators for a hole at site i (there is one state per site); $< ij >$ is the nearest-neighbour pairs of occupied sites; $\hbar$ is the reduced Planck constant; ω_M is the phonon frequency of mode M; $g_{i,M}$ and $g_{ij,M}$ are the local and non-local electron-phonon couplings measuring the strength of interaction between charge carrier and intra-molecular and inter-molecular vibrations; and $\hat{a}^+_M(\hat{a}_M)$ are the phonon creation (annihilation) operators, respectively. The local electron-phonon coupling causes the modulation of the site energies (i.e. local dynamic disorder) while the non-local term leads to the fluctuation of the transfer integral, which is typically of the same order of magnitude as the transfer integral itself (i.e. non-local dynamic disorder).[3] We computed the transfer integral using the below equation,

$$J_{ij} =< \varphi_i|\hat{F}|\varphi_j > \tag{A.5}$$

where φ_i and φ_j are the localized highest-occupied molecular orbital (HOMO) of molecule i and j, respectively, and $\hat{F}$ stands for the Fock operator of the dimer system. Calculations of the transfer integrals are carried out based on *ab initio* methods at the B3LYP/3-21g* level of the theory as implemented in Gaussian16.[4] The sign of J_{ij} will depend on the phases of φ_i and φ_j, being negative if the signs of the overlapping wavefunctions are opposite, and positive if the signs are alike. The local electron-phonon coupling is computed using the nuclear displacement between equilibrium positions before and after the charge transfer, as explained previously[5, 6].

To consider the impact of local electron-phonon coupling on the mobility, we defined an energy cut-off ($2k_BT$) to consider the local electron-phonon coupling classically; all the local modes above this cut-off (i.e. $\hbar\omega_M \geq 2k_BT$) contribute to the calculation of a renormalization factor f as explained in Ref. [7] and defined as f=$exp(-\sum_M(g_{i,M}/\hbar\omega_M)^2(2\mathrm{N}_M + 1))$ where $(g_{i,M}/\hbar\omega_M)$ is the dimensionless Huang-Rhys factor[8] or the local electron-phonon coupling for nuclear mode M of frequency ω_M and $N_M = (exp(\hbar\omega_M/K_BT)-1)^{-1}$

stands for the occupation number. T was set to 300 K and all the modes below this cut-off (i.e. $\hbar\omega_M < 2k_BT$) contribute to the on-site energy fluctuations $\sigma_{local} = \sqrt{\lambda_S k_B T}$ where $\lambda_S = \sum_M g_{i,M}^2/\hbar\omega_M$ contains contributions only from low-frequency modes.

The non-local electron-phonon coupling $g_{ij,M}$ is a measure of how the transfer integral between molecular pair i and j is modulated by a displacement along a phonon mode M and can be expressed as below[9], where ∇J_{ij} is the gradient of the transfer integral with respect to the atomic dispalcement and Q_M is the vector that denotes the Cartesian displacements of mode M,[10]

$$g_{ij,M} = \nabla J_{ij} Q_M \tag{A.6}$$

This coupling gives access to the non-local dynamic disorder σ_{ij} a global measure of the fluctuations of the transfer integrals J_{ij} when compared with their average values,[11]

$$\sigma_{ij}^2 = \frac{1}{N}\sum_M \frac{|g_{ij}^M|^2}{2} coth(\frac{\hbar\omega_M}{2k_BT}) \tag{A.7}$$

With N being the number of points employed to sample the q-space.

TLT[12] is used to evaluate the mobility as it has proved able to produce results in agreement with more complicated quantum dynamics propagation schemes[13, 14] as well as experimental measurements.[9] According to this theory, the effects of dynamic disorder can be monitored by a transient localization over a length L within a fluctuation time scale given by the inverse of the typical intermolecular oscillation frequency $\tau \sim 1/\omega_0$. In this work, τ is set to 0.13 ps, wherein it was concluded in Ref. [15] that τ does not change much between molecules, and that as $\mu \propto L_\tau^2/\tau$, L_τ^2 increasing with fluctuation time results in a weak dependence of τ on μ_h for the substituted acenes tested. The charge mobility in this theory is expressed as,

$$\mu = \frac{e}{k_BT}\frac{L^2}{2\tau} \tag{A.8}$$

where e is the electron charge, and L is computed as shown in Ref. [9]. We use the exact diagonalization method proposed in Ref. [16] to calculate the squared transient localization length in the crystal's high-mobility plane. Furthermore, in the present study, the generalized form of transient localization theory, as described in Ref. [2], is utilized to consider the impact of local electron-phonon coupling in addition to non-local electron-phonon term. As such, an additional on-site gaussian fluctuation σ_{local} (as defined above) is considered which takes into account the impact of low-frequency modes and the transfer integrals and their fluctuations are scaled by the renormalization factor f which considers the high-frequency vibrations.

In contrast to hopping theory, which calculates an incorrect temperature dependence for mobility, or band theory, which calculates nonphysical scattering lengths,[13, 15] TLT demonstrates accurate prediction of charge mobility given fully converged vibrational calculations. Thus, accurate predictions of μ_h allow for potential molecular designs to be rapidly screened and provide insight into high μ design rules. The key reason for selecting this model, is that it connects in a transparent way the vibrational properties, electronic structure, and μ. It is therefore easy within this theory to disentangle the different sources of errors in computing the phonons.

A.0.3 Rubrene partial mode analysis

Rubrene is much less structurally identical than the acenes discussed in this letter, making a direct comparison across similar motions at similar energies impossible. Nevertheless, Rubrene has the highest μ_h of any OSMs, warranting a partial node analysis. The dominant feature at low energy in Fig. S11a ($\sim$30 cm^{-1}) is comprised of multiple phonons, and we highlight the significant modes for Rubrene shown in Figure S14. Rubrene, like C8-BTBT, has opposing axial translation contributing to σ in Figs. S14a and S14b, wherein the phenyl rings reduce the amplitude of axial translation motions. At increasing energies, the weak C–C single bonds connecting the phenyl rings to the tetracene core allow large displacements with complex motions in the phenyl rings, including twisting and flapping, Figs. S14c-e. This in turn elicits an opposing motion from the core resulting in its own twisting, bowing, and other motions.

A.0.4 Supplemental Figures

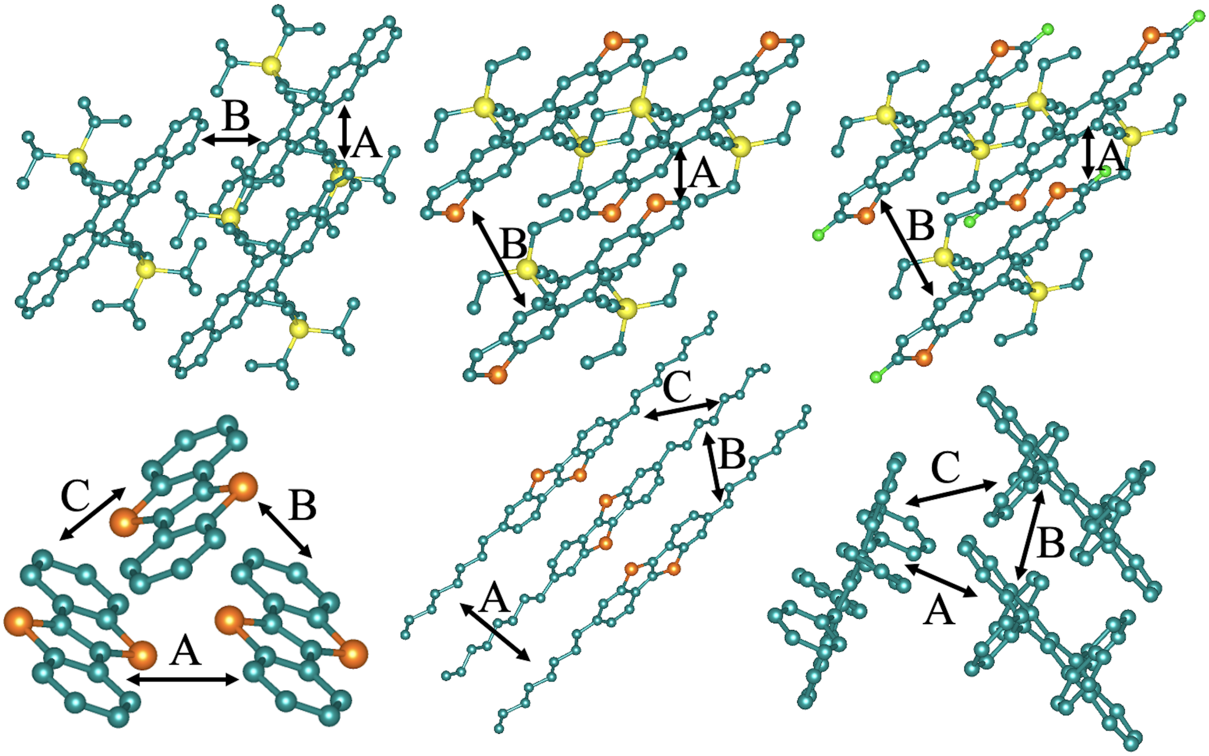

Figure A.1. The materials used for this work. From top-left to bottom-right: TIPS-PN, TESADT, diF-TESADT, BTBT, C8-BTBT, and Rubrene. A, B, and C denote the unique molecular pairs in which transfer integrals are computed. Hydrogen atoms have been omitted for clarity.

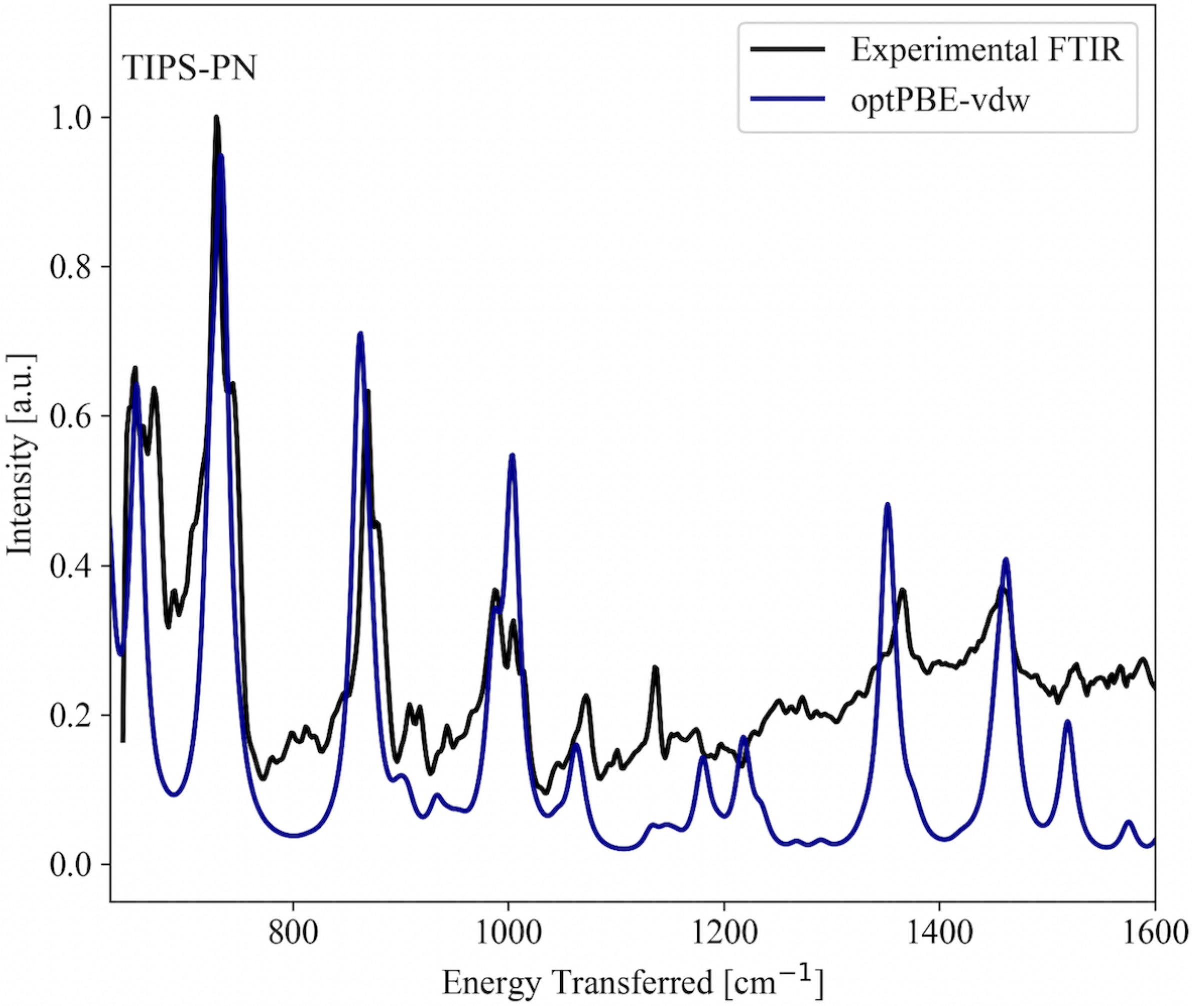

Figure A.2. Comparison of experimental (black) and computed optPBE-vdw (blue) FTIR spectra for TIPS-Pentacene. Energy range from 630-1600 cm^{-1}.

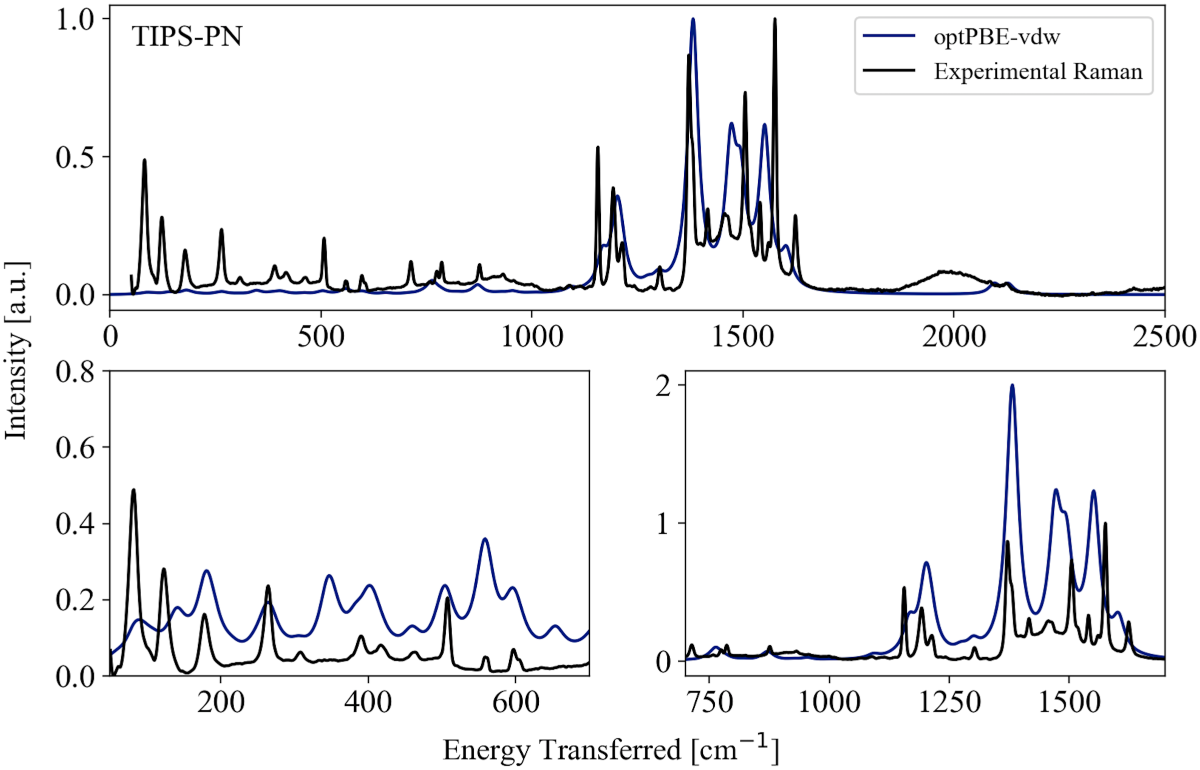

Figure A.3. Comparison of experimental (black) and computed optPBE-vdw (blue) Raman spectra for TIPS-Pentacene. Top spectra include energy range from 0-2500 cm^{-1}. Bottom show zoomed-in and scaled spectra for energies 50-700 cm^{-1} (bottom left) and 700-1800 cm^{-1} (bottom right).

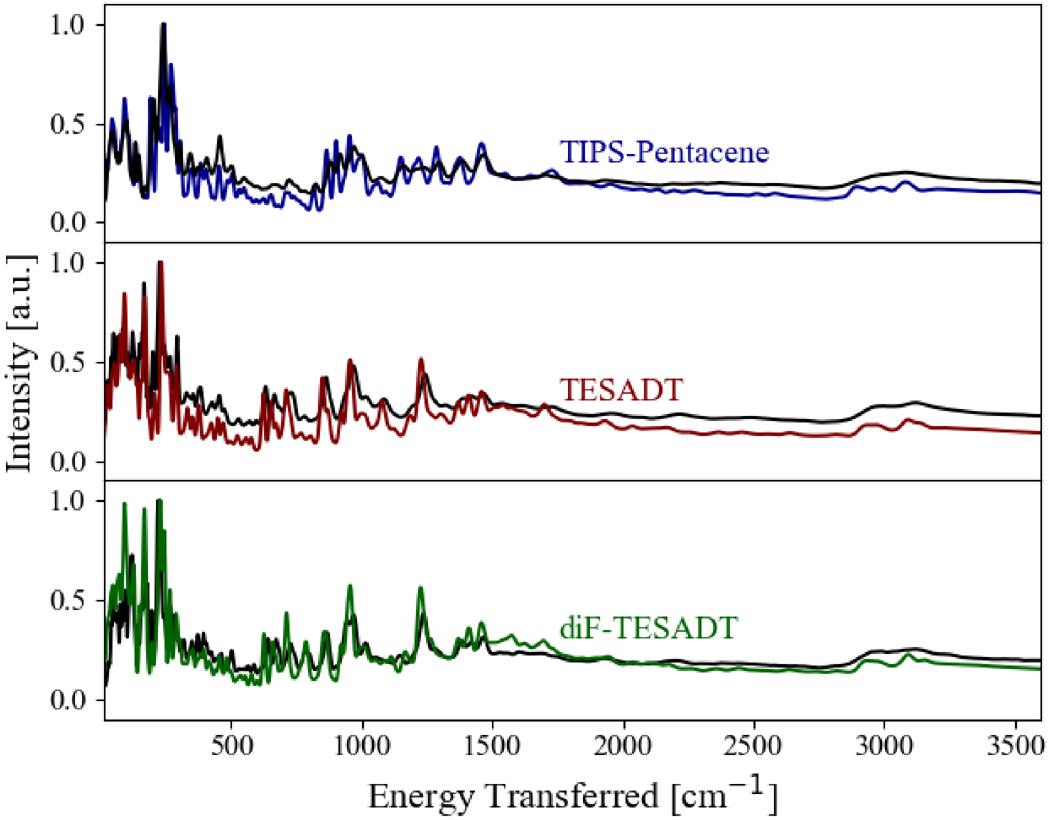

Figure A.4. Comparison of experimental (black) and computed optpbe-vdw inelastic neutron scattering spectra for TIPS-Pentacene (blue), TESADT (maroon), and diFTESADT (green) from 10-3400 cm^{-1}.

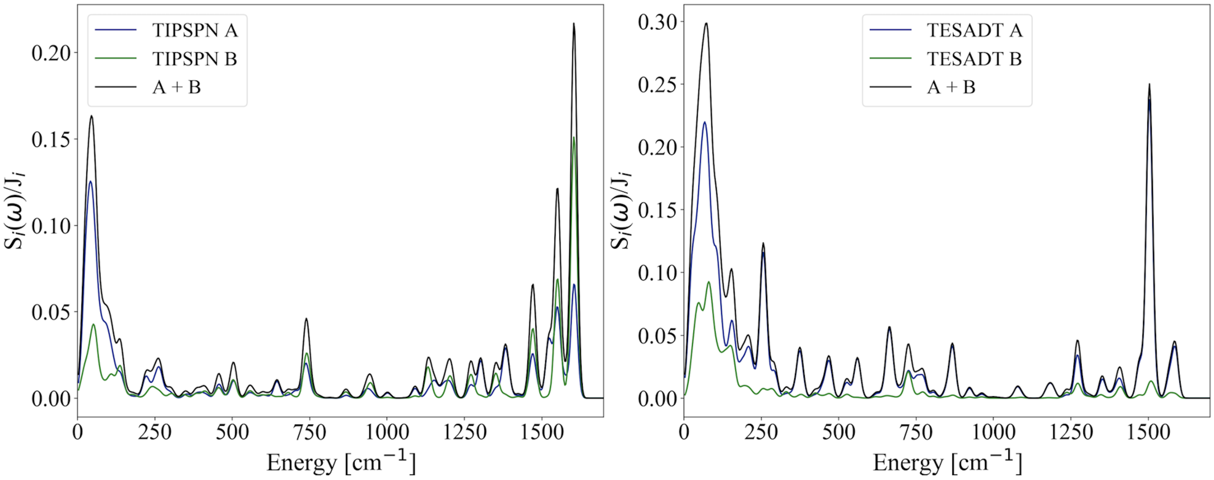

Figure A.5. Accumulative spectral density of electron-phonon coupling in the high mobility plane normalized by the transfer integral for TIPS-Pentacene and TESADT. Subscript i denotes the unique molecular pairs A and B.

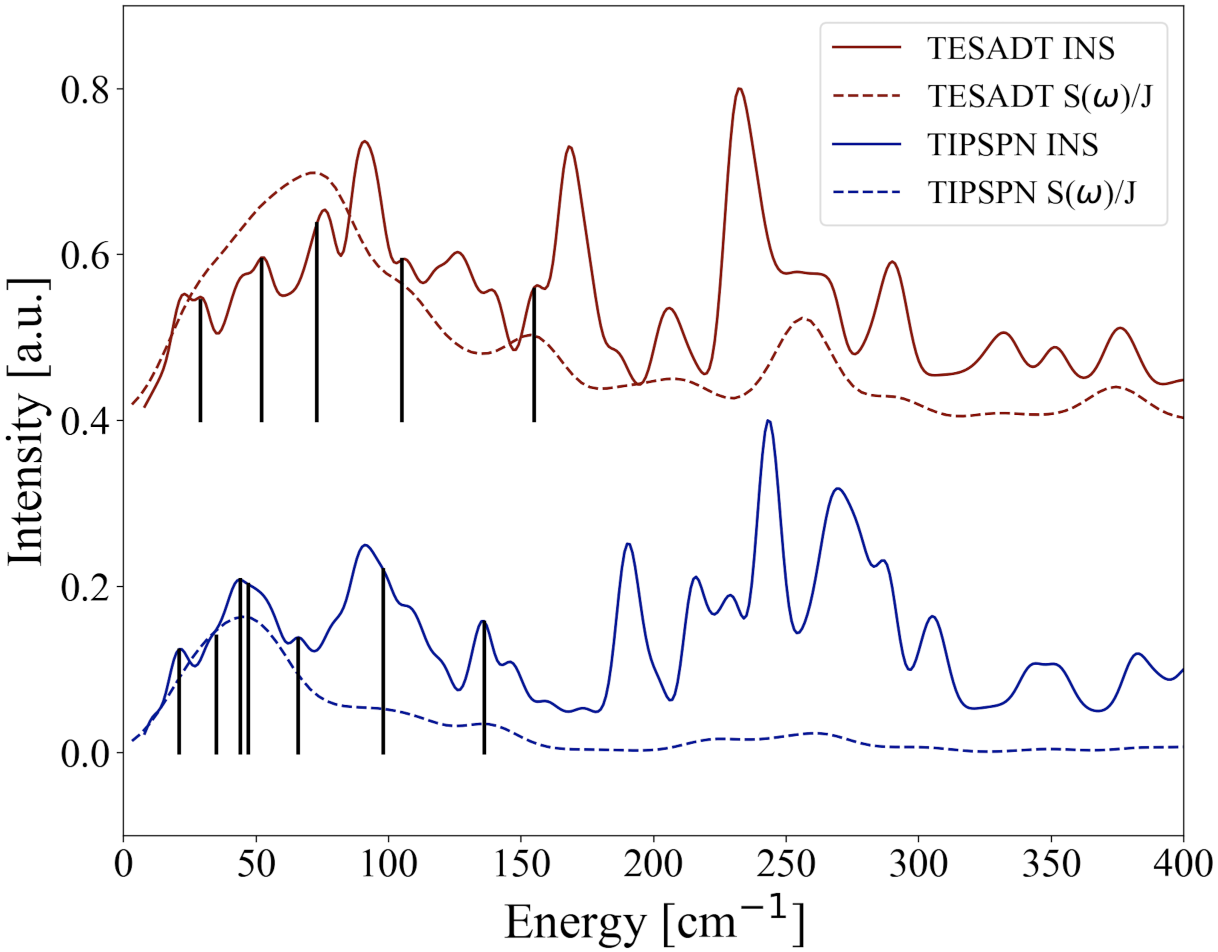

Figure A.6. Normalized spectral density of electron-phonon coupling with respective inelastic neutron scattering for TIPS-Pentacene and TESADT. Black vertical lines highlight the phonon modes shown in Figs. S6 and S7 for TIPS-Pentacene and TESADT, respectively.

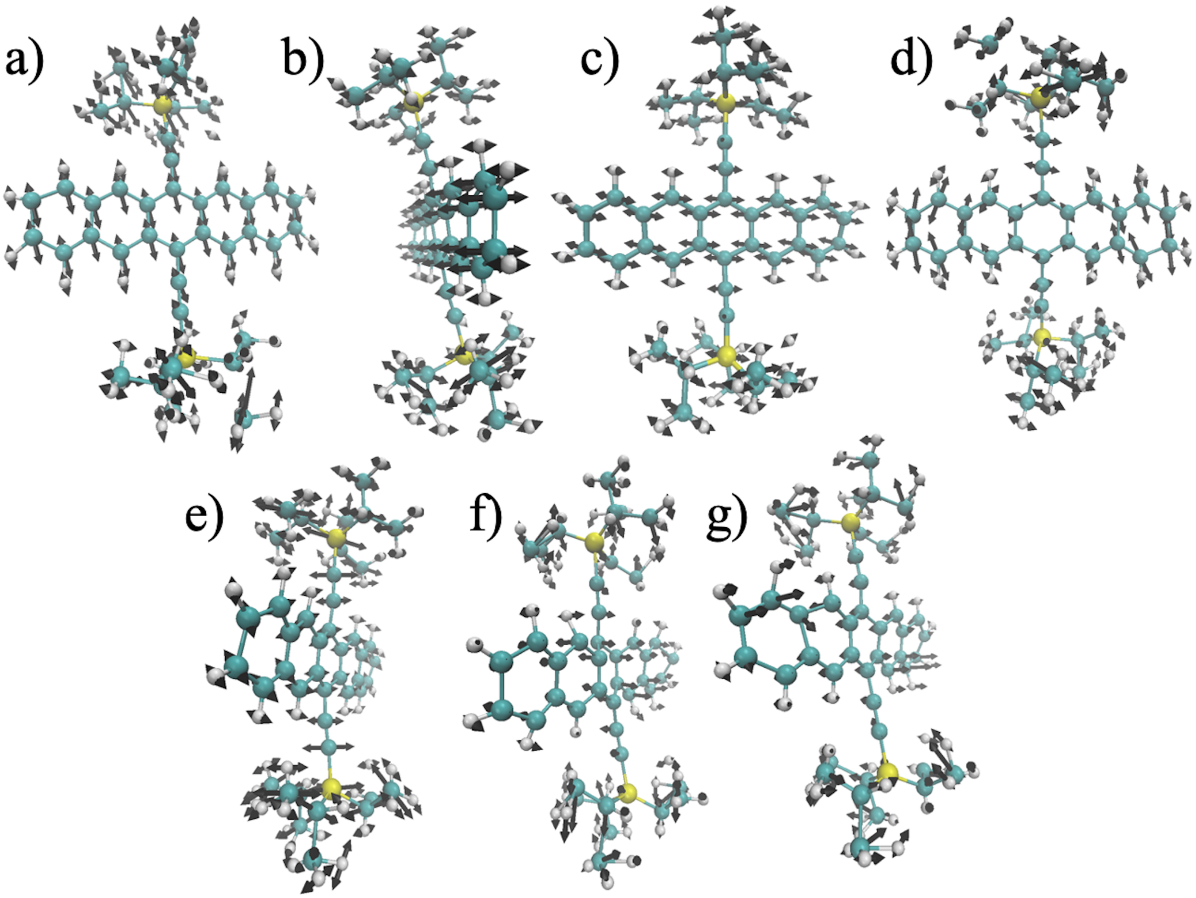

Figure A.7. Phonon modes for TIPS-Pentacene in the low energy region with large contribution to σ. Phonon frequencies in wavenumbers are 21, 35, 44, 47, 66, 98, and 136 in for a-g, respectively. Phonons are shown on one molecule included in the primitive unit cell.

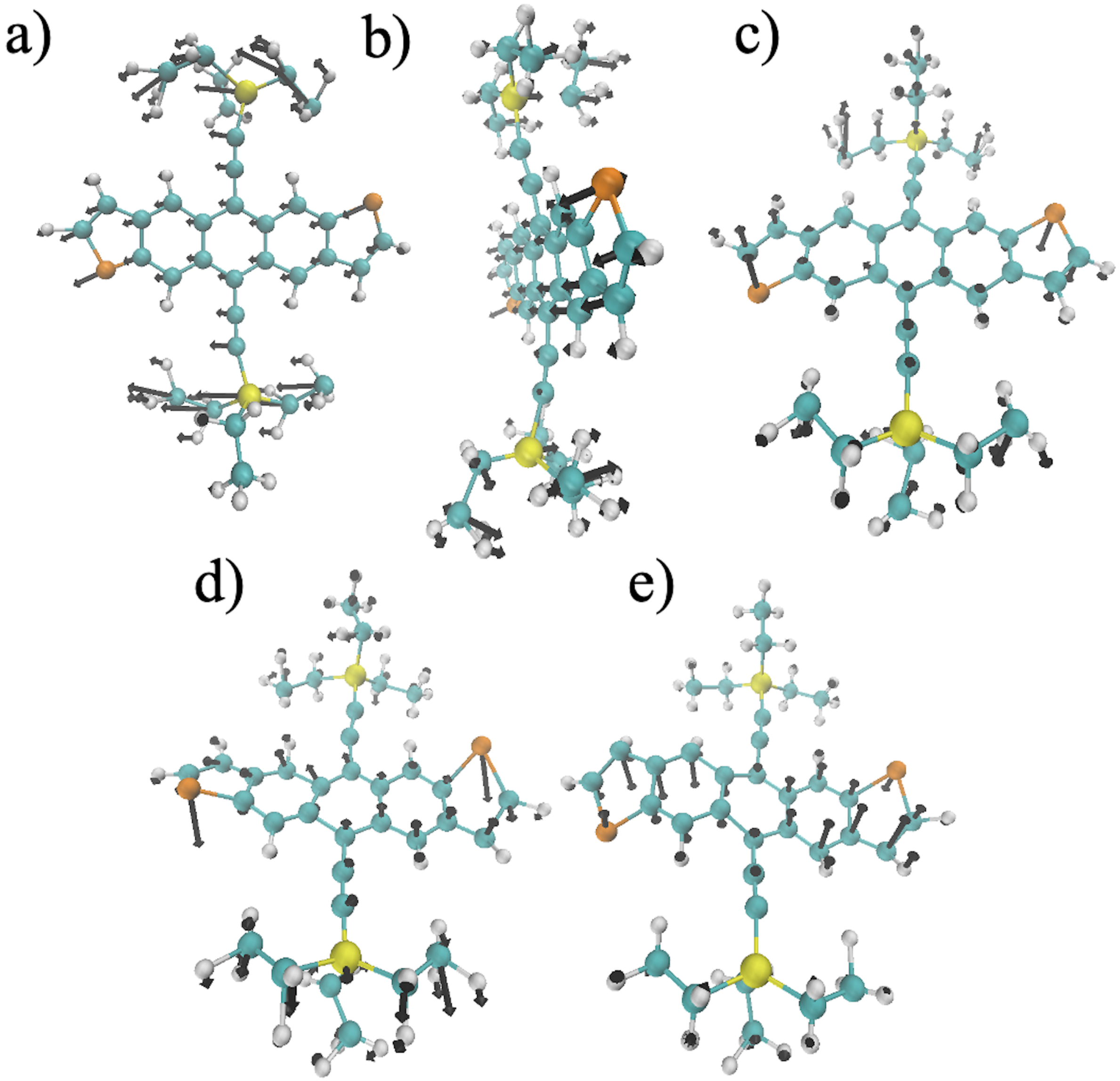

Figure A.8. Phonon modes for TESADT in the low energy region with large contribution to σ. Phonon frequencies in wavenumbers are 29, 52, 73, 105, and 155 in for a-e, respectively. Phonons are shown on one molecule included in the primitive unit cell.

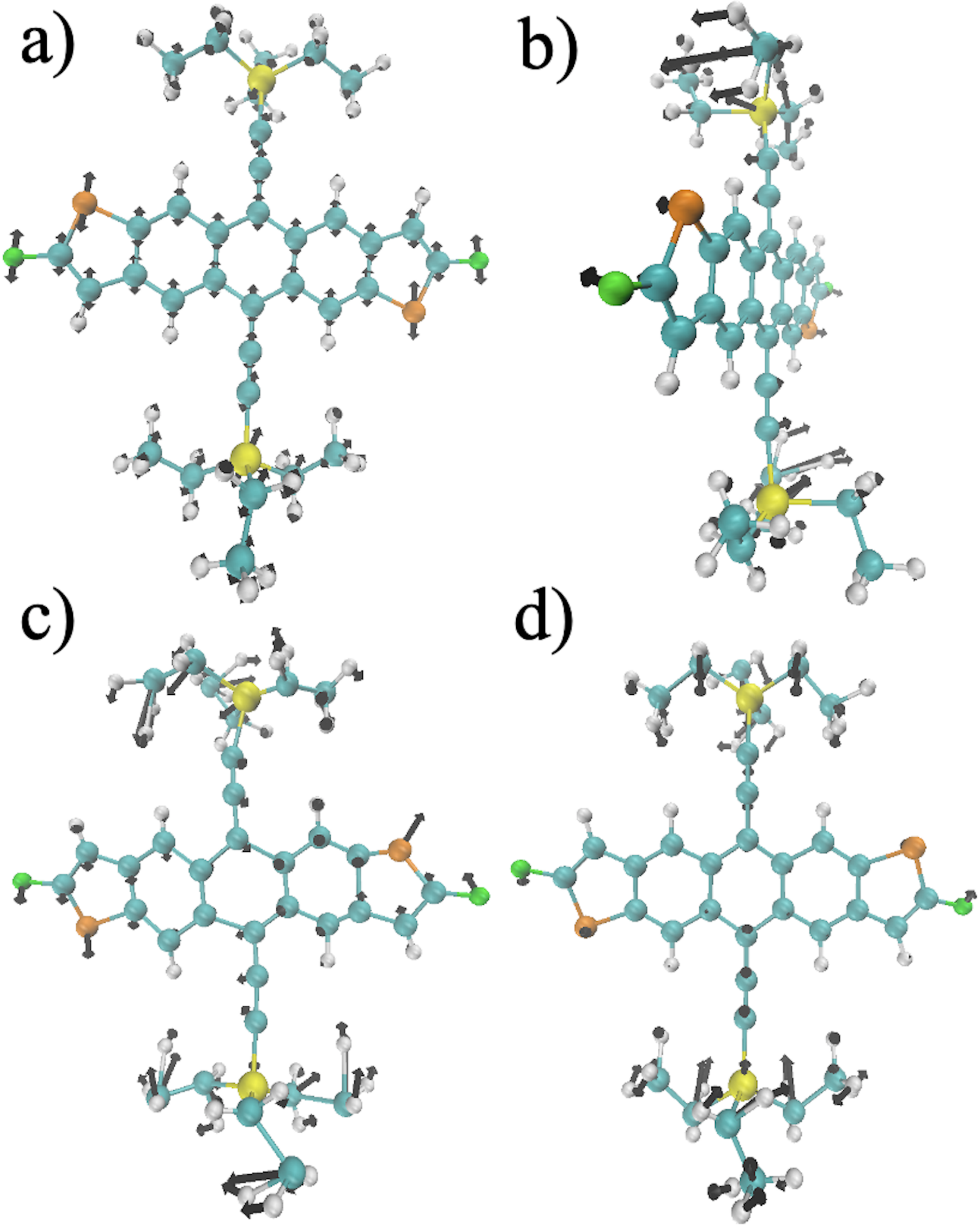

Figure A.9. Phonon modes for diF-TESADT wherein the modes of the former unfluorinated analogue had high σ. Phonon frequencies in wavenumbers are 27, 48, 70, and 150 in for a-d, respectively. Phonons are shown on one molecule included in the primitive unit cell.

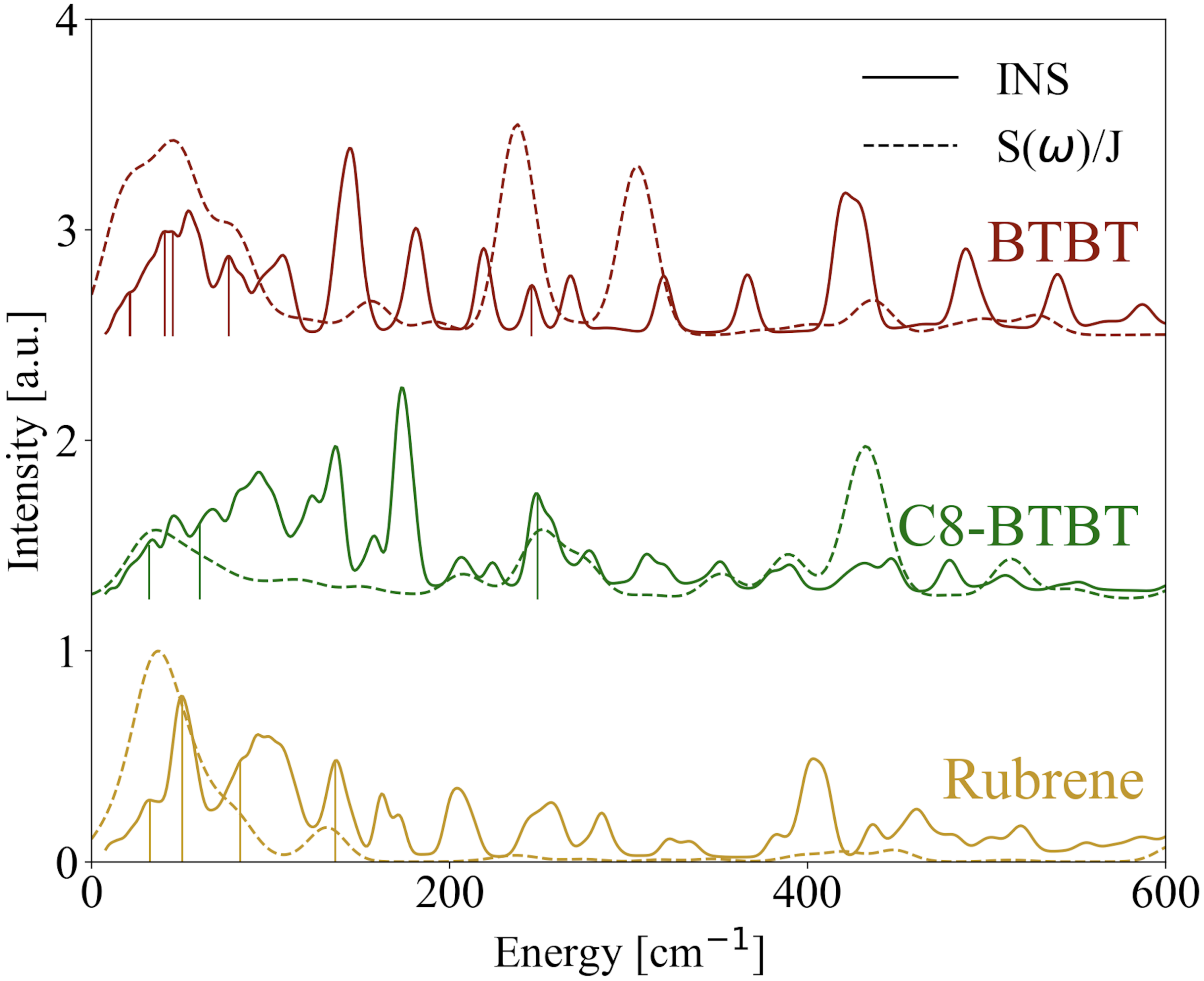

Figure A.10. Normalized spectral density of electron-phonon coupling with respective inelastic neutron scattering for BTBT, C8-BTBT, and Rubrene. Vertical lines highlight the phonon modes shown in Figs. S12-S14 for respective molecules.

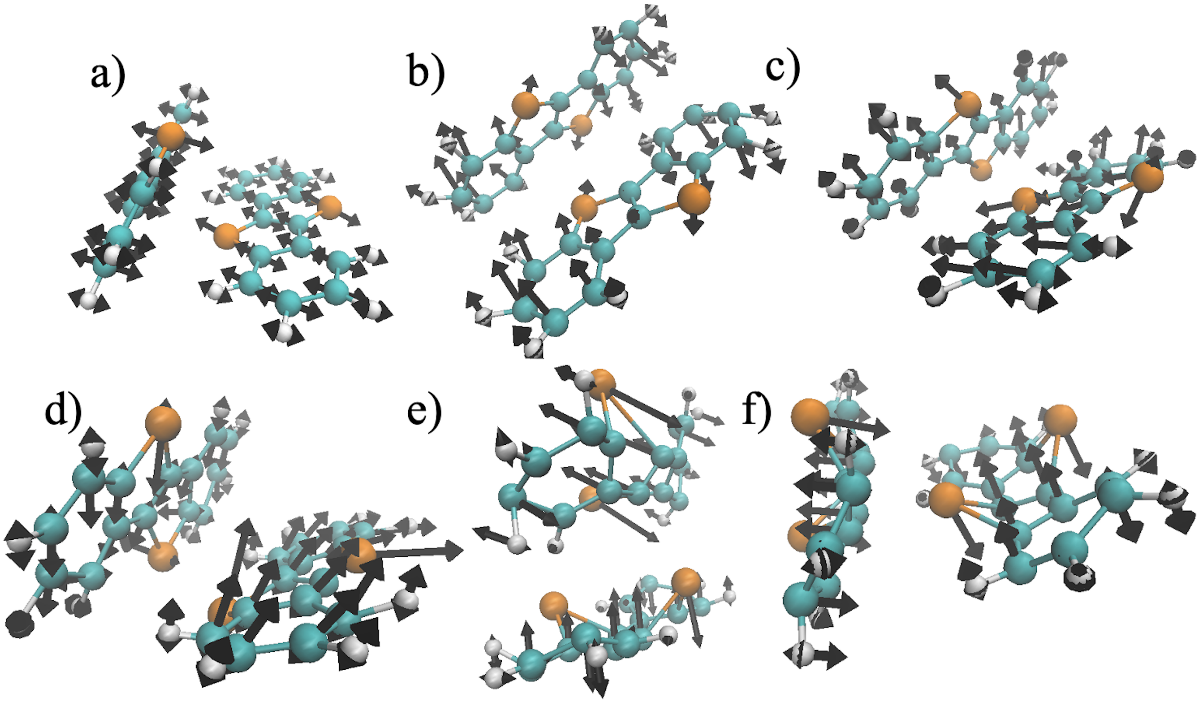

Figure A.11. Phonon modes for BTBT in the low energy region with large contribution to σ. Phonon frequencies in wavenumbers are 21.2, 21.5, 40.8, 45.0, 142.2, and 245.6 for a-f, respectively. Phonons are shown on the two molecules included in the primitive unit cell.

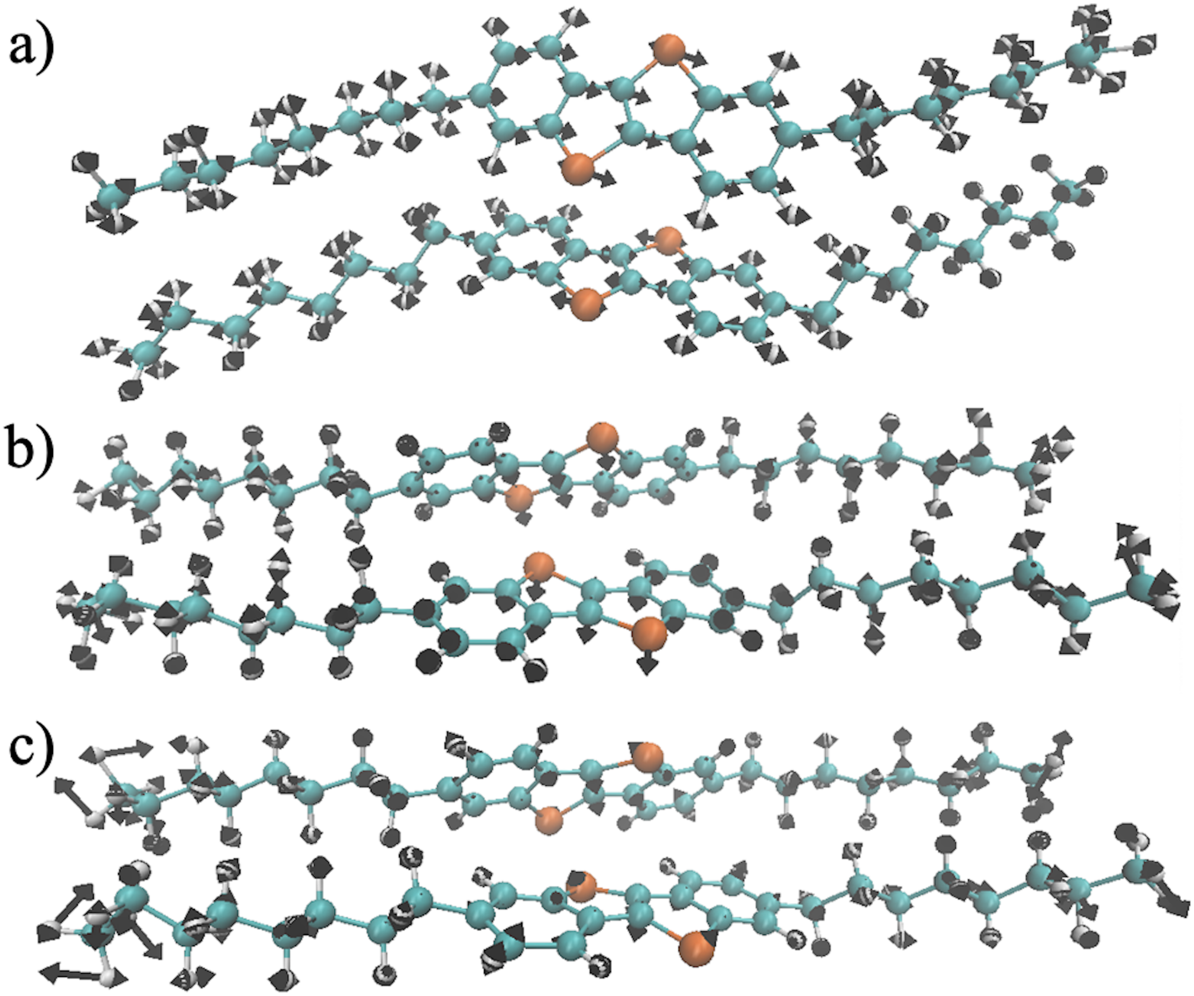

Figure A.12. Phonon modes for C8-BTBT in the low energy region with large contribution to σ relative to BTBT. Phonon frequencies in wavenumbers are 32.0, 60.2, and 260.2 for a-c, respectively. Phonons are shown on the two molecules included in the primitive unit cell.

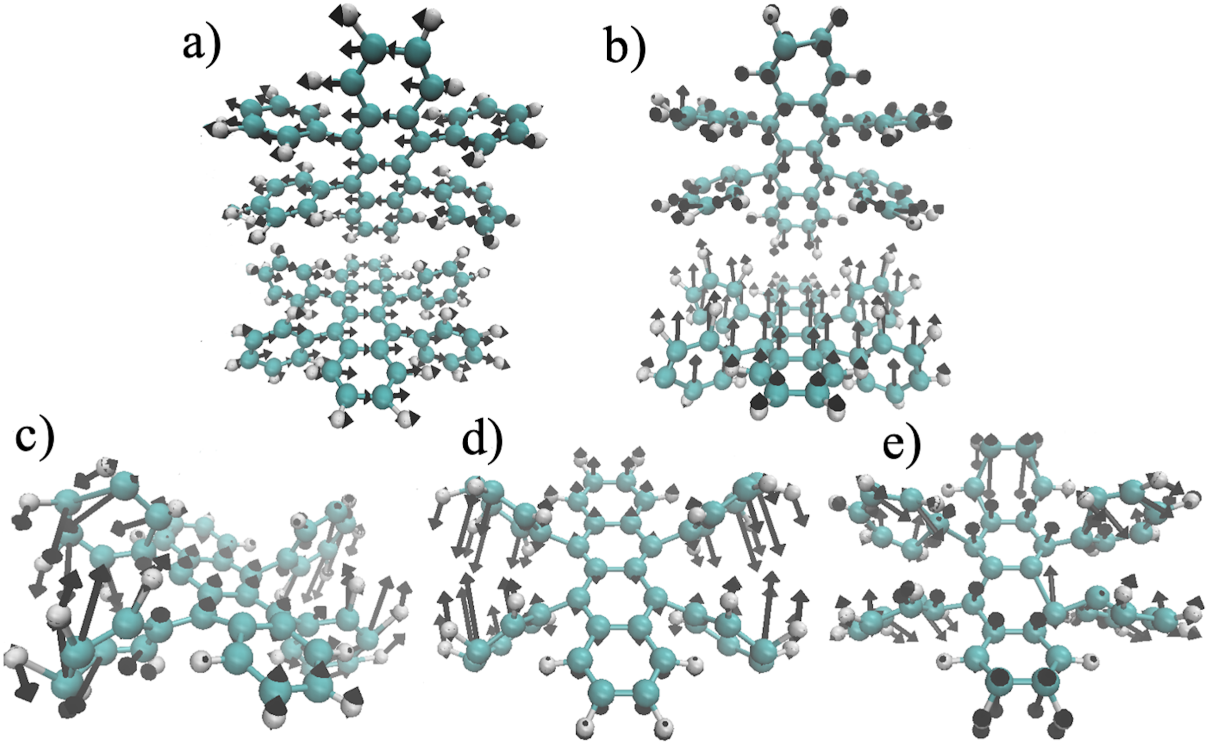

Figure A.13. Phonon modes for rubrene in the low energy region with large contribution to σ. Phonon frequencies in wavenumbers are 32.50, 32.54, 50.5, 105.2, and 144.5 for a-e, respectively. Relevant phonons are shown on reduced number of molecules for clarity.

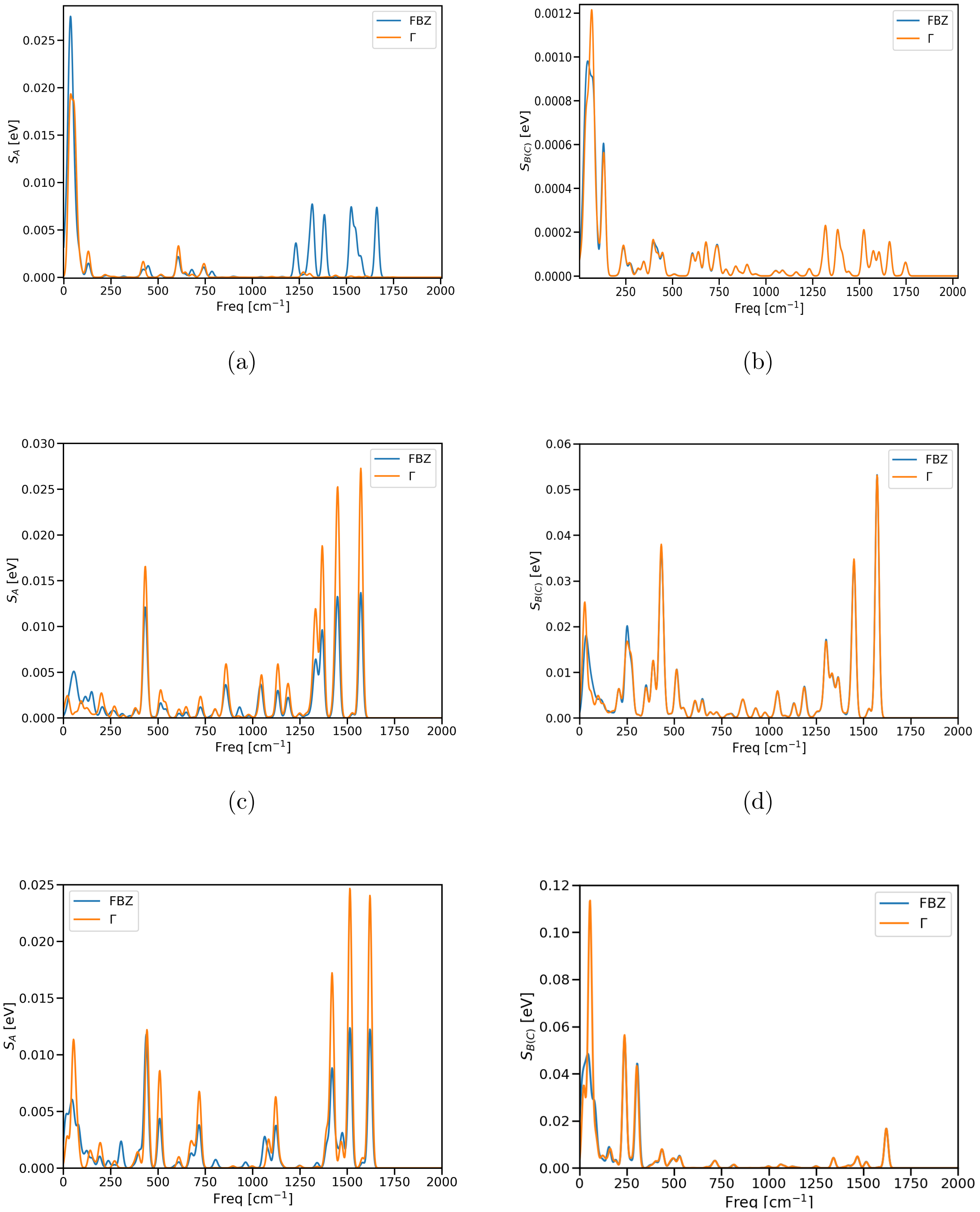

(a) (b)

(c) (d)

(e) (f)

Figure A.14. The spectral density of dimers A and B (C) for the three molecules considered here, from top to bottom (a-b) Rubrene, (c-d) C8-BTBT and (e-f) BTBT.

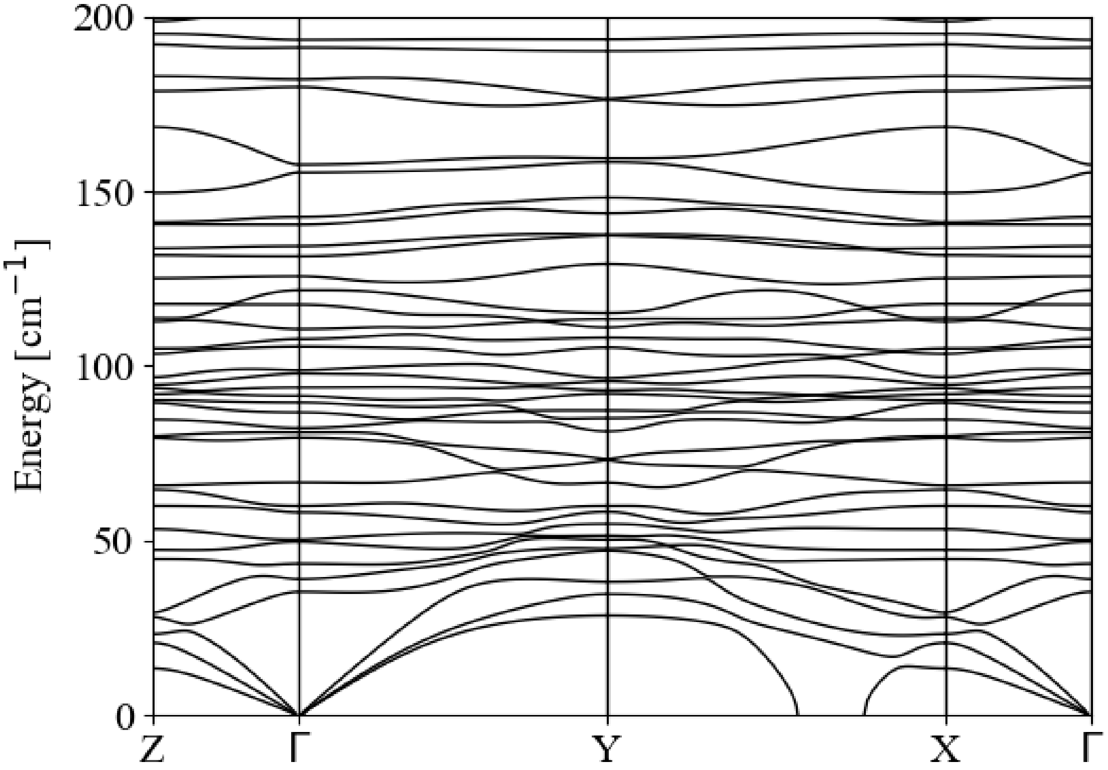

Figure A.15. Phonon band structure for TIPS-Pentacene.

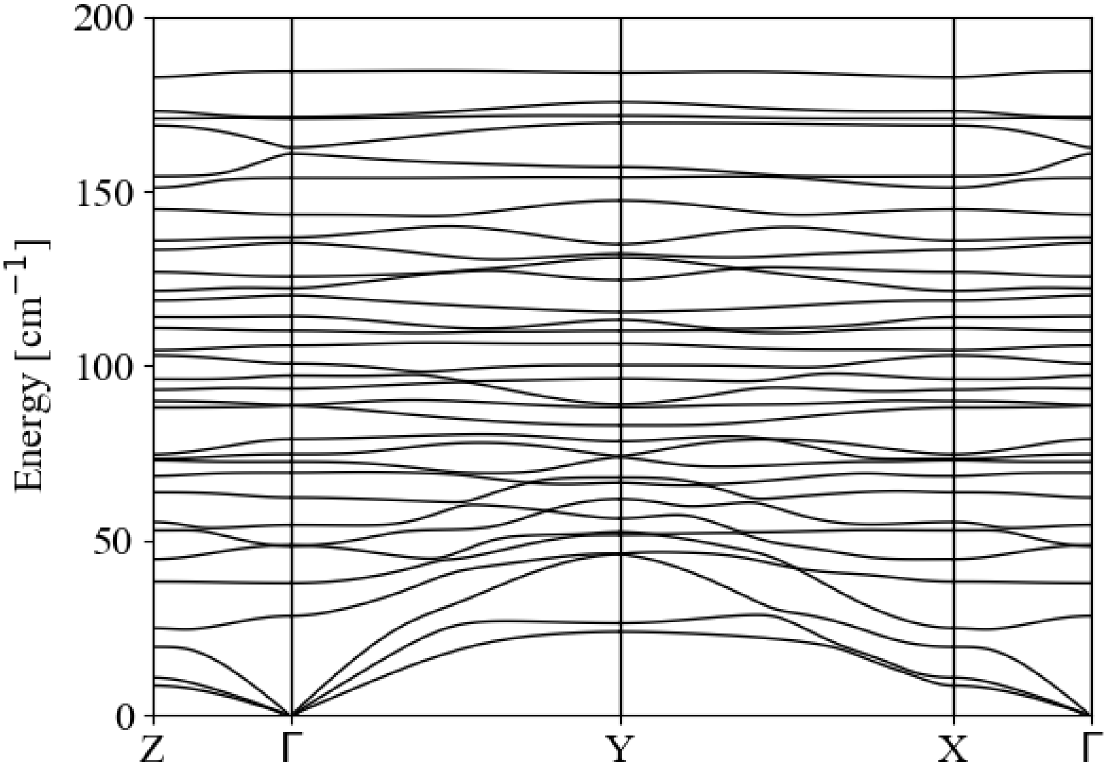

Figure A.16. Phonon band structure for TESADT.

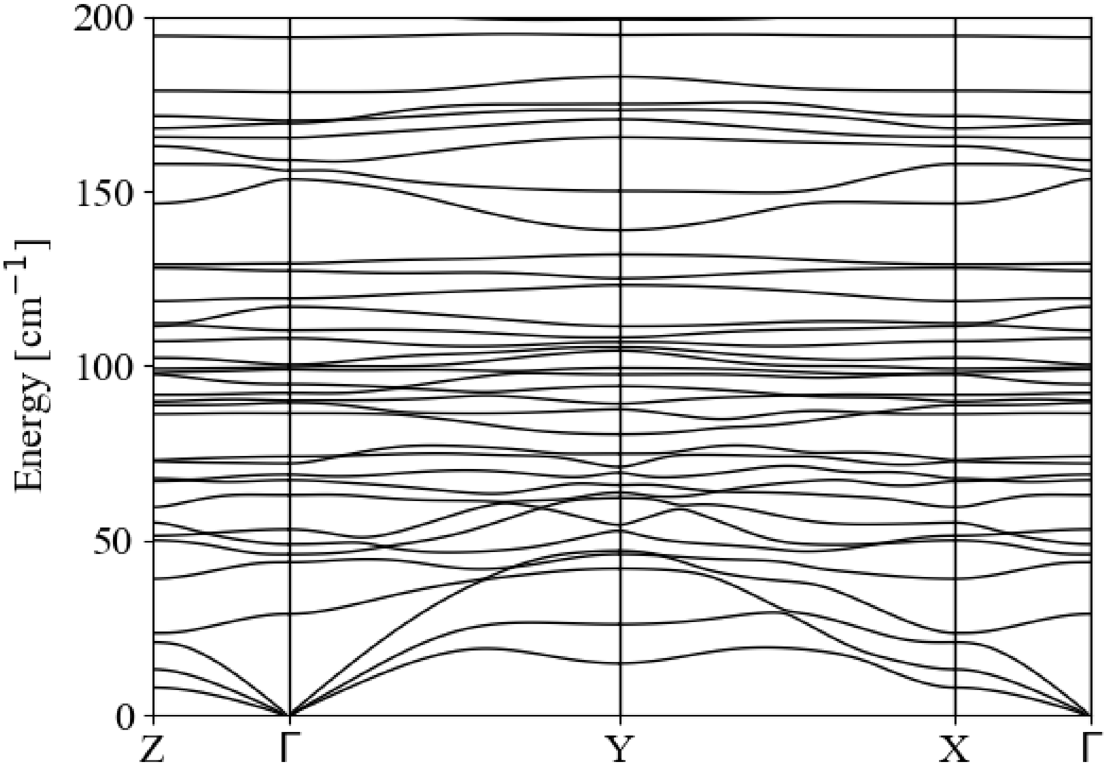

Figure A.17. Phonon band structure for diF-TESADT.

Bibliography

(1) Ramirez-Cuesta, A. J. *Computer Physics Communications* **2004**, *157*, 226–238.

(2) Nematiaram, T.; Padula, D.; Landi, A.; Troisi, A. *Advanced Functional Materials* **2020**, *30*, 1–10.

(3) Nematiaram, T.; Troisi, A. *Materials Horizons* **2020**, *7*, 2922–2928.

(4) Frisch, M. J. et al. Gaussian~16 Revision C.01, Gaussian Inc. Wallingford CT, 2016.

(5) Nematiaram, T.; Troisi, A. *Journal of Chemical Physics* **2020**, *152*, 190902.

(6) Malagoli, M.; Coropceanu, V.; Da Silva Filho, D. A.; Brédas, J. L. *Journal of Chemical Physics* **2004**, *120*, 7490–7496.

(7) Ren, X.; Bruzek, M. J.; Hanifi, D. A.; Schulzetenberg, A.; Wu, Y.; Kim, C. H.; Zhang, Z.; Johns, J. E.; Salleo, A.; Fratini, S.; Troisi, A.; Douglas, C. J.; Frisbie, C. D. *Advanced Electronic Materials* **2017**, *3*, 1–7.

(8) D. Feinberg, S. Ciuchi, F. de Pasquale *Int. J. Mod. Phys. B* **1990**, *4*, 1317.

(9) Harrelson, T. F. et al. *Materials Horizons* **2019**, *6*, 182–191.

(10) Xie, X.; Santana-Bonilla, A.; Troisi, A. *Journal of Chemical Theory and Computation* **2018**, *14*, 3752–3762.

(11) Coropceanu, V.; Sánchez-Carrera, R. S.; Paramonov, P.; Day, G. M.; Brédas, J. L. *Journal of Physical Chemistry C* **2009**, *113*, 4679–4686.

(12) Fratini, S.; Mayou, D.; Ciuchi, S. **2016**, *26*, 2292–2315.

(13) Fratini, S.; Ciuchi, S. *arXiv* **2019**, *013001*, 1–14.

(14) Giannini, S.; Carof, A.; Ellis, M.; Yang, H.; Ziogos, O. G.; Ghosh, S.; Blumberger, J. *Nature Communications* **2019**, *10*, 1–12.

(15) Fratini, S.; Ciuchi, S.; Mayou, D.; De Laissardière, G. T.; Troisi, A. *Nature Materials* **2017**, *16*, 998–1002.

(16) Nematiaram, T.; Ciuchi, S.; Xie, X.; Fratini, S.; Troisi, A. *Journal of Physical Chemistry C* **2019**, *123*, 6989–6997.

Appendix B

SI for Compact, and Portable Automatic Sample Changer Stick for Cryostats and Closed-Cycle Refrigerators

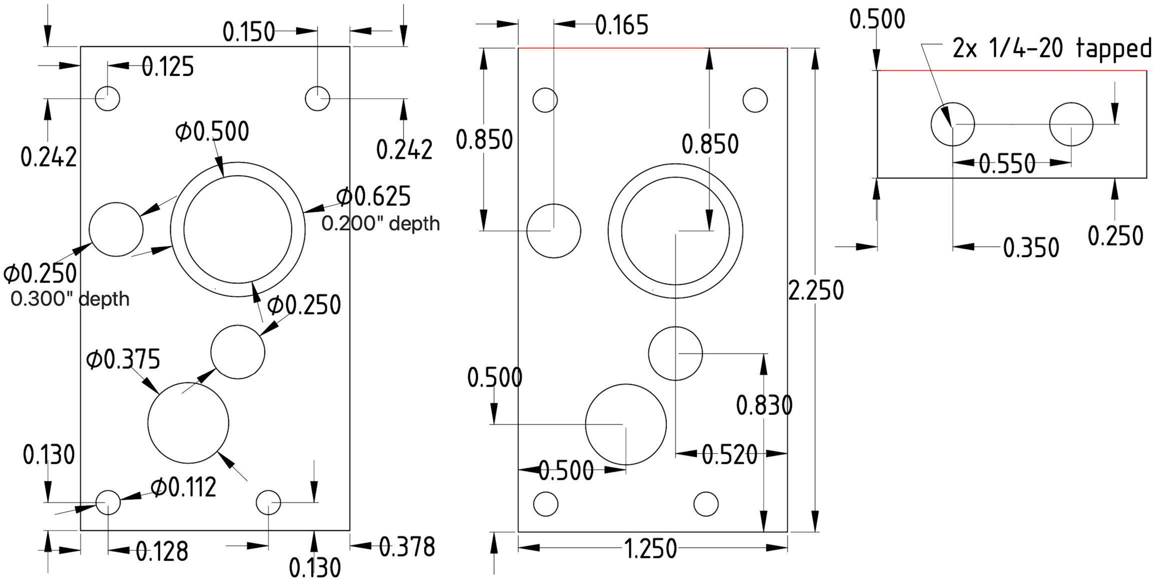

Figure B.1. Engineering drawing of lower 6061 aluminum guide. Red edge denotes shared edge between drawings. Units are in inches.

Table B.1. Bill of materials from supplier McMaster-Carr.

Quantity	Product	Description	Total
5	2424K11	1/4" Shaft Set Screw Coupling	63.8
1	6443K24	Single U-Joint Steel, for 1/4" Diameter	123.84
1	93615A415	18-8 SS Low-Profile Socket Head Screws	5.17
1	1257K132	Rotary Shaft 303 SS, 1/4" Diameter, 60" Long	61.5
2	6462K17	1/8" Diameter Set Screw Shaft Collar 303 SS	11.26
1	98980A965	304 SS Acme Lead Screw	30.43
1	95072A881	Acme Threaded Nut, Bronze, 1/4"-16 Thread Size	36.04
1	1329K11	Acme Flange 303 SS, 9/16"-18 Thread Size	56.48
1	89535K16	304/304L SS Rod 1/8" Diameter, 1’ Long	1.92
1	8975K597	Aluminum 1/4" Thick x 1-1/4" Wide, 3 Feet Long	11.84
1	91125A493	8-32 Female Threaded Standoff 18-8 SS	4.53
1	8975K473	Aluminum 1/2" Thick x 1-1/4" Wide, 1 Foot Long	8.86
1	8974K71	6061 Aluminum 2" Diameter, 1/2 Feet Long	23.82
1	91841A009	18-8 Stainless Steel Hex Nut 8-32 Thread Size	4.73
4	95907A460	Extension Spring Stud Anchor 8-32 Thread Size	26.12
1	8974K22	6061 Aluminum 1/4" Diameter, 3 Feet Long	6.31
2	9433K905	302 SS Extension Spring with Hook Ends	20.76
4	95907A480	Extension Spring Stud Anchor 1/4"-20 Thread Size	27.76
1	92673A113	18-8 SS Hex Nut 1/4"-20 Thread Size	3.15
4	91072A367	1/4"-20 to 5/16"-18 Hex Thread Adapter	38.92
4	91780A363	1/4"-20 Female Threaded Hex Standoff Aluminum	23.64
1	92311A544	18-8 SS Cup-Point Set Screw 1/4"-20 Thread	9.91
1	1610T19	6061 Aluminum 3" Diameter, 3" Long	21.52
1	8735K27	PTFE bar 1/4" Thick, 2" Wide, 1 ft. length	38.49
4	6377K12	Rulon J Sleeve Flanged, 1/4" Shaft, 3/8" Housing	26.12
1	6377K102	Rulon J Sleeve Flanged, 3/16" Shaft, 1/4" Housing	25.52
			$712.44

Table B.2. Bill of materials for parts from other vendors.

Company	Quantity	Product	Description	Total ($)
Linengineering	2	WO-5718M-02SD	Stepper motor	177.48
Linengineering	2	2090-R356-ND	Stepper motor driver	507.96
Kurt J. Lesker	1	QF100-BK	ISO100-K flange	105.55
Kurt J. Lesker	2	HN-0133	DN16CF half nipple	113.60
Kurt J. Lesker	2	KLFDCF025133-A	Rotary feedthrough	1660
Digikey	2	HEDS-5640#A06	Optical encoder	113.80
				2678.39

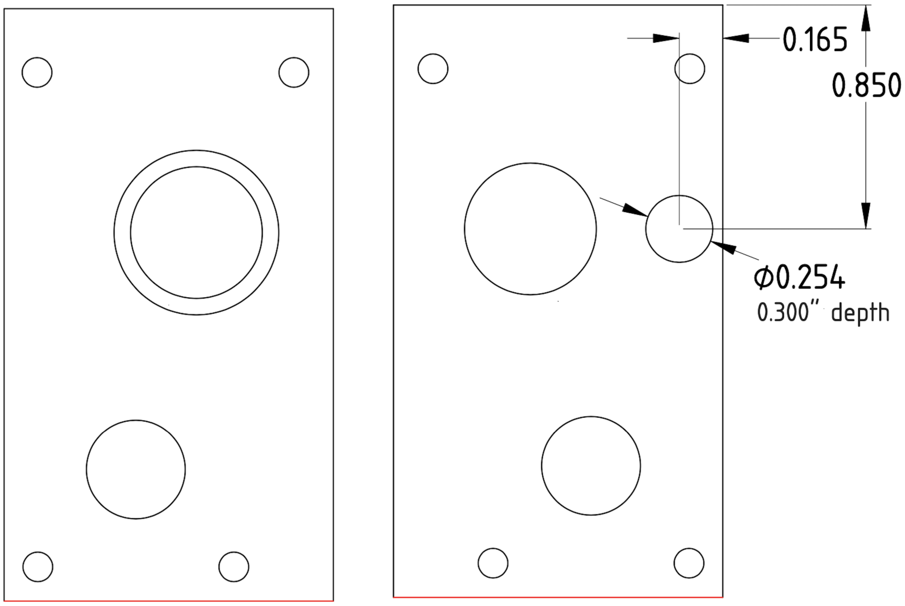

Figure B.2. Engineering drawing of middle 6061 aluminum guide. The left shows the top, while right shows the bottom. Omitted dimensions are shared with Figure B.1. Red edge denotes shared edge between drawings. Units are in inches.

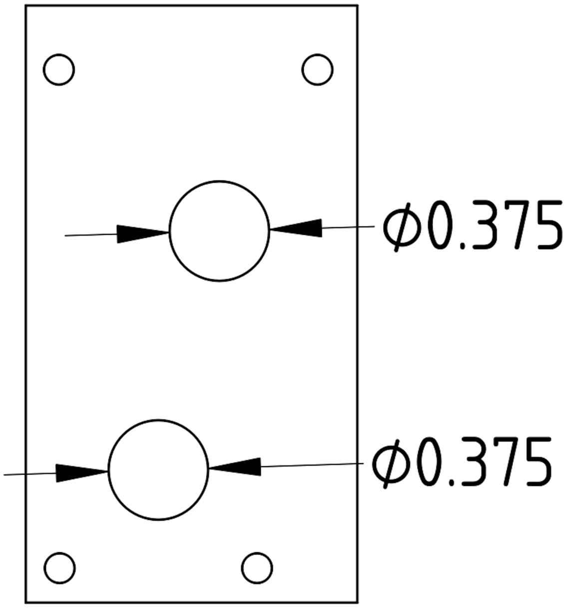

Figure B.3. Engineering drawing of upper 6061 aluminum guide. Omitted dimensions are shared with Figure B.1. Units are in inches.

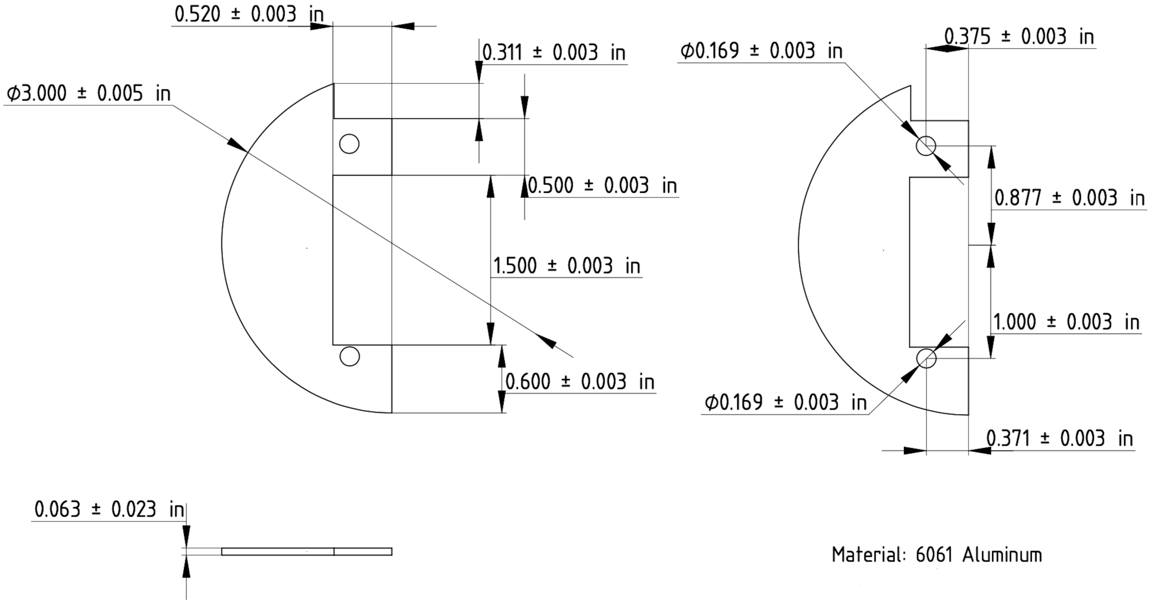

Figure B.4. Engineering drawing of left baffle made of 6061 aluminum. Units are in inches.

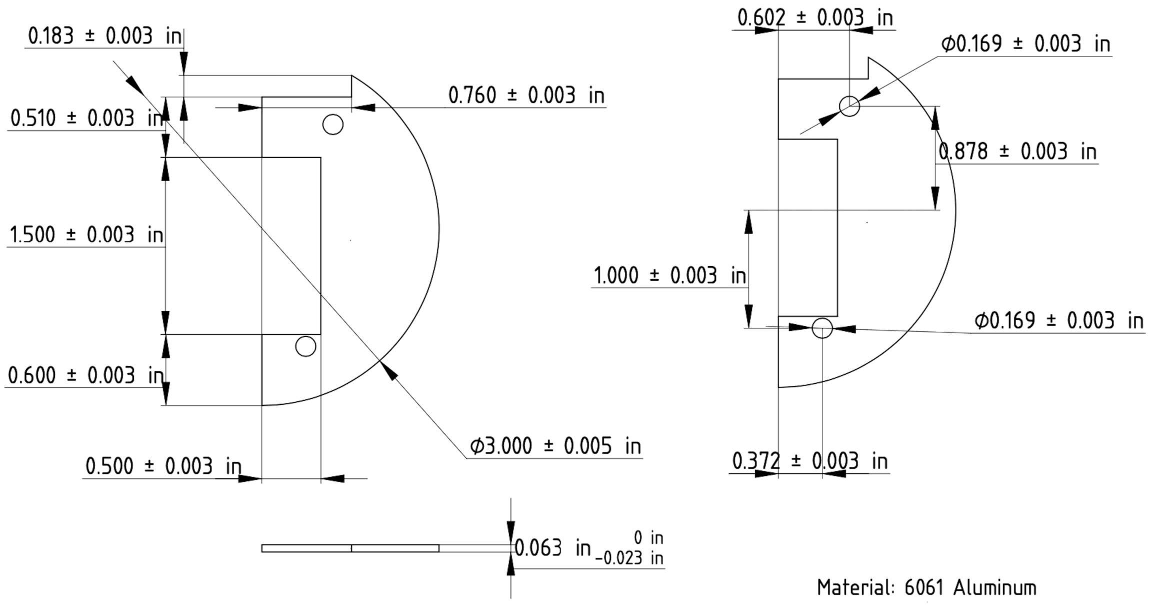

Figure B.5. Engineering drawing of right baffle made of 6061 aluminum. Units are in inches.

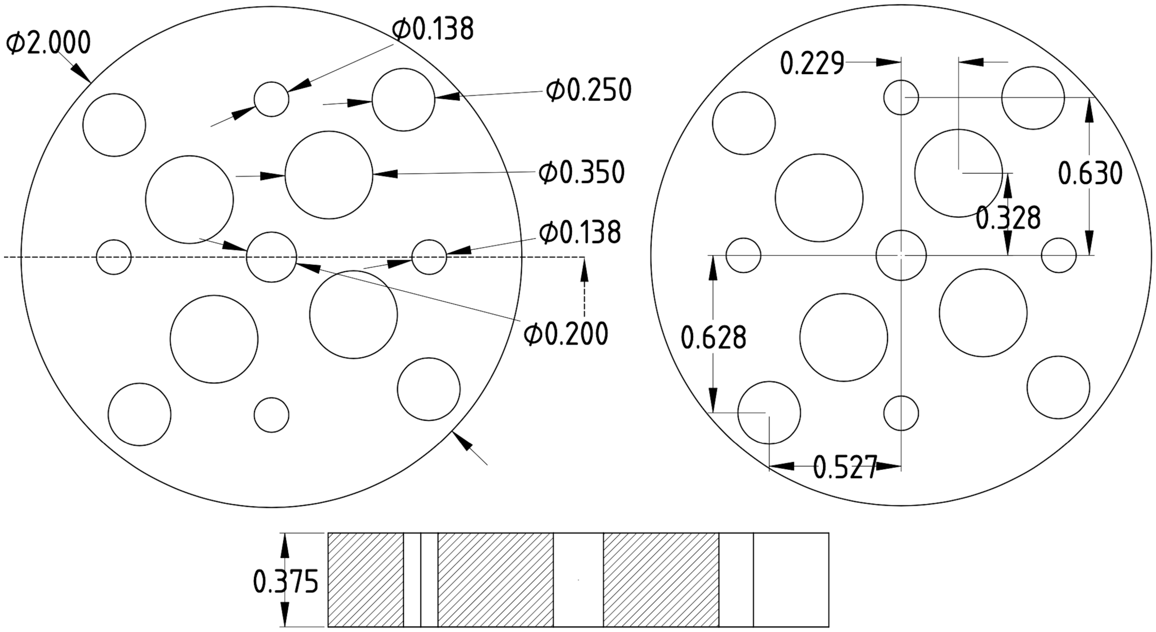

Figure B.6. Engineering drawing of 6061 aluminum round of upper carousel. Through holes for other quadrants are 90° apart measured from center. Units are in inches.

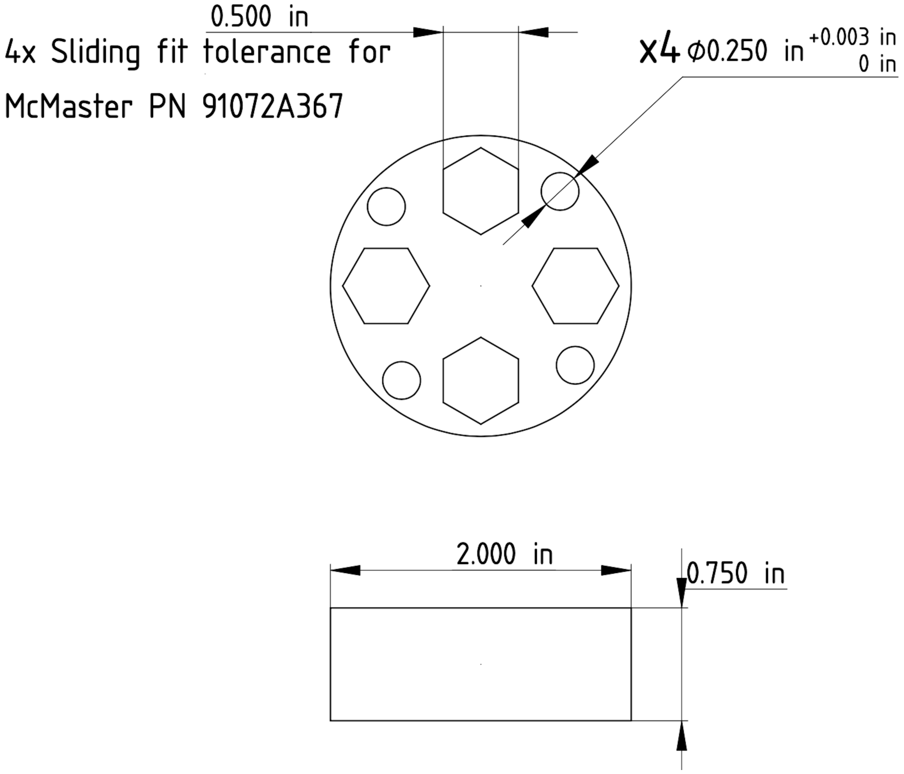

Figure B.7. Engineering drawing of 6061 aluminum round of lower carousel. The 0.250" holes are same dimensions as of Figure B.6. Units are in inches.

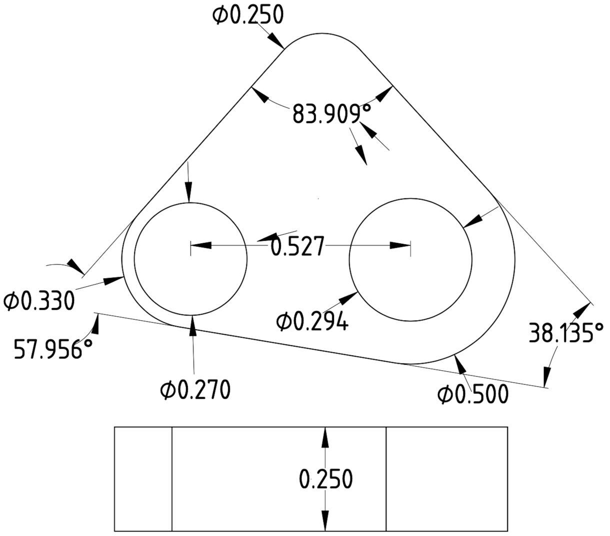

Figure B.8. Engineering drawing of PTFE linear guide. STEP file included for laser or CNC cutting. Units are in inches.

Appendix C

SI for Photochemistry Sample Sticks for Inelastic Neutron Scattering

C.0.1 Supplemental Figures

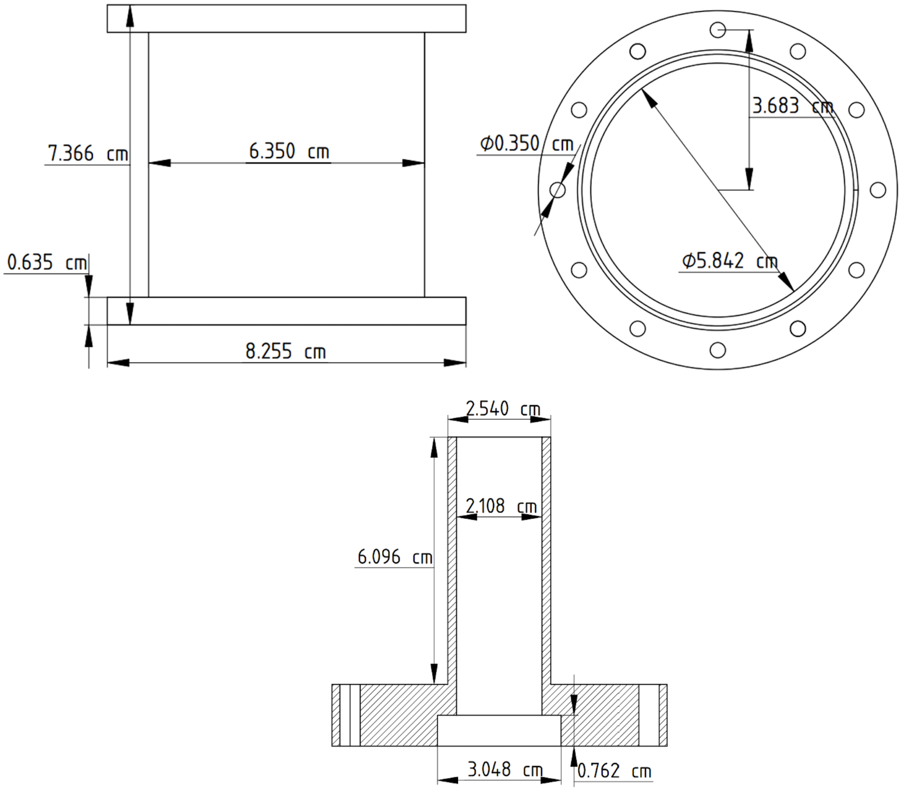

Figure C.1. Engineering drawing of 6061 aluminum LED housing. Top row show the double flanged body. Bottom is the half nipple.

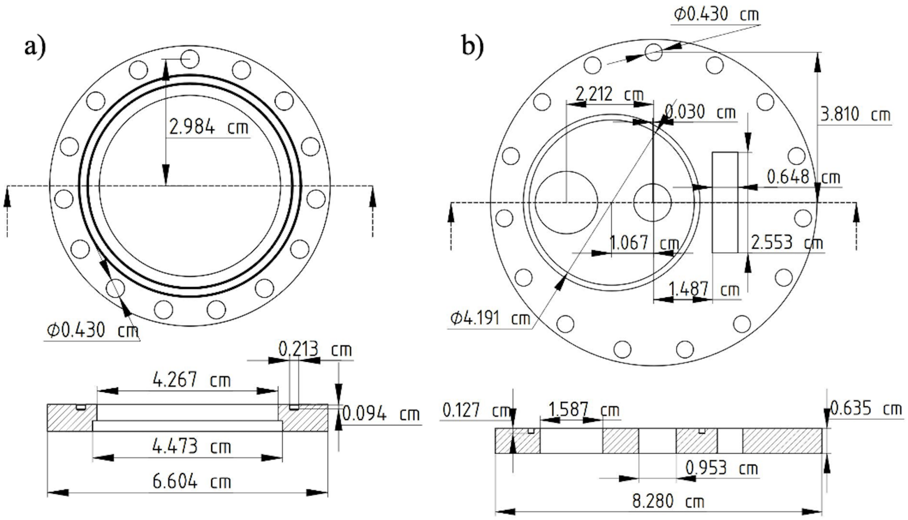

Figure C.2. Engineering drawings of 6061 aluminum middle upper (left) flange and lower (right) flanges.

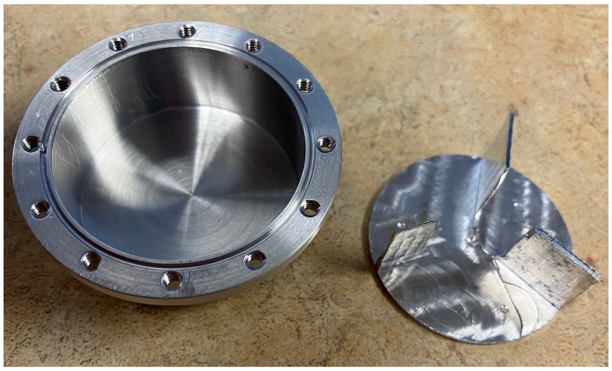

Figure C.3. Aluminum sample can with tumbler blade inserts.

Figure C.4. 405 nm photoresin in a quartz sample holder. Aluminum base includes concentric hole to mount onto the rotating shaft, secured using a set screw on the threaded hole.

Appendix D

SI for Excited State Geometry Shifts Energy Levels for Favorable Singlet Fission in Tetracene

D.0.1 Supplemental Figures

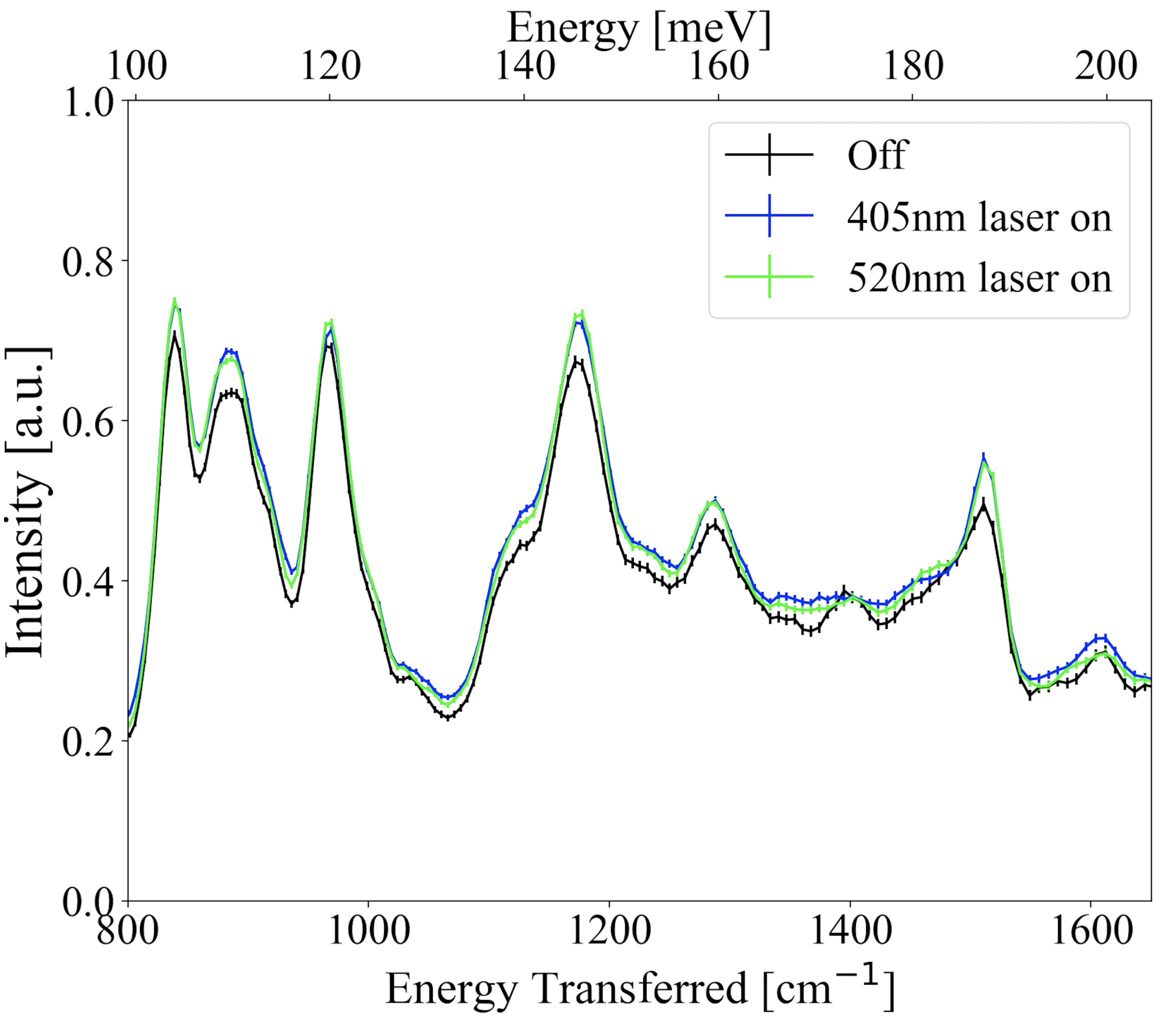

Figure D.1. INS spectrum for pentacene with 405 nm laser on (blue), 520 nm laser on (green), and laser off (black) between ∼100-200 meV.

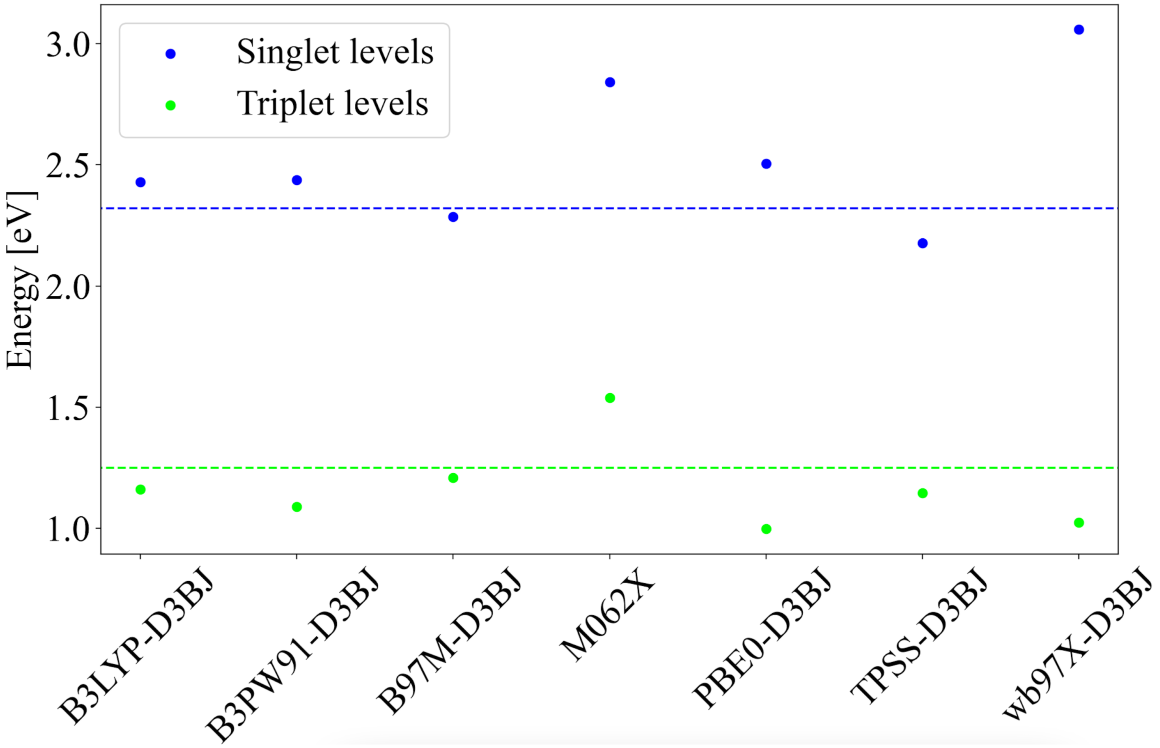

Figure D.2. Calculated Singlet and Triplet energy levels using different levels of theory in ORCA. Blue scatter plot shows Singlet levels, and green shows Triplet levels. Dashed lines represent experimental levels reported in literature.